SUPERELASTIC SHAPE MEMORY ALLOY COMPOSITE BARS FOR REINFORCING CONCRETE STRUCTURES

BY

NICHOLAS E. WIERSCHEM

THESIS

Submitted in partial fulfillment of the requirements
for the degree of Master of Science in Civil Engineering
in the Graduate College of the
University of Illinois at Urbana-Champaign, 2009

Urbana, Illinois

Adviser:

Professor Bassem Andrawes

ABSTRACT

Superelastic shape memory alloys (SMAs) are a class of metallic alloys that have the unique property of being able to undergo large amounts of plastic strain while remaining elastic and dissipating energy. This thesis explored a strategy for adding ductility and energy dissipation to FRP reinforcing bars through the use of SMA-fiber reinforced polymer (SMA-FRP) composites, an innovative type of composite that consists of a polymer matrix reinforced with small diameter superelastic SMA wires with and without additional conventional fiber reinforcement. In this study an analytical model for the behavior of SMA-FRPs was developed based on experimental results. This model was then used in a parametric study to determine the effect of the composition of the composite on its performance. After which, the SMA-FRP bars were explored as reinforcement for concrete structures with analyses at the section, substructure, and structural levels. From this study it was found that SMA-FRP reinforcing bars behave in a ductile manner and are capable of dissipating energy. Furthermore, it was found that SMA-FRP bars have more potential to improve the ductility and energy dissipation capability of concrete structures compared to conventional FRP bars.

ACKNOWLEDGEMENTS

I would like to acknowledge my advisor, Dr. Bassem Andrawes; without his guidance and support, this work would not have been possible. I would also like to acknowledge the academic and emotional support of my lab mates and fellow graduate students here at the University of Illinois. Even on the coldest of winter days, they have brought some joy into coming to Newmark. I would also like to thank my parents. They have been a great source of support and I would like to thank them for understanding when I miss a holiday because I am working to fulfill my dream. Finally, I would like to thank my girlfriend Becky. She has been a constant source of encouragement and positive thinking. Conversations about our shared lust for sleep have brought a smile to my face on many of my late nights. I couldn't imagine life without her.

TABLE OF CONTENTS

CHAPTER 1:

INTRODUCTION

1.1 MOTIVATION

Fiber reinforced polymer (FRP) bars have long been suggested as reinforcement for concrete structures because of some of the unique advantages they provide when compared to traditional steel reinforcement. These advantages include low strength-to-weight ratio, magnetic invisibility, and high corrosion resistance [Bank, 2006]. There are numerous examples of FRP reinforcement of concrete structures in use today, including diaphragm walls for tunnel boring [Weber et al. (2006)], slabs of parking structures [Benmokrane et al. (2004)], and most commonly, bridge decks [Bakis et al. (2001), Bank et al. (2005), and Bradberry (2001)]. Despite these examples, FRP reinforcement has not yet been used in structures with the aim of mitigating their dynamic response under service or extreme dynamic loads such as vibration control or seismic design applications, respectively (Harris et al. 1998). The failure of FRP reinforcement to gain acceptance in such type of applications is attributed to their linear elastic behavior, which limits their ability to provide concrete structures with sufficient ductility or energy dissipation capability. (Benmokrane et al. 1995; Said and Nehdi 2004).

Several researchers have attempted to address the shortcomings of FRP as reinforcement with a FRP reinforcing material known as hybrid FRP [Harris et al. 1998, Somboonsong et al. 1998, and Pastore et al. 1999]. Hybrid FRP is a composite which consists of a polymer matrix reinforced with several different types of conventional fibers with different moduli of elasticity and rupture strains. The result of this combination of

different conventional fibers is a material with a ductile monotonic tensile stress-strain curve that contains an initially elastic portion followed by a low stiffness region. However, the ductility of this material is achieved by the rupture of the fiber reinforcement, thus the ductility is achieved through permanent damage.

This thesis addresses the issue of ductility and energy dissipation in FRP reinforcement bars with the introduction of shape memory alloy-FRP (SMA-FRP). SMA-FRP is an innovative composite material that consists of a polymer matrix reinforced with small diameter superelastic shape memory alloy (SMA) wires with and without additional conventional fiber reinforcement. It is proposed that with select reinforcement, the unique properties of SMA-FRP composites can be used to add ductility and energy dissipation to concrete structures primarily reinforced with FRP.

1.2 THESIS OUTLINE

This thesis is divided into 8 chapters, including the introduction. In Chapter 2 literature related to FRP reinforcement bars and SMA composites is reviewed. In Chapter 3 experimental tests of SMA-FRP coupons are discussed. Based on this experimental work, an analytical model for the behavior of SMA-FRP is developed. Chapter 4 presents a parametric study of SMA-FRPs, which is used to investigate the effect of the composition of the SMA-FRP on its performance. Chapter 5 begins the discussion of the effects of using SMA-FRP composite bars as reinforcement in concrete structures. In this chapter an analytical study is performed at the section level with comparisons made between FRP and SMA-FRP reinforced sections made using moment-curvature relationships. In Chapter 6 SMA-FRP reinforcement in concrete structures is

evaluated at the substructure level with a cyclic analysis of reinforced concrete structures being performed in two case studies. In these studies comparisons are once again made to structures reinforced only with FRPs. In Chapter 7, SMA-FRP reinforcement is explored at the structural level with an incremental dynamic analysis of concrete frames reinforced with SMA-FRP in all beam plastic hinge zones. Based on this work, conclusions made in regards to SMA-FRP bars are presented in Chapter 8.

CHAPTER 2:

LITERATURE REVIEW

2.1 FRP COMPOSITE BARS

Fiber Reinforced Polymers (FRPs) are increasingly gaining popularity in the field of civil engineering. Common applications for FRPs in civil engineering range from retrofitting structures with patches and wraps to structures made entirely with FRP members. Another increasingly common application is internal FRP reinforcing bars for concrete structures. FRP bars for this application consist of a polymer matrix material, typically epoxy, polyester, or vinylester, reinforced with conventional fibers. Various different conventional fibers have been used in FRP bars, including E-glass, S-Glass, carbon, and aramid. Table 2.1 lists some of the typical mechanical properties of these conventional fibers. As one can see from this table, the reinforcing fibers have a wide range of modulus of elasticity and rupture strains; however, all these conventional fibers are similar in that their stress-strain behavior is linear elastic until rupture.

Table 2.1: Properties of conventional fibers used in FRP [Bank (2006), various manufacturers]

Fiber Type	Modulus of Elasticty (GPa)	Ultimate Strength (MPa)	Ultimate Strain (mm/mm)
E-Glass	68.9	1378	0.020
S-Glass	86.2	2586	0.030
Arimid	124.1	3723	0.030
Low Modulus Carbon	230.0	3790	0.016
High Modulus Carbon	370.0	3520	0.010

One of the processes that is commonly used in the manufacturing of FRP reinforcement bars is the pultrusion process. The name pultrusion comes from the combination of the words "pull" and "extrusion". This process begins by pulling multiple strands of conventional fibers from rovings. Resin is then added to these strands by a resin bath or impregnation. The strands and resin are then combined and run through a series of toolings, which help the composite form the desired shape. The composite is then run through a heated metal die. This process can be augmented to allow for filler materials, as well as, exterior veils, treatments, and deformation [Strongwell Corporation (2009)]. A schematic of this process can be found in Figure 2.1. Some of the benefits of this process include a high degree of automation, and the ability to manufacture composites with a wide range of shapes and lengths with little alteration to the machine. Pictures of rebars manufactured with the pultrusion process are seen in Figure 2.2. The surface deformations and roughness seen on some of the rebars shown in this figure are designed to increase the bond between the rebar and concrete [Katz (1999)].

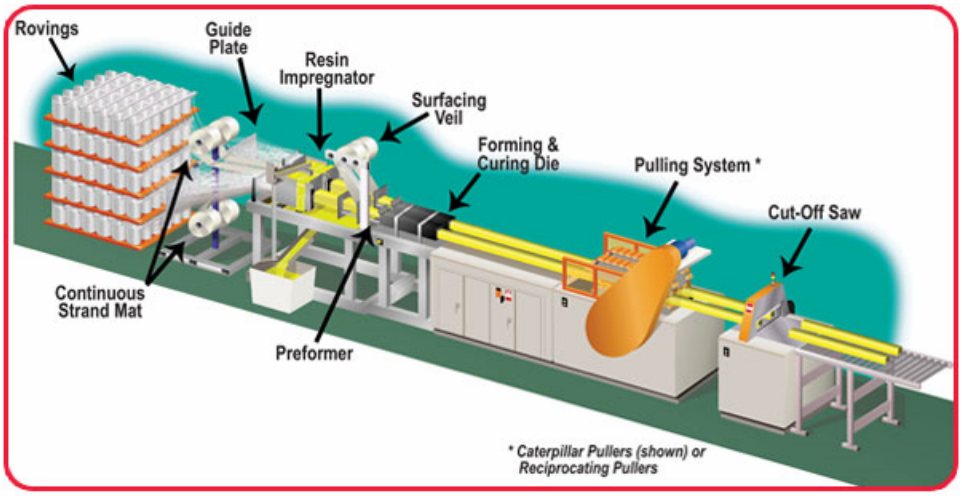

Figure 2.1: Schematic of the pultrusion process [Strongwell Corporation (2009)]

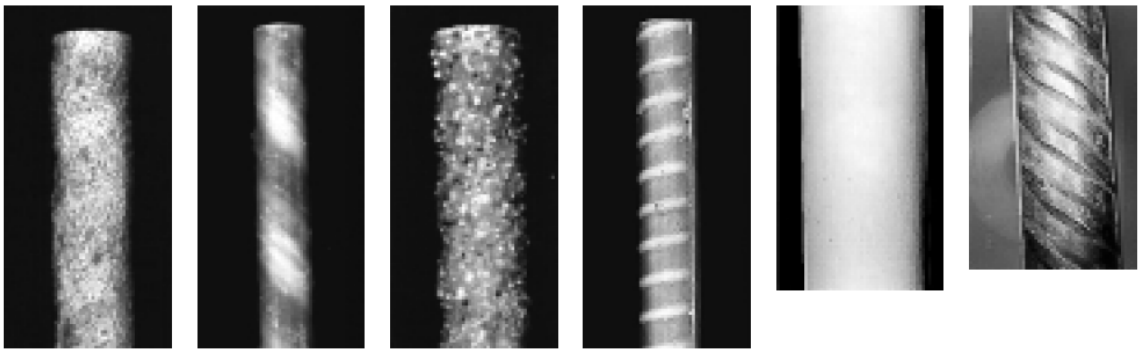

Figure 2.2: FPR reinforcing bars manufactured by pultrusion [Katz (1999)]

When compared to traditional steel rebar, FRP rebars have numerous advantages. Some of the most prevalent of these advantages include high strength-to-weight ratio, magnetic invisibility, and high corrosion resistance [Bank, 2006]. Interest in exploiting the advantages of FRP rebar has lead to the implementation of FRP reinforcement in a multitude of different concrete structures, these including, diaphragm walls for tunnel boring (Weber et al. 2006) and slabs of parking structures (Benmokrane et al. 2004). However, today the most common use of FRP reinforcement is in bridge decks (Bank et al. 2005; Bradberry 2001; Bakis et al. 2001). One reason for the relative popularity of FRP reinforcement of bridge decks is extreme environmental conditions some bridges are subjected to. Because of the environmental challenges, these bridges stand to benefit more from the corrosion resistance provided by the FRP reinforcement. An example of FRP reinforcement used in the construction of a reinforced concrete bridge deck is seen in Figure 2.3, which shows the Morristown Bridge under construction in Vermont.

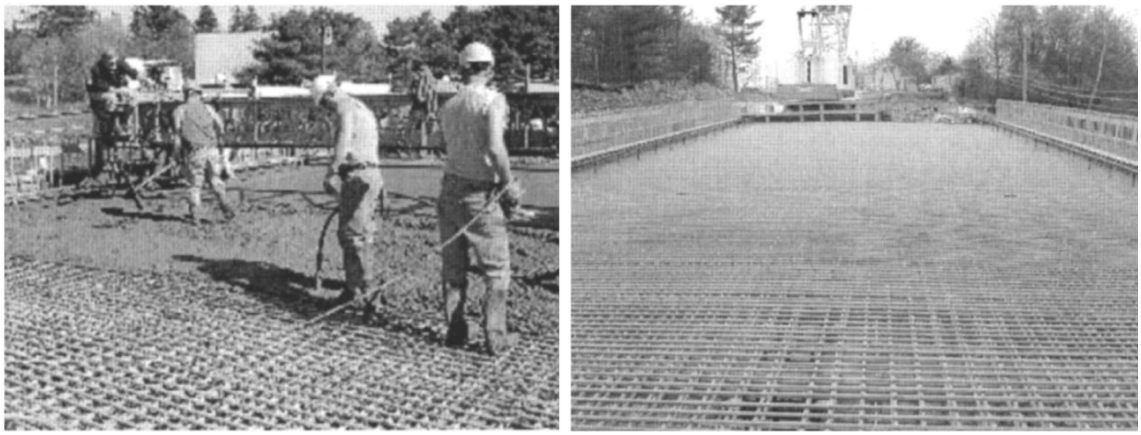

Figure 2.3: FRP reinforced bridge deck under construction in Vermont [Benmokrane et al. (2006)]

Despite these examples, FRP reinforcement has not yet been used in structures with the aim of mitigating their dynamic response under service or extreme dynamic loads such as vibration control or seismic design applications, respectively (Harris et al. 1998). The failure of FRP reinforcement to gain acceptance in such type of applications is attributed to their linear elastic behavior, which limits their ability to provide concrete structures with sufficient ductility or energy dissipation capability (Benmokrane et al. 1995). An example of this is found in a study that compared the behavior of FRP and steel reinforced beam-column joint subassemblages [Said and Nehdi (2004)]. In this study, beam-column joint subassemblages reinforced steel and FRP were subjected to a cyclic beam-column tip displacement loading The resulting load deformation results from the steel reinforced and FRP reinforced specimens are found in Figure 2.4. As discussed above, this figure shows that the FPR reinforced joint did not show the ductility or energy dissipation, denoted by wide hysteretic loops, that was seen in the steel

reinforced specimen. This study suggested that the reason for this is the non-ductile nature of the FRP reinforcement.

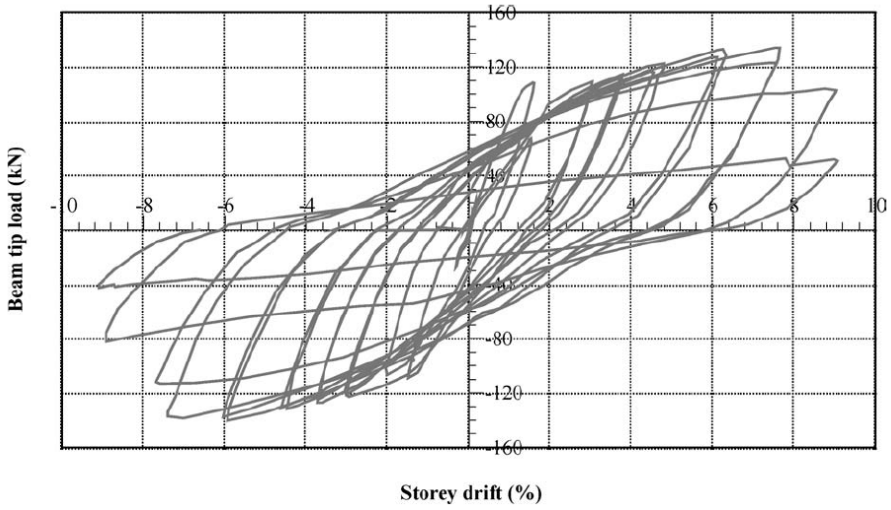

(a)

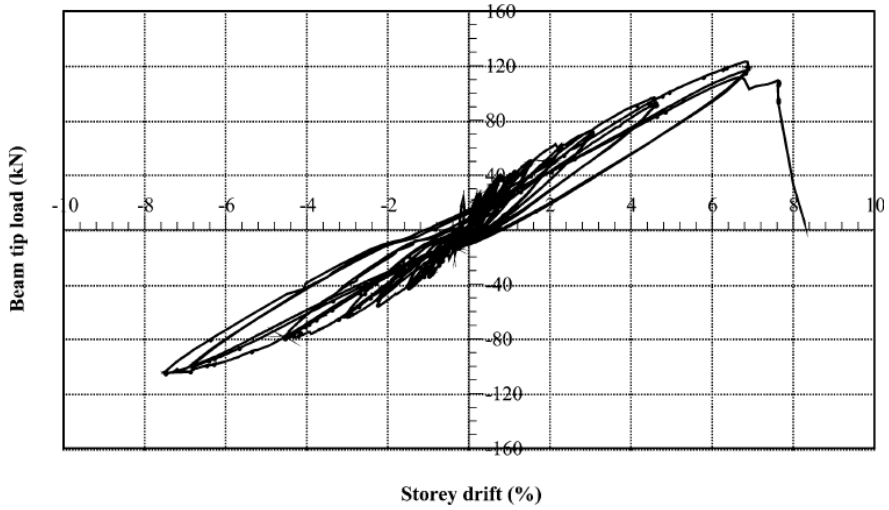

(b)

Figure 2.4: Load-deformation results from a test of a beam-column joint specimen subjected to cyclic beam tip deflection (a) steel reinforced (b) FRP reinforced [Said and Nehdi (2004)]

Several researchers, (Harris et al. 1998; Somboonsong et al. 1998; Pastore et al. 1999), have attempted to address this concern by developing a ductile reinforcing material with FRPs. The result of this research is a composite reinforcement, which is commonly referred to as hybrid FRP. This hybrid FRP is manufactured in a process closely related to pultrusion and is composed of several different reinforcing fibers that have different rupture strains and modulus of elasticity. Figure 2.5 shows a schematic view of a hybrid FRP bar and how the different reinforcing materials are braided together in the composite. The combination of these fibers allows the hybrid FRP to exhibit a ductile monotonic stress-strain relationship with a low stiffness region after an initial linear elastic period. This monotonic ductile behavior is exhibited in Figure 2.6, which shows the resulting stress-strain behavior from tensile tests of hybrid FRP bars. The shortcoming of this reinforcement material is that ductility is achieved through permanent damage to the reinforcement; this is indicated in the stress-strain relationship by the drops in capacity of the bar due to the rupture of some of the reinforcing material. Although a different damage mechanism is used, this is quite similar to steel reinforcement, which achieves ductility also through permanent plastic deformations.

This thesis addresses the shortcomings of FRP and hybrid- FRP reinforcing bar, in regard to ductility and energy dissipation, with the introduction of shape memory alloy composite referred to as SMA-FRP. SMA-FRP is an innovative composite material that consists of a polymer matrix reinforced with small diameter superelastic shape memory alloy (SMA) wires with and without additional conventional fiber reinforcement. Accordingly, a thorough review of both SMAs and SMA composites is presented next.

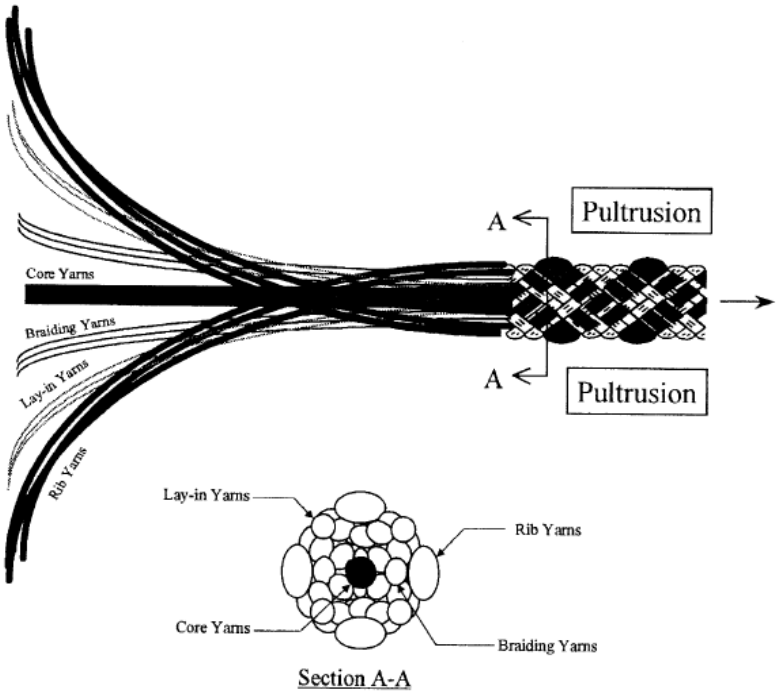

Figure 2.5: Schematic view of the composition of a hybrid FRP bar [Somboonsong et al. (1998)]

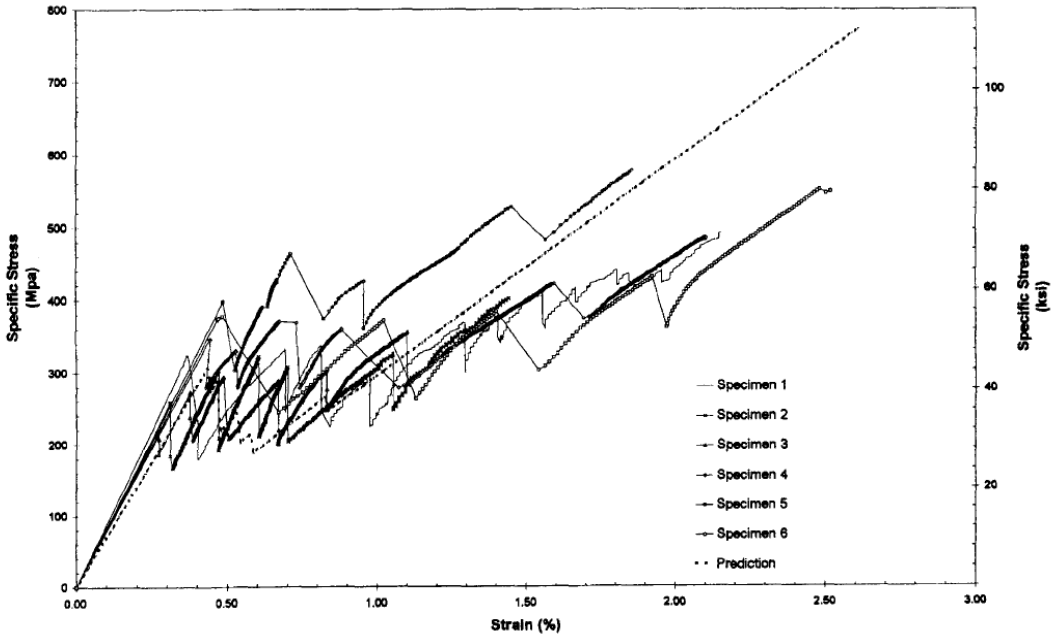

Figure 2.6: Monotonic stress-strain curve from tensile tests of hybrid FRP bars [Harris et al. (1998)]

2.2 SHAPE MEMORY ALLOYS

Shape memory alloys (SMAs) are metallic alloys that display two unique qualities, shape memory effect and superelasticity, both of which are related to the material phase of the SMA [Lagoudas (2008)]. The material phase of the alloy is dependent on temperature; consequently, the temperature of the SMA has a great effect on its mechanical properties. At relatively high temperatures, the alloy is in an austenite phase while at relatively low temperatures, it is in a martensite phase [Brinson (1993)]. The four transformation temperatures that define the SMA's transformation from one phase to the other are M_f, M_s, A_s, and A_f, which are the martensite finish temperature, martensite start temperature, austenite start temperature, and the austenite finish temperature, respectively. The relationship between these transformation temperatures can be seen in Figure 2.7. As an example of the temperature dependency of the SMAs is best illustrated with an example; this example can be followed with Figure 2.7. If a 100% martensite SMA was heated it would begin martensite to austenite phase transformation when the alloy reaches A_s and finish transformation to 100% austenite when the alloy reaches A_f. Additionally, if the SMA in this example was then cooled, reversed transformation would start at M_s and the transformation back to 100% martensite would be completed when the alloy reaches M_f.

In addition to temperature induced phase changes, SMAs can undergo phase change due to changes in mechanical stress. For example, an increase in mechanical stress in an austenite SMA can lead to a phase change to martensite. Figure 2.7 also

shows the generalized mechanical stress relationship for SMAs. In this figure, σ_{MAf}, σ_{MAs}, σ_{AMs}, and σ_{AMf} are the martensite to austenite finish stress, martensite to austenite start stress, austenite to martensite start stress, and the austenite to martensite finish stress. As one can see from this figure, these stresses are dependent on the temperature of the SMA.

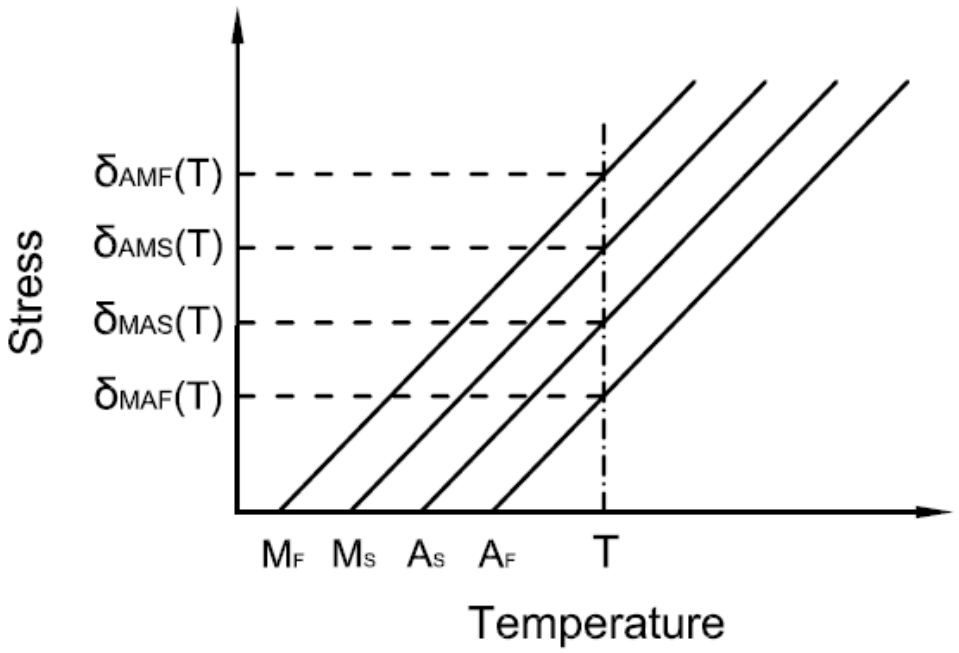

Figure 2.7: SMA phase dependency on temperature and mechanical stress

2.2.1 Shape Memory Effect

When martensite SMAs are strained beyond their elastic point a residual strain results when the stress is relieved; however, when the temperature of the alloy is raised above A_f, this strain is recovered. This phenomenon is known as the shape memory

effect (SME) and it can be used to recover, with negligible residual deformation, strains up to 8%. Figure 2.8 shows the stress-strain curve of a SMA that undergoes the SME after residual strains are accumulated. Additionally, if strain recovery due to the SME is restrained, recovery stresses up to 800MPa can be generated [Vokoun and Stalmans (1999)]. A large amount of research has been done in the field of SMAs on the SME. Some of the application that has been proposed and discussed include prestressing of concrete structures [Maji and Negret (1998)], deployment arterial stents used in human arteries [Kuribayashi et al. (2006)], and self deploying space structures [Todoroki et al. (2009)], among others.

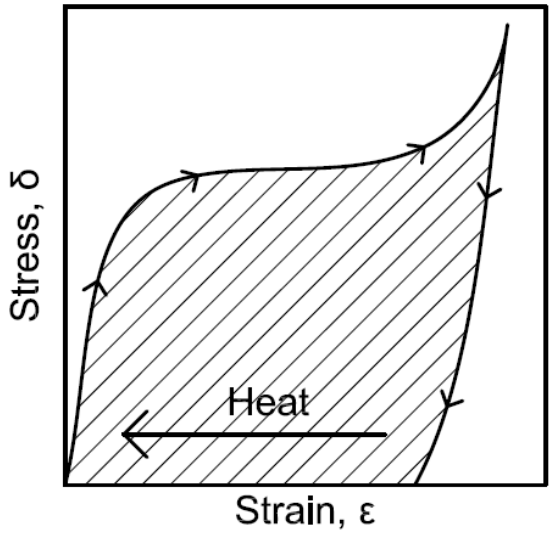

Figure 2.8: Stress-strain curve for SMA exhibiting the SME

2.2.2 Superelasticity

The other unique property of SMAs is called superelastity. This property describes how SMAs at temperatures above A_f can be strained, up to approximately 8%,

and when unloaded (with no temperature change) return to a position with no residual strain. The typical flag shaped hysteresis of superelastic SMAs is found in Figure 2.9. In this figure the transformation stresses corresponding to phase transformation are shown. From this figure, one can see that superelastic SMAs exhibit energy dissipation through hysteretic area without residual strain or damage to the material. Additionally, one can see that when loading, the stiffness of the composite is dramatically decreased during phase transformation. This decrease in stiffness has been compared to the yielding of steel.

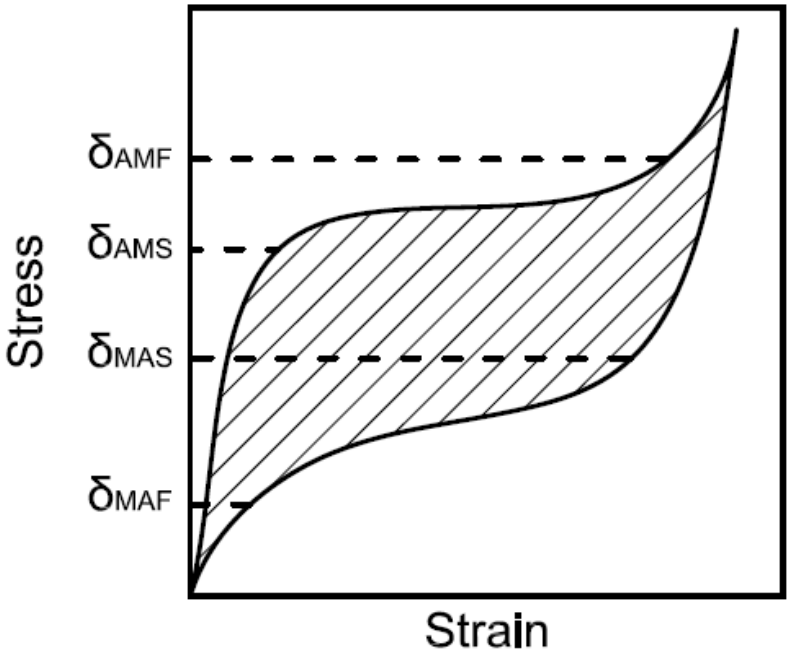

Figure 2.9: Stress-strain hystersis for superelastic SMA

2.2.3 Shape Memory Alloy Training

In practice, a superelastic SMA hysteric curve without any residual displacement, as seen in Figure 2.2, can only be achieved with trained SMAs. Trained SMAs are SMAs

that have undergone a process in which they experience numerous cycles of stress induced phase change. During cycles of stress induced phase change on a virgin superelastic shape memory alloy residual martensite is formed [Naito et al. 2001]. Residual martensite can be seen of the surface of an austenite SMA in Figure 2.10. One of the effects of the presence of the residual martensite is residual displacement. As the number of cycles is increased, residual displacements due to the formation of residual martensite continue to grow, but at a decreased rate. Eventually, a stable behavior is reached and the alloy exhibits no additional residual displacements.

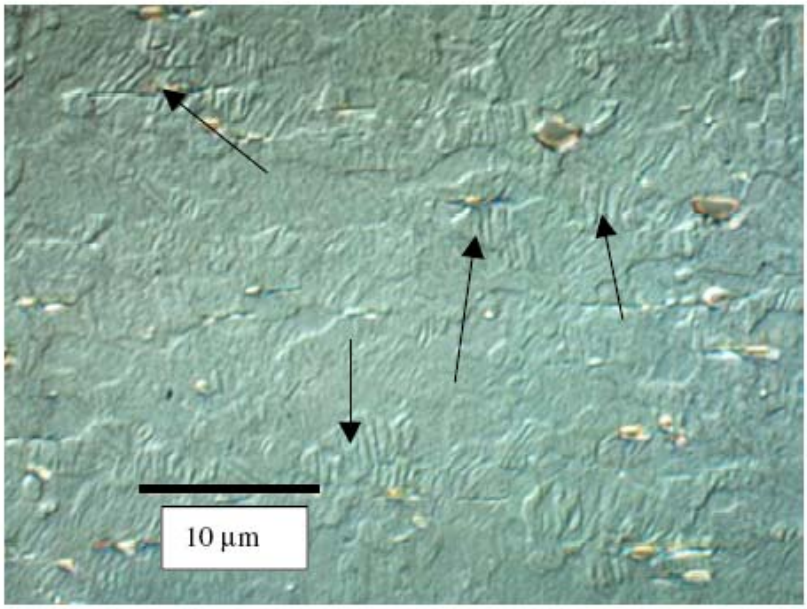

Figure 2.10: Surface of an austenite SMA with patches of residual martensite [Miller and Lagoudas (2000)]

An example of the progression of the SMA's stress-strain relationship during the training process is seen in Figure 2.3. In this figure the stress-strain relationship is seen at multiple points during training and the number of cycle of stress the SMA has been subjected to is denoted by N. This figure illustrates the above discussion; a SMA during

training will accumulate a large amount of residual displacement in the first cycles, but the amount of additional residual displacement accumulated decreases as the number of cycles increases. One can also see that due to the presence of the residual martensite, the SMA's transformation stress is lowered in this training process. While a lowered transformation stress may be a disadvantage in some cases, the benefits of a repeatable stress strain relationship outweigh this disadvantage in most cases [McCormick et al. (2005)].

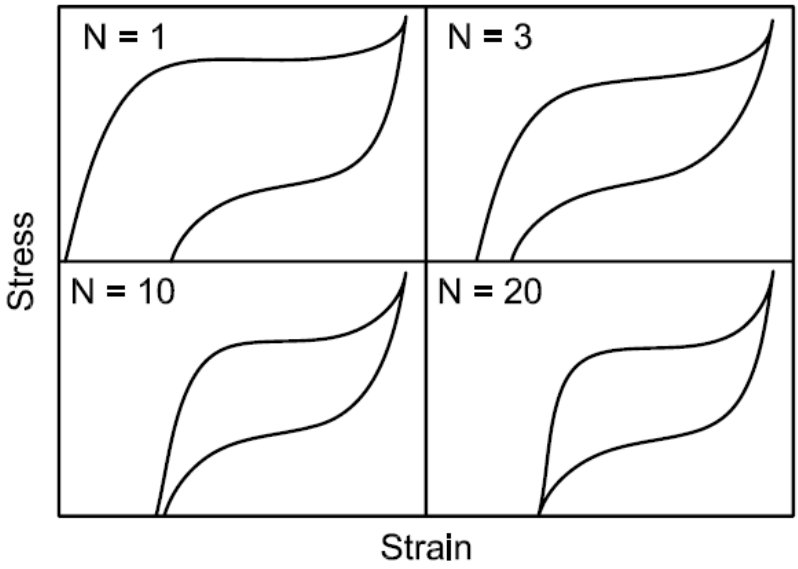

Figure 2.11: Example stress-strain behavior during SMA training over N cycles

Other training techniques can be used to achieve an SMA that exhibits the two way shape memory effect (TWSME), which is defined to be the ability of a SMA to memorize a shape at low temperatures and a different shape at high temperatures and repeatedly transition between the two when heated or cooled [Perinkins (1974)]. An example of the TWSME is seen in Figure 2.12, which shows the displacement hysteresis

due to temperature changes of an SMA wire exhibiting the TWSME. The different techniques that have been shown to result in a SMA with the TWSME include cycles of mechanical deformation, cycles of thermal loading, and cycles combining both thermal and mechanical loading [Perinkins (1974), Hebda et al. (1995), Huang and Toh (2000), Lui et al. (1999)].

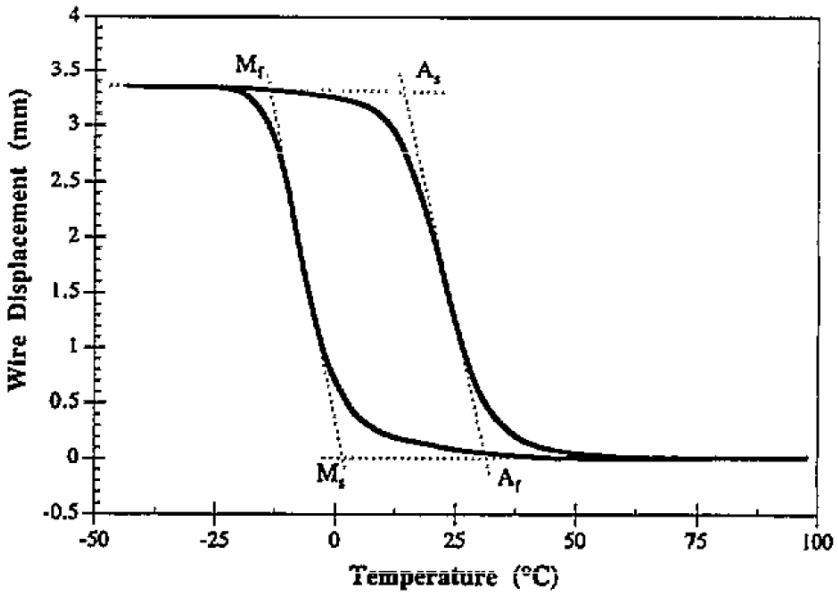

Figure 2.12: Hystersis of a wire exhibiting the TWSME [Hebda and White (1995)]

2.2.4 Modeling of SMAs

SMAs and SMA composites will be analytically modeled in this thesis; therefore, it is important to investigate how SMAs have been modeled. One of the first thermo-mechanical models of SMAs was developed by Muller (1979). This model was based on potential energy principles. Tanaka and Nagaki (1982) expanded this model by considering the temperature and stress effect on the potential energy. This model was

useful in describing both the SME and superelasticity. This model was again further expanded by Niezgodka and Sprekels (1986) and Hoffmann and Zheng (1986) who considered the dynamic response of the alloy. Unfortunately, these models proved to be impractical for design because they were based on thermo-mechanical parameters that are extremely difficult to obtain.

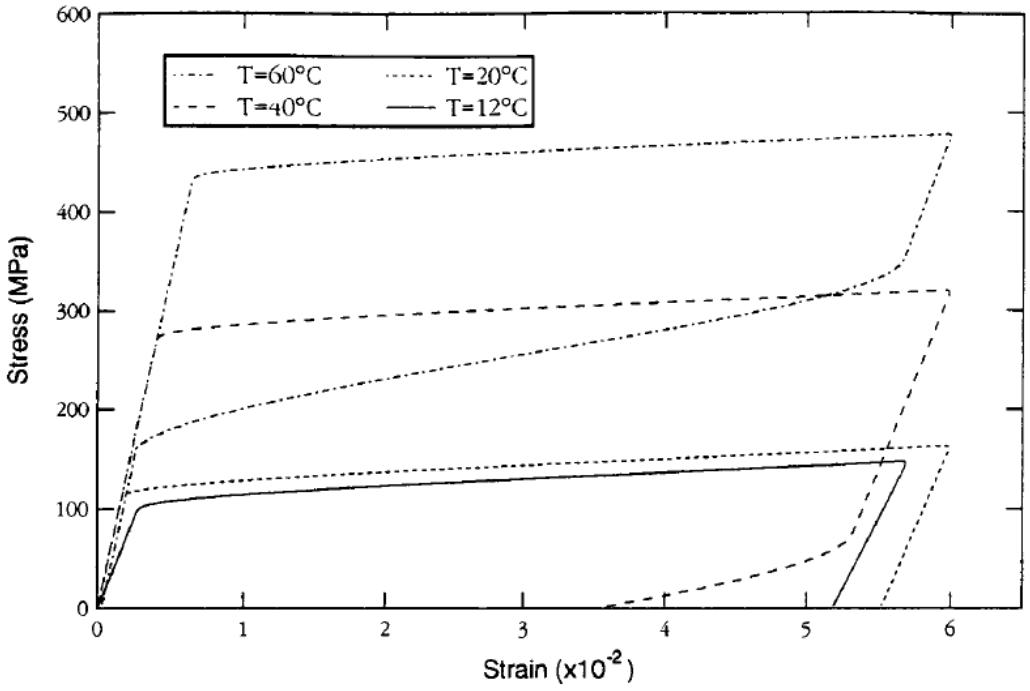

Figure 2.13: Numerial example of superelastity in Brinson's thermo-mechanical model [Brinson (1993)]

Based on the work by Niezgodka and Sprekels, as well as the rate form of the constitutive equation proposed by Tanaka and Nagaki, Liang and Rogers (1990) went on to develop a thermo-mechanical model focused on the SME. This model has the advantage of being based on the simplest possible material constants, thus making it more practical. Brinson (1993) then went on to expand this model to better capture

superelasticity. Figure 2.13 shows one of the numerical examples presented in Brinson 's paper. In this figure one can see a representation of the ability of Brinson's thermo-mechanical model to change its superelastic response in relation to the temperature. The SMA thermo-mechanical model used in SMA composites was studied by Zak et al. (2003), who compared the uniaxial version of several models. This study found that the Brinson model performed well and recommend its use when modeling superelastic SMAs in composites.

2.2.5 Nickel Titanium and SMA applications

There are many different alloys that are classified as SMAs, but the most amount of research has focused on an alloy that consists of nearly equal parts, by weight, nickel and titanium known as NiTi. NiTi was patented in 1965 by Bueler and Wiley, who discovered it through their research at the Naval Ordinance Laboratory [Bueler and Wiley (1965)]. Another common name for NiTi is Nitinol, which comes from the combination of NiTi and the abbreviation for the Naval Ordinance Laboratory, NOL. NiTi is considered by many as the most favorable SMA for most structural applications because of its excellent superelastic properties, lower sensitivity to temperature changes, excellent corrosion resistance, and high resistance to fatigue [Dolce and Cardone (2006)]. Table 2.1 provides a comparison of the properties of NiTi and other SMAs in the austenite phase. This table demonstrates the superiority of NITi to other alloys with a higher available range of yield and ultimate strengths available as well as better performance in terms of the failure elongation and amount of recoverable strain. Additionally, from this table it is seen that the properties of NiTi SMAs can vary greatly. These variations are

often the result of small changes to the SMA, such as slight shift in the Ni/Ti ratio or seemingly minor modifications to the manufacturing process. This sensitivity makes careful planning necessary to choose the SMA that is optimal for a given application.

Table 2.2: Comparison of the properties of NiTi and other SMAs in austenite phase [Janke et al. (2005)]

Property	Unit	Ni-Ti	Cu-Zn-Al	Cu-Al-Ni	Fe-Mn-Si-Cr
Young's Modulus	GPa	70-98	70-100	80-100	140
Yield Strength	MPa	100-800	150-350	150-300	200
Ult. Tensile Strength	MPa	800-1500	400-900	500-1200	650
Elongation at Failure	%	15 - 20	10 - 15	8 - 10	29
Recoverable Strain	%	8	3.5	2	3.4

Traditionally, SMAs have been used almost exclusively in high-end fields, such as the aerospace and biomedical industries. One reason for the slow development of civil engineering applications is that SMAs have historically been rather expensive. This is particularly true for NiTi, which is one of the most expensive SMAs. Consequently, low cost Cu and Fe based SMAs, such as those seen in Table 2.2, have gained some interest, despite their inferior performance. With increased overall popularity and streamlined production, the cost of SMAs has and will continue to drop, which will continue to increase the market for new applications [DesRoches and Smith (2004)]. Partially due to this decrease in cost, there has been an increase in research in the past decade into the civil engineering applications with SMAs. Some of these applications include, energy dissipating braces [Janke et al. (2005)], bridge restrainers [Andrawes and DesRoches (2007)] and deflection mitigation concrete beams through the use of embedded prestrianed SMAs [Li and Liu (2006)]. Additionally, the high cost of SMAs is one of the

motivating factors for research in the field of SMA composites, including this thesis since SMA composites can be used to exploit the beneficial properties of SMA with a reduced amount of SMAs and cost.

2.3 SMA COMPOSITES

SMA composites are a material type that is composed of polymeric matrix material reinforced with SMAs with or without additional conventional fibers. Figure 2.14 shows a schematic of a typical SMA composite. The polymer matrix materials that have been studied in SMA composites include epoxy, polyester, and vinylester. Some of the first research involving SMA composites was performed by Roger and colleagues at Virgina Tech in the late 1980s and early 1990s [Rogers (1990); Rogers et al. (1991); and Paine and Rogers (1994)]. Their research focused mainly on vibration control of a composite with embedded SMA wires. Since this initial research into SMA composites, a wide variety of polymer matrix SMA composites have been studied, including a great deal of research on SMA composites that utilize SMA wires. Although wires are most prevalent reinforcement type, SMA ribbons, foils, fibers, and particles have also been studied as composite reinforcement [Jonnalagadda et al. (1998), Wei et al. (1998), Zhang and Ni (2007)]. There are multiple different reinforcing materials that have been studied to be used as reinforcement with SMAs in composites, most of which are conventional fibers, such as carbon, aramid, and glass fibers.

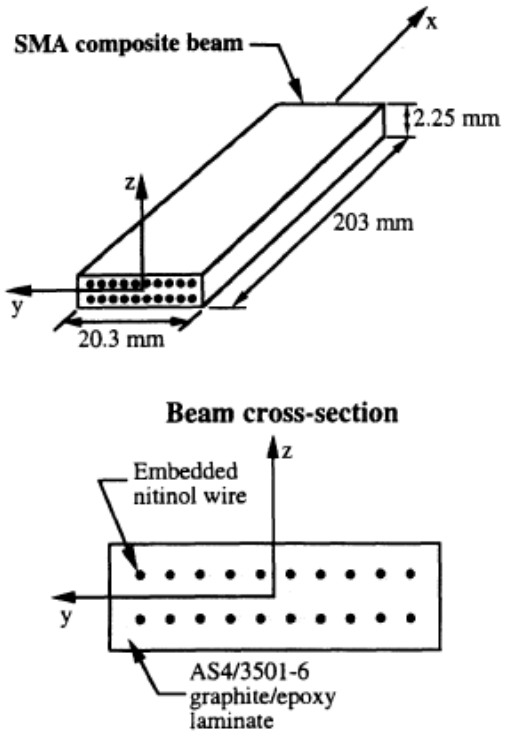

Figure 2.14: Schematic view of a typical SMA composite [Hebda et al. (1995)]

2.3.1 Manufacturing of SMA Composites

The manufacturing process of SMA composites varies considerably due to the different types of matrices, SMA reinforcement, additional reinforcing materials, and the intended usage of the composite. Differences also arise due to the fact that most SMA composites are now created in the research environment where standardized manufacturing techniques for particular SMA composite may not be established or utilized. A review of SMA composite manufacturing processes can be used to identify common techniques and challenges that arisen.

One common manufacturing technique for SMA composites was discussed by Pappada et al. (2008). In this paper the manufacture of an SMA composite used for

impact resistance was discussed. The SMA composites in this paper consisted of a vinylester resin reinforced with superelastic SMA wires and glass or carbon fabric. To manufacture these composites, specialized frames were built to secure the SMA wires and ensure correct wire spacing. Sheets of fabric reinforcement were then placed between the layers of SMA reinforcement and the process was repeated until the composite had a total of 4 layers of SMA wire reinforcement. To create a composite between these two reinforcing materials vinylester resin was added using vacuum assisted infusion.

The above manufacturing technique is similar to a common manufacturing technique for SMA composites utilizing the shape memory effect, which was discussed by Michaud et al. (2002). In their paper they discussed, in detail, the manufacturing of an SMA-FRP composite that consisted of an epoxy matrix reinforced with prestrained SMA wires and Kevlar fibers that was used for vibration control. The prestrain in the SMA wires required the use of a device to apply and hold the desired prestaining throughout the manufacturing process. Without a device to hold the prestrain in the wires, the prestraining would be released due to heat during the manufacturing and the result would be a SMA composite without prestraining. Figure 2.15 shows similar frame used by Sittner and Stalmans to apply this prestrain. Once the prestraining was applied to the SMA wires, epoxy Kevlar prepregs were then sandwiched between the SMA wires. The assemblage was then cured at 70°C for 12 hours and post cured at 140°C for up to 4 hours in an autoclave under vacuum. Once the post curing was finished and the sample was cool, the SMA composite was removed from the frame and was ready for use. A microscopic cross-section of the finished SMA composite is seen in Figure 2.16.

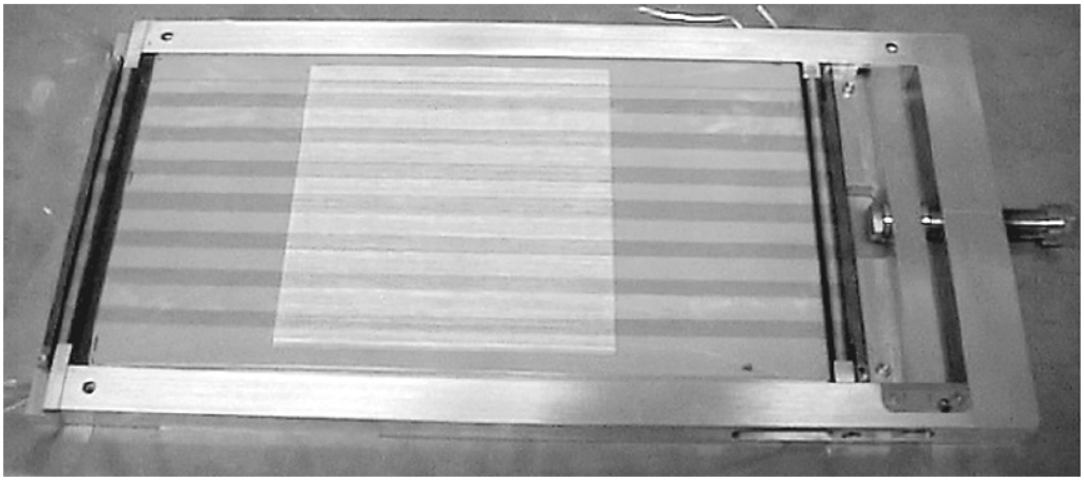

Figure 2.15: Frame used to prestrain SMA wires during the manufacturing of a SMA composite [Sittner and Stalmans (2000)]

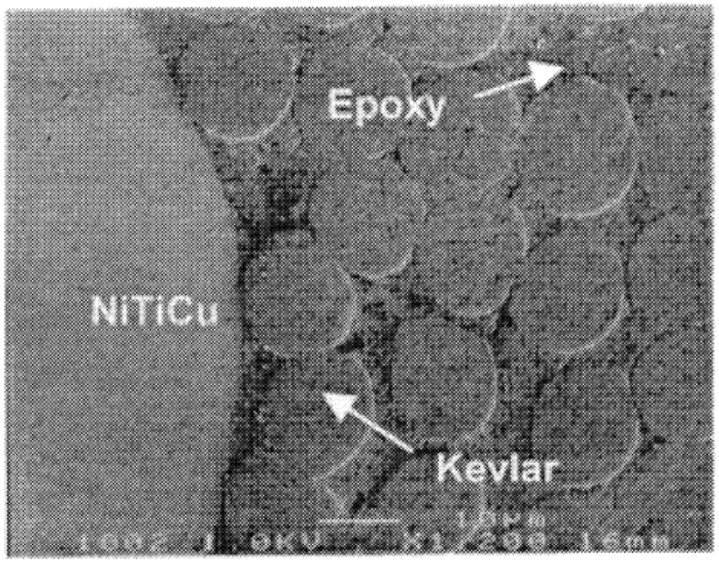

Figure 2.16: Cross-section of an SMA composite [Michaud et al. (2002)]

Some of the early research on SMA composites produced poor results; especially when vacuum cure techniques were not utilized [Hebda et al. (1995)]. These poor results have often been attributed to poor interfacial bonding of the SMA wires Xu et al. (2002),

which is thought to occur because voids in the composite have been observed to congregate near the SMA wires. This problem and, specifically, the void content of a SMA composite in relationship to the position of the SMA wires was studied by Hebda et al. (1995). The SMA composite in this study consisted of graphite/epoxy laminates with 0.2mm SMA wires. This composite was vacuum bagged and cured in an autoclave for a total of 5 hours with the maximum temperature of 177°C. Figure 2.17 shows the void content of the SMA composite in relation to the position of the SMA wires. From this figure one can see that the void content increases dramatically near the wires. In this composite the maximum void content near the wires was approximately 31%, while the average void content of the composite was only 7.3%

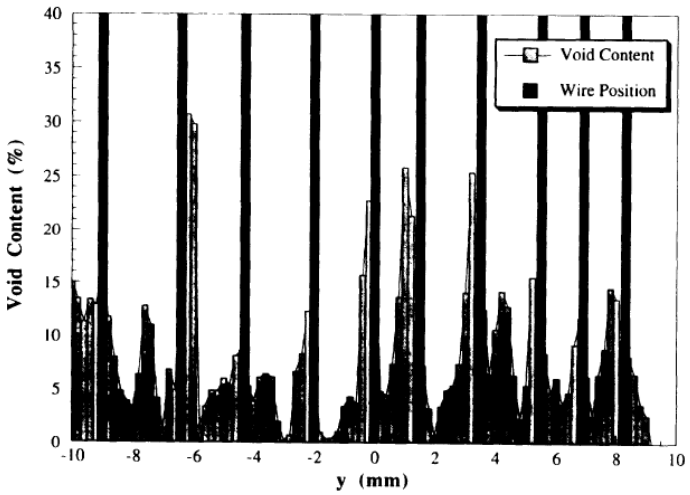

Figure 2.17: Void content of an SMA composite relative to the position of the SMA wires [Hebda et al. (1995)]

Xu et al. (2002) investigated using small diameter SMA wires to improve the interfacial bonding in SMA composites with the study of a composite reinforced with ultrathin, 50 μm diameter, SMA wires and carbon fibers. From this study it was found that the use of ultrathin SMA wires nearly eliminated voids near the SMA wires when

conventional reinforcement in the composite ran parallel to the wires and greatly reduced voids when the reinforcement ran perpendicular to them. This is demonstrated in Figure 2.18 which shows cross-sections from SMA composites with 50 μm diameter SMA wire reinforcement. In this figure the SMA composite with SMA wires and carbon fibers oriented in the same direction has virtually no visible voids, while the composite with SMA wires and carbon fibers orientated in opposite directions has some visible voids.

Surface treatments designed to increase the interfacial bonding of the SMAs in the composite were studied by Jonnalagadda et al. (1997) and Smith (2004). Jonnalagadda investigated three possible techniques for increasing the interfacial bond strength of embedded SMA wires: sand blasting, acid etching, and hand sanding. From this study it was found that sand blasting significantly improved the bond shear strength, while both acid etching and hand sanding lead to decreases in bond shear strength.

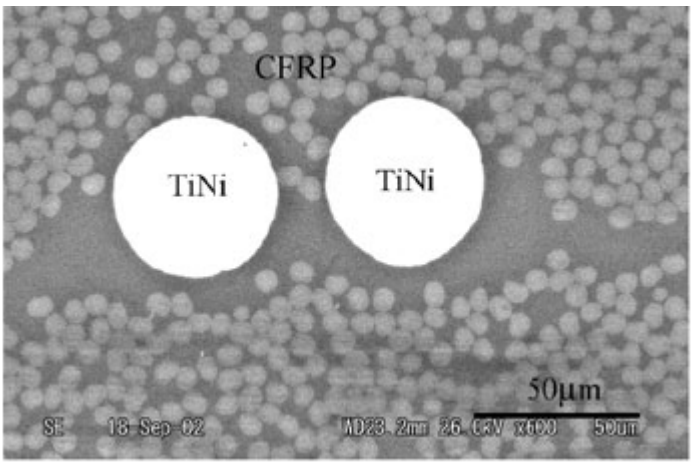

(a)

Figure 2.18: Cross-sections of SMA-FRP composites (a) carbon fibers and SMA wires orientated in the same direction (b) carbon fibers and SMA wires orientated in perpendicular directions [Xu et al. (2002)]

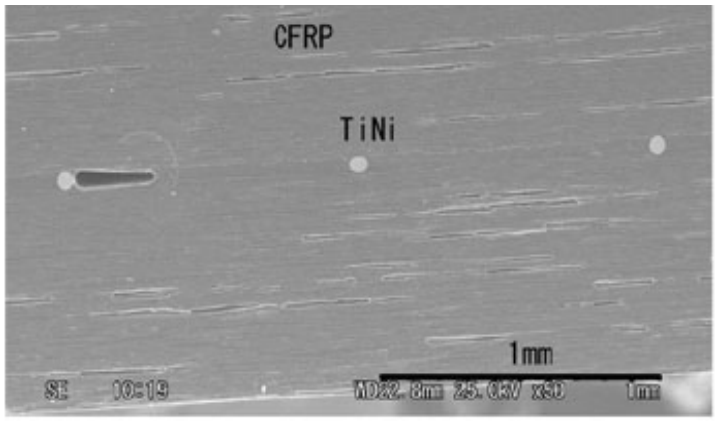

(b)

Figure 2.18 (cont.)

While the above manufacturing techniques are all designed for SMA composites with continuous pieces of SMA reinforcement, such as wires, some SMA composites utilize many discrete pieces of SMAs. Zhang and Ni (2007) detailed a process used to manufacture a SMA composite that consisted of an epoxy matrix reinforced with either small SMA particles (diameter ≈ 425 μm) or short SMA fibers (length = 1.5-2 mm). In this process the SMA reinforcing material combined with the epoxy resin and vacuum dried for 20 minutes. After drying, the mixture was then poured into molds and cured at room temperature for 24 hours. Finally, the composite was heated to 140°C over a period of 10 hours and the SMA composite layer was bonded to a bulk epoxy layer. The SMA content of the specimens varied from 1% to 27.4%, by weight. Figure 2.19 shows some of the small particle and short fiber SMA composites manufactured with this process.

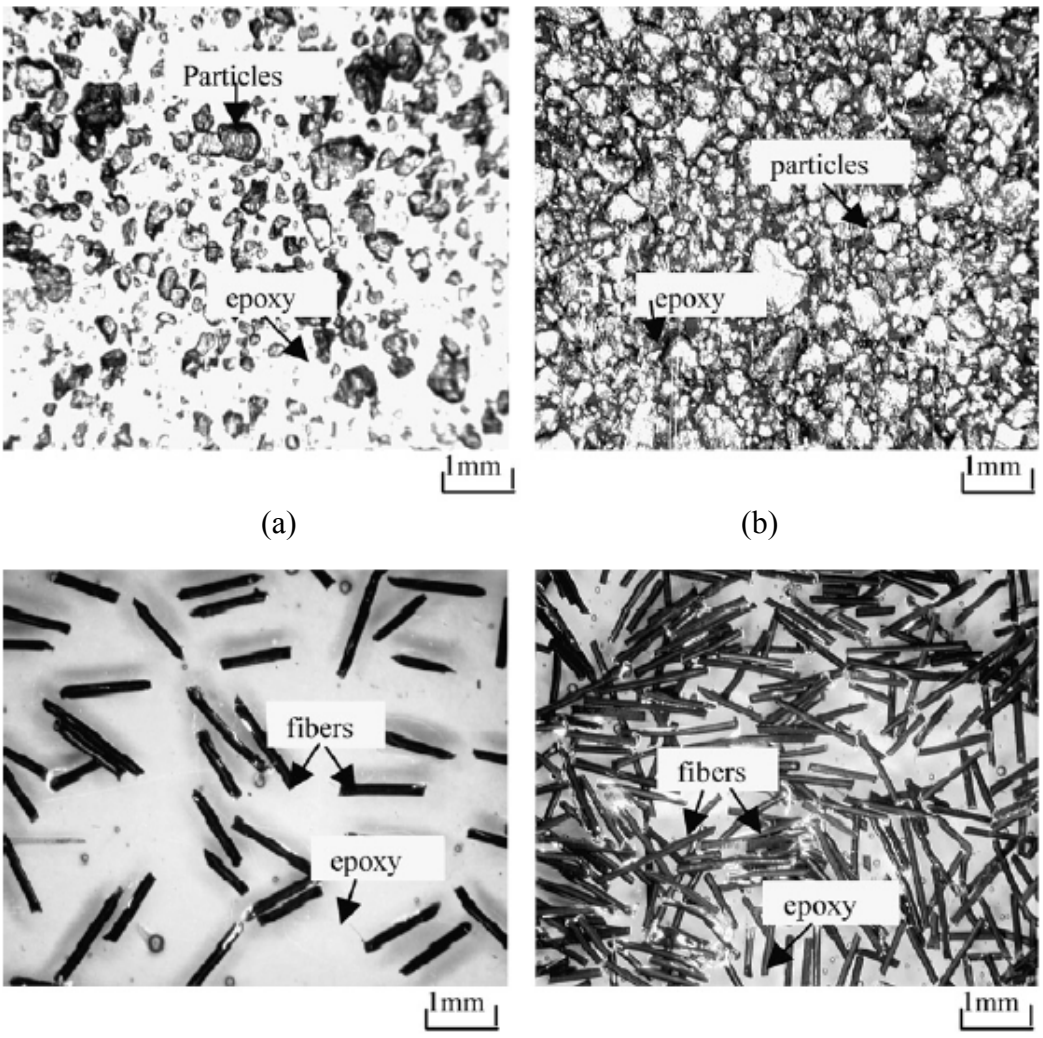

Figure 2.19: Short fiber and small particle SMA composites
a) 5.1 wt% small particle SMA composite b) 27.4 wt% small particle SMA composite
c) 5.1 wt% short fiber SMA composite d) 27.4 wt% short fiber SMA composite
[Zhang and Ni (2007)]

2.3.2 SMA Composite Applications

There are numerous applications for SMA composites that have been proposed. These include active and passive vibration control, self-healing composites, actuation,

and impact damage resistance. Most of the composites used for these applications are designed to exploit the SMA's shape memory effect or superelasticity.

Vibration Control

Vibration control of composites using embedded SMA wire was one of the first applications researched for SMA composites. Since that time many papers, including Baz et al. (1990), Rogers (1990), Rogers et al. (1991), and Lau (2002), have been published on the subject. There are two main types of vibration control with SMA composites: active and passive control. Passive vibration control with SMA composites was demonstrated by Lau 2002. In this paper, it was shown that the addition of SMAs into a composite was able to change the natural frequency of the composite and that the natural frequency can be further changed by prestraining the SMAs in the composite. Additionally, this paper showed that the addition of SMAs into a composite can affect the damping ratio of the composite. This is shown in Figure 2.20 which details the damping ratio of an SMA composite in relation to the applied constant current in the embedded SMA wires [Lau (2002)]. The specimens in this test were SMA composite beams that contained martensitic SMA wires that were prestrained to 4%. When tested, the beams had fixed-fixed boundary conditions. From Figure 2.20 one can see that the higher constant voltage levels had the effect of increasing the damping ratio due to the phase transformation of the SMAs into austenite.

On the other hand, active control with SMA composites generally involves a control program designed to activate the SME in a way that reduces vibrations. An example of this is the SMA composite developed for active control by Baz et al. (1990).

This composite consisted of two SMA actuators combined with a flexible beam. The SMA actuators were used to actively damp out vibrations by using a control program to activate the SME in either actuator. An example of the results from this study are seen in Figure 2.21, which compares controlled and uncontrolled displacement response of the SMA composite beams subjected to a stepped tip displacement. As one can see from this figure, the actively controlled SMA composite was able to damp out the vibrations faster than the uncontrolled specimen.

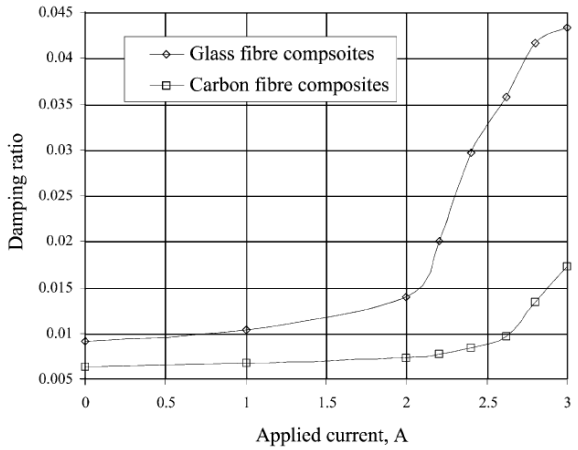

Figure 2.20: The damping ratio of an SMA composite in relation to the current in the embedded SMA wires [Lau (2002)]

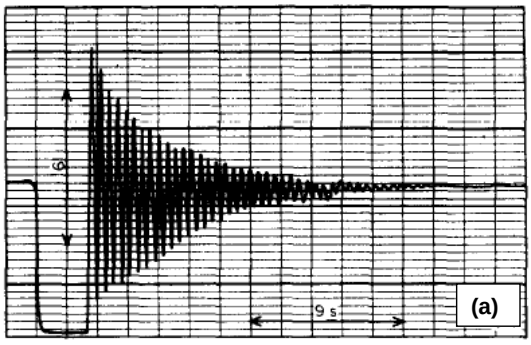

Figure 2.21: The response of SMA composite beams subjected to a stepped tip displacement (a) uncontrolled (b) actively controlled [Baz et al. (1990)]

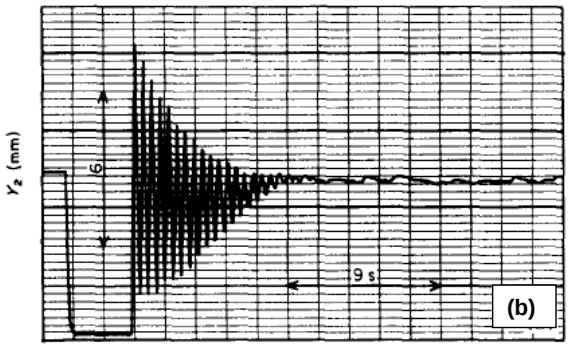

Figure 2.21 (cont.)

Self Healing SMA Composite

Burton and Gao (2006) and Hamada et al. (2003), among other researchers have explored exploiting the SME in order to create a composite that has self healing properties. The research by Burton et al. consisted of exploring self-healing SMA composites with a series of finite element simulations. The SMA composite was modeled with one dimensional SMA wires contained within a multidimensional brittle elastoplastic metal matrix. The member was tested in axial tension with and with out an initial notch in the matrix perpendicular to the load. When the composite was modeled with an initial notch this tensile load caused the notch to propagate into a crack. With the matrix material cracked in the simulation, the composite was heated and the SME of the SMA reinforcement was used to close the crack. Additionally, the matrix softening at higher temperature allowed the crack to fully close at the high temperatures needed to activate the shape memory effect. Without this softening, the matrix would contain residual stress. The results of this study showed that the recovery force of the

composite's SMA reinforcement was capable of closing cracks in the composite. Figure 2.4 shows a diagram of the crack propagation and closure.

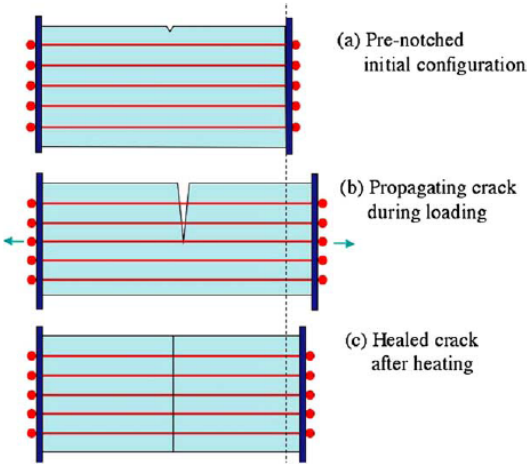

Figure 2.22: Crack propagation and healing of an SMA composite [Burton and Gao (2006)]

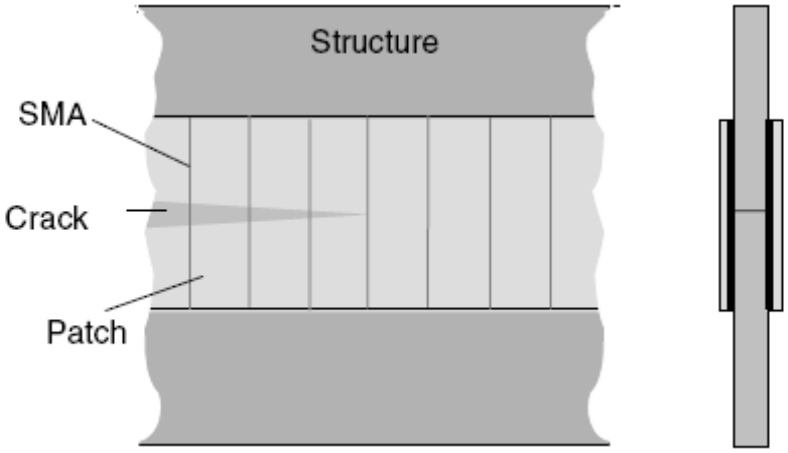

Figure 2.23: Schematic drawing of how a SMA composite could be applied to help close a crack in a structure [Wang (2002)]

Another type of SMA composite that uses the SME to repair a structure was studied by Wang (2002). This composite consisted of prestrained SMA wires embedded in a sheet of matrix material, with or without additional fiber reinforcement. These sheets

were designed to be bonded with an adhesive to areas in need of repair, such as a crack in a plate. Once bonded, the composite would be heated and the SME would be activated allowing the composite to repair the damage area. Figure 2.23 shows a schematic drawing of how a SMA composite patch could be applied to a structure to help repair a crack.

Actuation

The ability of an SMA to recover a great amount of residual strains through the SME has inspired researches to look for ways to utilize SMA composites to create actuators. There have been two main ways that have been proposed to created SMA composites that actuate, the first is through the use of one-way SME, and the second utilizes TWSME. The shape memory effect of SMAs alone has been discounted by some as not a viable actuator [Cho and Kim (2005)]. The reason for this is that the shape memory effect provides only one-way actuation; once the memorized shape is recovered the SMA can not automatically assume any other shape. SMA composites, however, can be designed to be two-way actuators. One method for enabling an SMA composite to become a two-way actuator, is to design an elastic base matrix material such that its glass transition temperature, T_g, is between the SMA transformation temperatures M_s and A_s. This is significant because at temperatures above T_g, the matrix material will have a dramatic reduction in stiffness. With this requirement fulfilled the SMA composite can acquire two shapes in a repeatable fashion. In this process, the first shape is acquired when the SMA composite is heated up past A_f. This corresponds to a temperature

above, T_g ; consequently, the epoxy decreases in stiffness and allows the SMA to recover a bent up shape. When cooled, the matrix stiffened in this shape, thus helping to maintain it. The second shape is acquired when the SMA composite is heated past T_g but below A_s. When this occurs the SMA relaxes and the epoxy lets the composite acquire and keep a nearly flat shape when the temperature is lowered. Figure 2.24 shows an example of a two-way SMA composite actuator researched by Sterzla et al. (2003). This figure shows the evolution of the SMA composite's shape with temperature changes. Additionally, Figure 2.25 shows the two stable shapes of this type of two way SMA composite actuator.

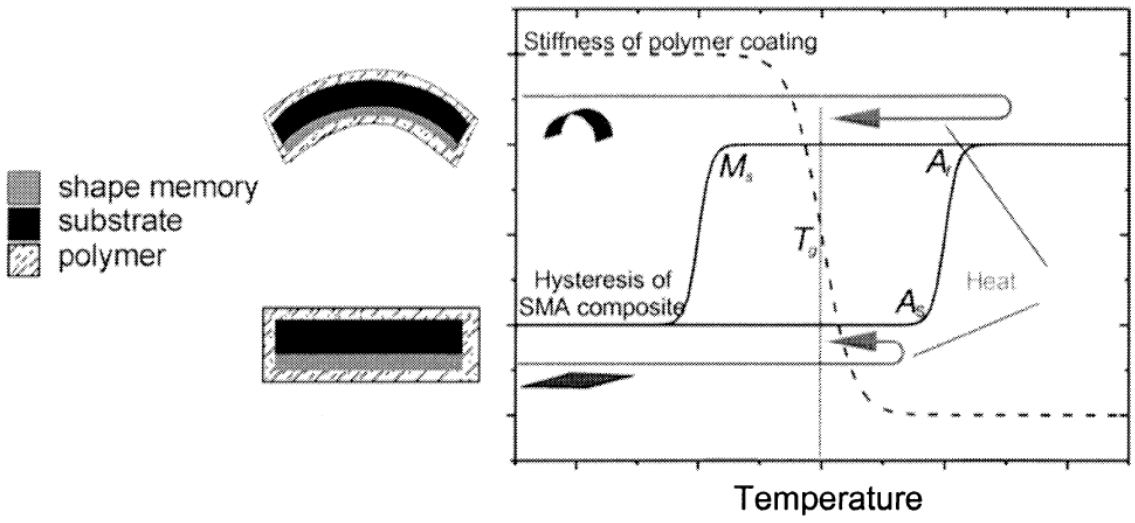

Figure 2.24: SMA composite demonstrating two-way actuation [Sterzla et al. (2003)]

Another type of SMA composite actuator was discussed by Hebda et al. (1995). The SMA composite in this study consisted of SMA wires embedded in an epoxy matrix with graphite fibers. Prior to embedment in the composite, the SMAs were trained to

exhibit the TWSME; therefore, the SMA composite was able to display two-way actuation when heated then allowed to cool. Additionally, by using SMAs that were trained for the TWSME, the need to prestrain the SMAs in the composite was eliminated. This resulted in a much less complex manufacturing process. The composites created in this study showed good ability to actuate, due to up to 4% strain recovery in the SMA embedded in the composite.

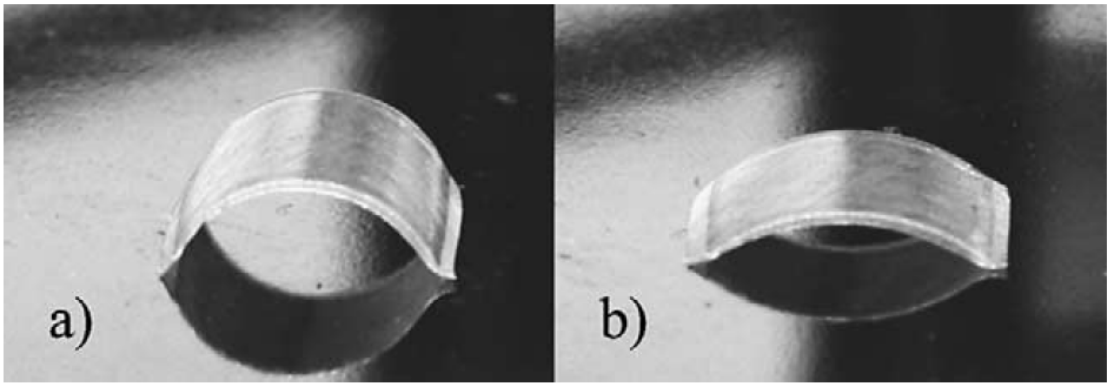

Figure 2.25: Two-way actuating SMA composite (a) shape after high temperature cycle (b) shape after low temperature cycle [Winzek et al. (2004)]

SMA Composite for Impact Damage Resistance

SMA composites have also been studied for applications in extreme loading situations. Several researches, including Tsoi et al. (2002), Pappada et al (2008), and Paine and Rodgers (1994) Paine and Rodgers (1995) have studied the embedment of SMA wires into an FRP composite to create an SMA composite with better capacity for mitigating the effect of an impact. In the study by Paine and Rodgers (1995) the impact damage resistance of SMA composites was studied at both low and high velocities. The

SMA composite samples used for this study were composites of epoxy and layers of graphite or fiberglass reinforcement each with an exterior layer of NiTi SMA wires and epoxy bonded to one face (see Figure 2.26 for a schematic of the specimens). Comparisons were made to the performance of graphite and epoxy reinforced composites with an exterior layer of aluminum wires and epoxy on one face, as well as graphite or fiberglass composites that do not have an additional layer of wire and epoxy. From this study it was found that the SMA composite energy required for an impact to cause perforation of the composite was increased by up to 100% compared to conventionally reinforced specimens. This increase in perforation energy due to the addition of SMA wires was also observed to increase with increased speed of the impact. Additionally, this study discounted the possibility that such increases could be obtained by embedding any type of metallic wire in the composite, which was shown by comparison of perforation energy of the aluminum wire reinforced composite and conventional composite, where almost no increase is observed. A sample of the result of this study is seen in Figure 2.27 where the energy dissipated in high velocity impact testing is presented. In this figure the first bar for each composite type shows the amount of energy dissipated, while the second and third bars show the volume and density normalized values, respectively. As discussed above, this figure shows the superiority of SMA composites in dissipating impact energy when compared to conventional FRP composites and aluminum wire reinforced composites.

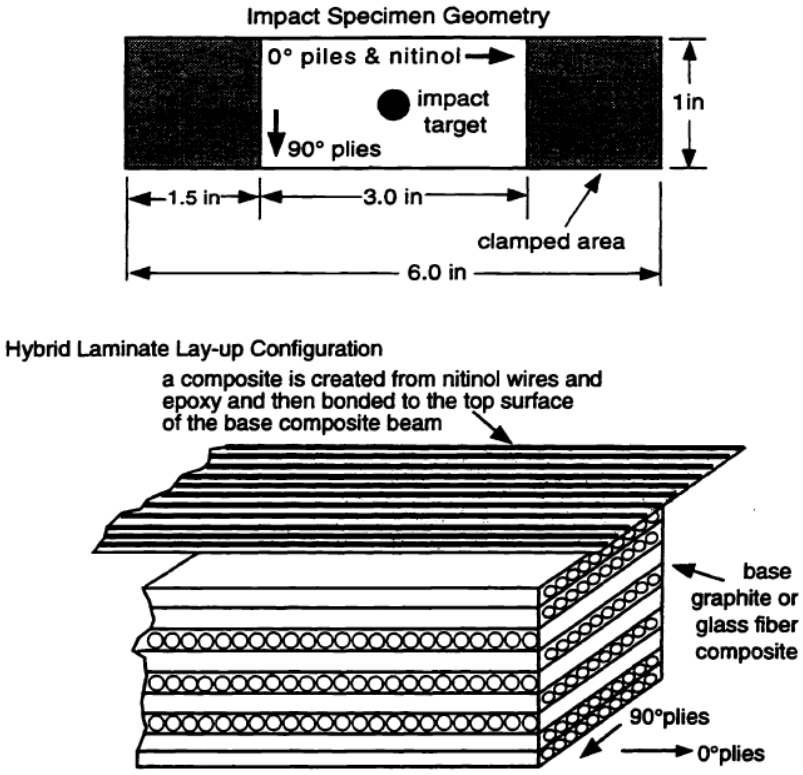

Figure 2.26: SMA composite specimens created for impact testing [Paine and Rodgers (1995)]

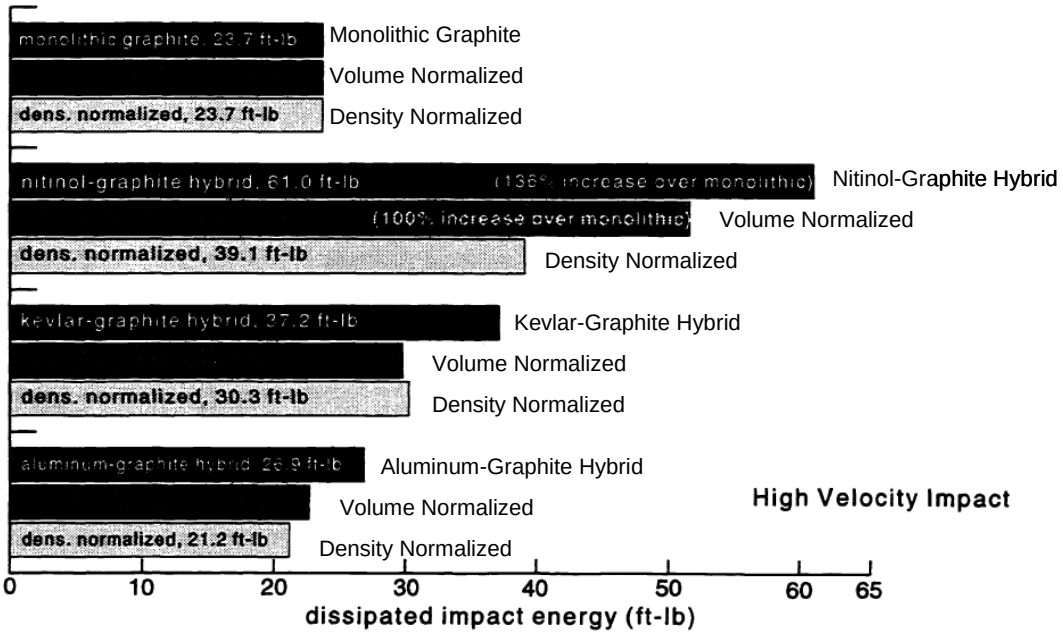

Figure 2.27: Energy dissipated in high velocity impact testing of various composite sheets [Paine and Rodgers (1995) figure annotated for clarity]

CHAPTER 3:

SMA-FRP COMPOSITES EXPERIMENTAL TESTING AND MODELING

The constitutive behavior of SMA-FRP composites was examined in this chapter and compared with that of conventional FRP composites. In this chapter experimental tests conducted on coupons made of SMA-FRP and Glass-FRP (GFRP) composites are presented. The experimental results are used as a basis for a phenomenological model that was developed to describe the behavior of SMA-FRP composites. This model is then extended so that the effect of prestraining of the SMA wires in the composite could be studied.

3.1 MANUFACTURING AND TESTING PROCEDURES

The SMA-FRP coupons used in this study were manufactured by laying out sheets of bidirectional fiberglass cloth, saturating the E-Glass fiber cloth with epoxy resin, and running 0.5 mm diameter superelastic SMA wire in between layers of the fiberglass cloth with the wires orientated along one of the primary directions of the fibers. The number of SMA wires used in the composite was designed to create coupons with fiberglass to SMA ratios of 100/0 (GFRP) and 75/25 (SMA-FRP), by volume. After curing at room temperature for more than 24 hours, 250 mm long by 15 mm wide coupons were cut out of the sheet. The coupons were cut such that the SMA wires were orientated longitudinally down the length of the coupons. To prevent failure of the specimen at the point of contact with the load frame's grips, 56 mm long hard plastic tabs were attached with epoxy to the coupon's both ends. The geometry of the specimens and

tabs were prepared according to the specifications laid out in ASTM specification D3039 (ASTM 2008). Figure 3.1 shows the SMA-FRP and GFRP coupons used in the tests and Figure 3.1 shows a schematic of an SMA-FRP coupon. The coupons were tested in tension quasi-statically in cycles using an 89 kN uniaxial servo-controlled hydraulic frame. The test setup for these coupons is seen in Figure 3.3. Testing of the samples consisted of cycles of tensile strain where the maximum strain was increased by 0.5% each cycle. In addition, the SMA wires used in the tests were first tested on a smaller scale machine to determine their constitutive behavior.

Figure 3.1: FRP composite coupons used in the study (a) GFRP (b) SMA-FRP.

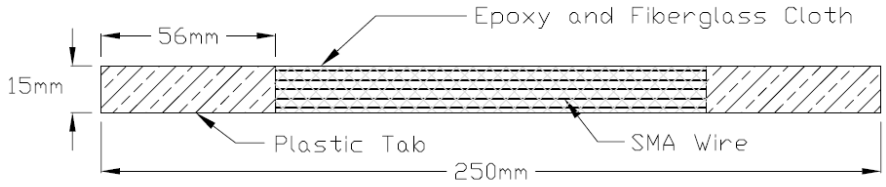

Figure 3.2: Schematic drawing of an SMA-FRP coupon

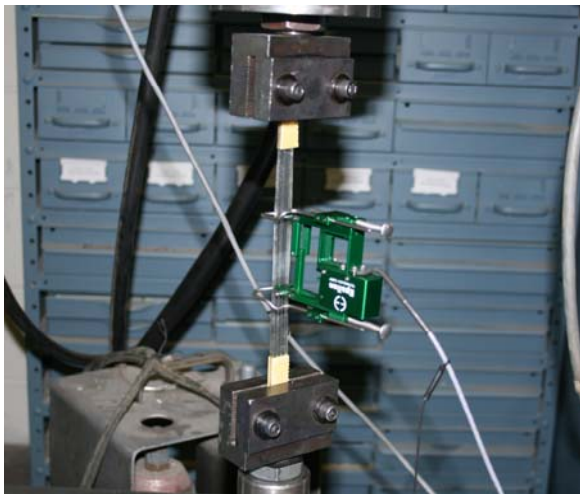

Figure 3.3: SMA-FRP coupon in testing frame with extensometer attached

3.2 RESULTS AND DISCUSSION

Figure 3.4 presents the results of the tests conducted on GFRP, SMA-FRP, and SMA wires. The GFRP behavior depicted in Figure 3.4a was linear elastic with an average modulus of elasticity and failure strain of 21 GPa and 1.7%, respectively. The SMA wires stress-strain behavior shown in Figure 3.4b confirms the flag-shape typical of superelastic SMAs. The austenite to martensite starting transformation stress is roughly 600 MPa and the strain at which stress transformation occurs is about 1%.

Figure 3.4c shows the stress-strain behavior of the tested SMA-FRP. The response of the SMA-FRP is linear elastic until approximately 1.0% strain. At this point SMA phase transformation initiates. The stiffness of the coupon after this point decreases due to the reduction in the SMAs modulus during phase transformation (see Figure 3.4b). When the SMA-FRP was loaded cyclically within strain levels below the fiberglass ultimate strain, the composite exhibited a capability to dissipate energy, which is evident by the hysteretic area enclosed within the stress-strain curve.

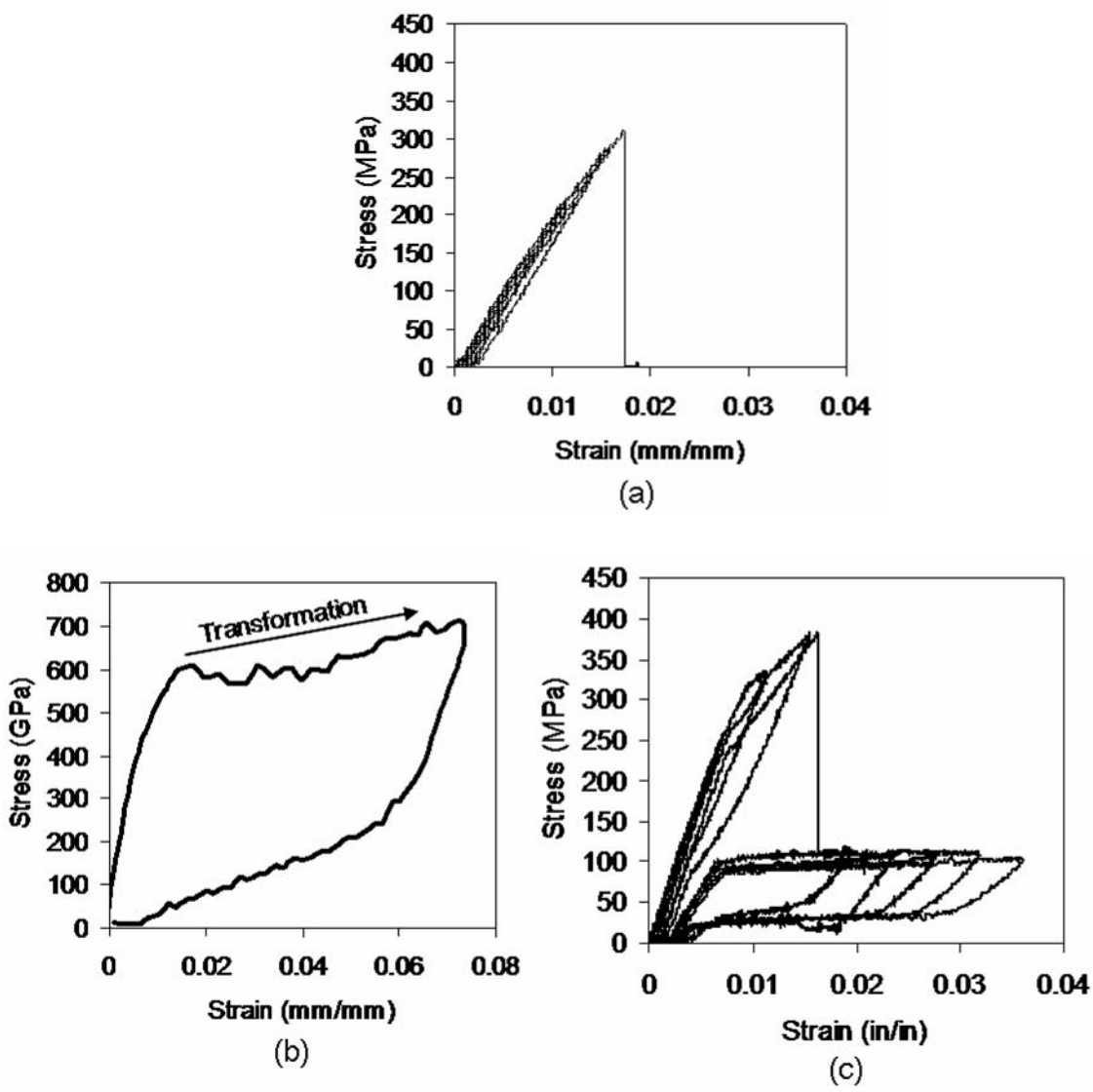

Figure 3.4: Experimental stress-strain curves of
(a) GRFP coupon (b) SMA wires (c) SMA-FRP coupon.

In the cycles leading up to the rupture of the glass fibers, the amount of energy the SMA-FRP composite dissipated through hysteretic area was 2.6 times larger than the amount of energy dissipated by the GFRP composite. When the average strain in the composite reached 1.63% the fiberglass and epoxy matrix of the composite ruptured,

which resulted in a significant loss of capacity without failure due to the still intact SMA wires. After this point, the behavior of the composite was dominated by the SMAs and further cyclical loading of the specimen produced large amount of energy dissipation due to the hysteretic behavior of the SMA. The specimen was strained until about 3.8%, at which the test was stopped. Due to the great strain capacity of SMAs, failure of the specimen was not observed.

As one can reason from the test results presented, the amount of energy that can be dissipated before the rupture of the fiber reinforcement is dependent on the difference in the strain at which the rupture of the fiberglass reinforcement occurs and the strain that SMA phase transformation begins. The larger this difference, the greater potential for energy to be dissipated before fiberglass ruptures. Consequently, more energy dissipation would be observed in the SMA-FRP coupons if the fiberglass in the composite ruptured at a higher level of strain.

From Figure 3.4c it can be seen that residual displacement accumulated during the test of the SMA-FRP composite. This residual displacement is undesirable since it reduces the ability of the composite to remain elastic. A major component of the residual displacement is likely due to the fact that the SMA wires were untrained. Training of SMAs wires similar to those used in the SMA-FRP composite coupons was performed; the stress-strain result from this test is seen in Figure 3.5. In this figure one can see that after 10 cycles of training, a repeatable stress-strain has been obtained. Additionally, it can be seen that a substantial amount of residual strain of approximately 1.6%, has accumulated in those 10 cycles. Consequently, it can be concluded that with the use of

trained SMAs much of the residual displacement observed in the SMA-FRP coupon tests could be eliminated.

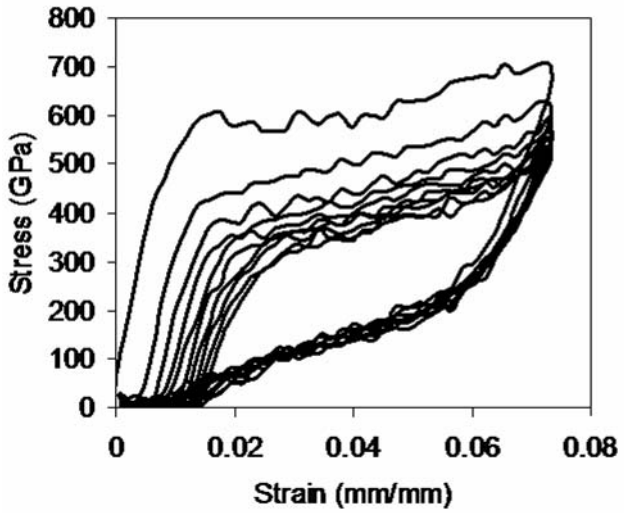

Figure 3.5: SMA stress-strain curve from 10 cycles of training.

3.3 ANALYTICAL MODEL

In order to further explore the behavior of SMA-FRP composites, a simplified analytical model was developed using the software MATLAB. In this model the SMA-FRP composite is represented by 3 parallel springs, which have material properties corresponding to the epoxy matrix, fiber reinforcement, and SMA reinforcement. This model does not take into account length effects and instabilities, such as buckling or material defects such as the existence of voids in the composite. The model was analyzed cyclically in tension in a manner similar to the experimental test procedure. To account for the changes in the stress-strain properties of the initially untrained SMA due the cyclic loading, the SMA properties were updated after the rupture of the conventional fibers to match the trained SMA experimental results shown in Figure 3.5. To verify the

accuracy of the analytical model, the analytical and experimental results were depicted in Figure 3.6. The figure indicated that the analytical model is capable of closely predicting the initial stiffness, rupture stress and strain, and the post-rupture behavior. Given the demonstrated accuracy of this model, it will be used to perform a parametric study of the behavior of SMA-FRP in a subsequent section of this thesis.

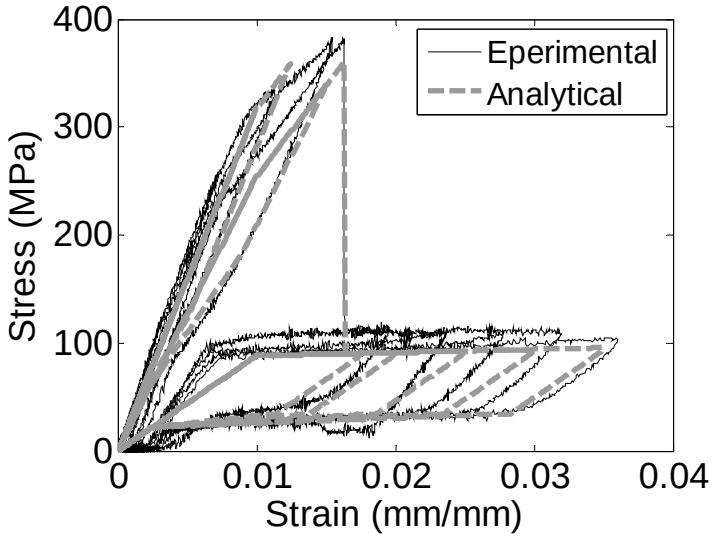

Figure 3.6: Experiment and analytical comparison of SMA-FRP stress-strain behaviors.

3.4 PRESTRAINED SMA-FRP COMPOSITES

One of the techniques that has been studied analytically to enhance the ductility and damping characteristics of the SMA-FRP composite is through the prestraining of the SMA wires. Prestraining of the SMAs is beneficial since it lowers the strain of the composite needed to reach the transformation strain of the SMA, which increases the composite's potential for energy dissipation. Additionally, the lowered transformation strain of the composite increases its ductility (rupture strain / yield strain). As

demonstrated by Figure 3.7, there will be some losses in the prestraining due to elastic shortening when the composite is allowed to come to equilibrium with the prestraining. In this state of equilibrium, the average stress in the composite is zero, but the SMA reinforcement is in a state of tension and the epoxy and conventional fiber reinforcement are in compression. The compressive strain in the matrix is beneficial since it delays the rupture of the conventional fibers.

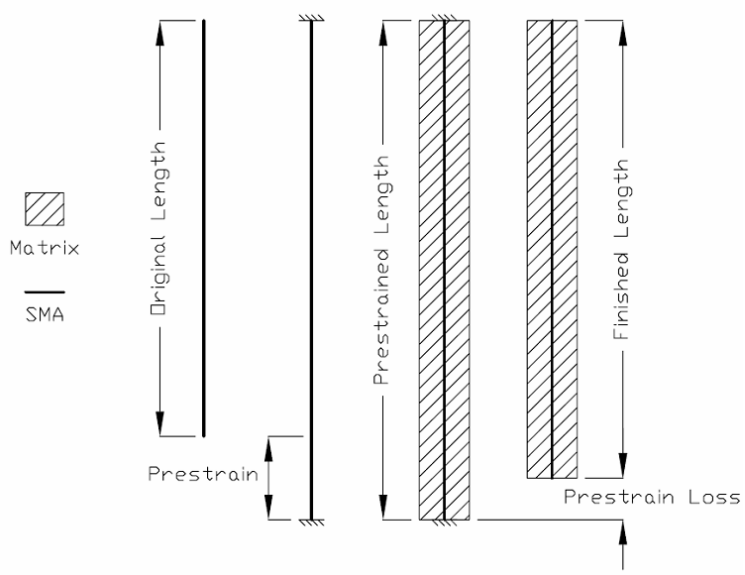

Figure 3.7: Prestraining of SMA wires in SMA-FRP Composite.

The behavior of SMA-FRP composites with prestrained SMAs is demonstrated with an analytical example using the MATLAB model, which was described in the previous section. In this example the properties of the conventional fibers and epoxy are the same as previously used for the experimental comparison, and the SMA model is matched to the behavior of the trained SMA. Figure 3.8 shows a comparison of the behavior of a SMA-FRP with 75% fiberglass and 25% trained SMA reinforcement with

and without prestraining to 1% strain. From the figure, one can see prestraining results in reducing the transformation (yield) strain from 1.0% to 0.35%, and increasing the rupture strain from 1.63% to 1.97%. Furthermore, the amount of hysteretic energy dissipated prior to the rupture of the fiber reinforcement increases 392%, when compared to that of the composite without prestraining.

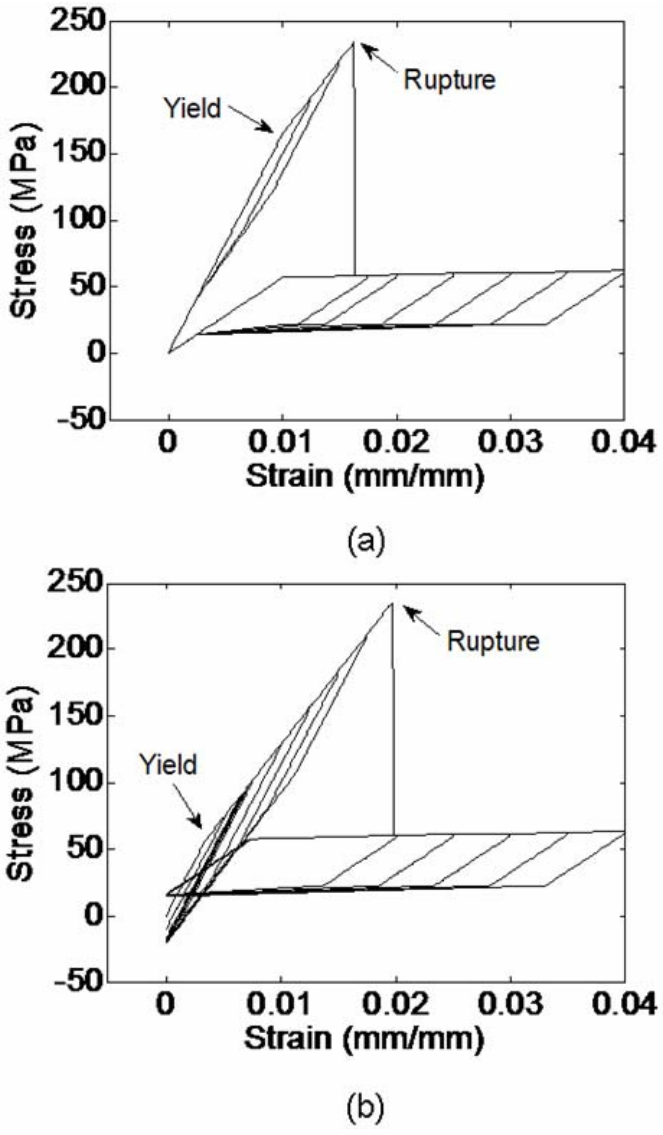

Figure 3.8: Behavior of SMA-FRP composite with (a) 0% prestrain (b) 1% prestrain.

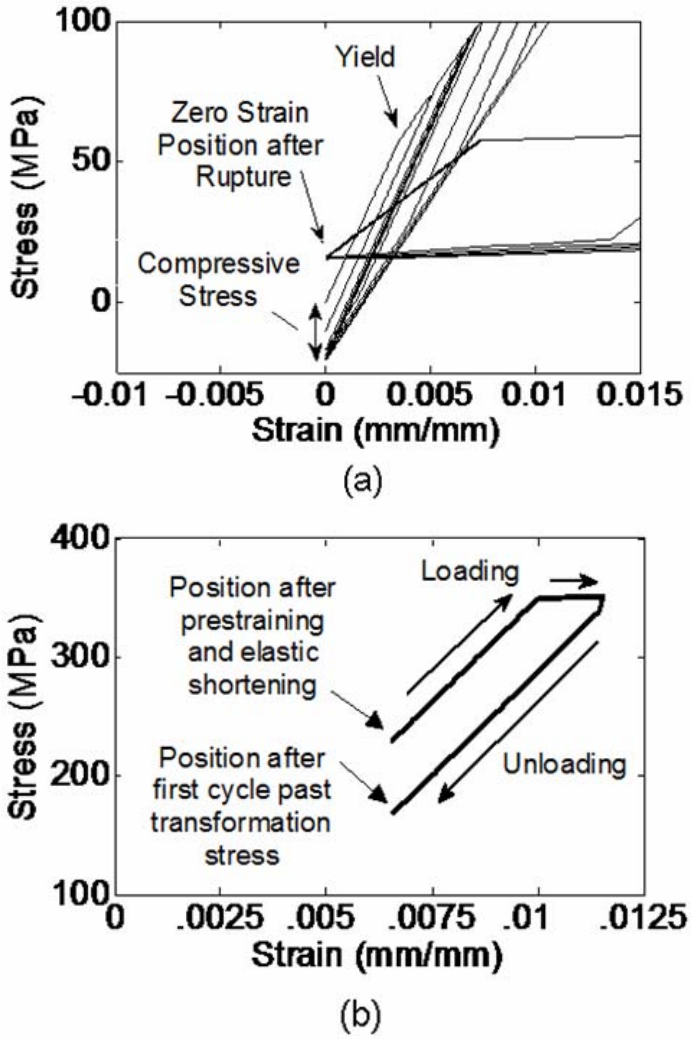

Figure 3.9: (a) Closer view of the stress-strain behavior of the prestrained composite shown in **Figure 3.8**b (b) stress-strain behavior of reinforcing SMA wires during first cycle.

In addition to altering the transformation and rupture strain of the composite, Figure 3.9a (an enlarged view of Figure 3.8b), shows that there are other significant changes to the stress-strain behavior of the composite. After the onset of phase transformation (yield) in the SMAs, but before the rupture of the conventional fibers, it is observed that the unloading of the SMA-FRP results in compressive stress in the composite. This compressive stress results from the SMA being prestrained past the

unloading phase transformation strain. This is demonstrated in Figure 3.9b, which shows the stress-strain behavior of the SMA in the first cycle beyond the SMA transformation strain. After prestraining and elastic shortening, the SMA starts at a stress of about 229 MPa and a strain of 0.0066. After the SMA is loaded past its transformation stress, it unloads to a stress of around 168 MPa and strain of 0.0066. This 61 MPa decrease in stress in the SMA at the composite's unstrained state leads to overall compression in the composite. One can also see that the same mechanism that leads to compressive stress also leads to residual strains, which is defined as strain in the composite when the composite's stress is zero. Additionally, after the rupture of the fiber reinforcement, there is no material to keep the prestraining in the SMA. Consequently, the SMA will want to release its prestrain and return to a state of zero strain, which would be compressive strain in the composite's reference frame; however, in this analysis the displacement based loading prevents the composite reaching compressive strains. Despite the possibility for residual strain or compressive stress in the composite, the significant gains in energy dissipation make prestraining an attractive option.

CHAPTER 4:

PARAMETRIC STUDY WITH SMA-FRP COMPOSITES

The stress-strain behavior of SMA-FRP composites is affected by a number of factors related to the used SMA wires and conventional fiber reinforcement. To determine the effect of these parameters on the stress-strain behavior of the composite, a parametric study was conducted.

4.1 PARAMETERS

Three parameters were considered in this parametric study: 1) amount of SMA reinforcement, 2) level of prestraining in the SMA wires, and 3) type of conventional fiber reinforcement; the values of these parameters are presented in Table 4.1. SMA percentages presented in this table are by volume, and were chosen to provide a range of composites with both fiber and SMA reinforcement, as well as a composite only reinforced with SMA wires. The prestraining levels used in this study were limited to a maximum value of 0.75% in order to avoid prestraining past the SMA transformation strain. The fiber reinforcement types were chosen to provide a range of both modulus of elasticity and rupture strain. Low rupture strain fibers, such as carbon, were not considered since they would typically fail prior to the phase transformation of the SMAs.

In this analysis the values that were held constant were the SMA and matrix properties and the total reinforcement percentage in the composite. The composite's matrix to reinforcement volumetric ratio was 35/65. The resin used in this study was assumed to be epoxy with a modulus of elasticity of 3.0 GPa. The initial modulus of the

SMA wires used in the study was taken as 68.9 GPa, while the phase transformation starts at strain and stress equal to 0.8% and 551 MPa, respectively. These values are typical for the superelastic NiTi SMAs (DesRoches et al. 2004). The loading used in this static analysis is cyclic in tension with the strain demand on the composite increasing by 0.25% each cycle up to a maximum value of 6%.

Table 4.1: Parameters considered in parametric study

Prestrain %	Fiber Reinforcement			SMA % of Reinforcement
0.00	Fiber Type	Tensile Modulus (GPa)	Ultimate Strain (%)	25
0.25	E-Glass	68.9	2.00	50
0.50	S-Glass	86.2	3.00	75
0.75	Aramid	124.1	3.00	100

4.2 RESULTS AND DISCUSSION

The stress-strain relationships from selected composites analyzed in this parametric study are shown in Figure 4.1. In this figure, stress-strain curves for composites reinforced with 75% SMA prestrained to 0.75% are shown for each fiber reinforcement type up until the rupture of the fiber reinforcement. Additionally, in this figure the stress strain curve for the 100% SMA reinforced composite is shown, up to 3% strain; however, it should be noted that since this composite is not susceptible to conventional fiber rupture, the composite retains additional capacity after this point and that 3% strain was chosen only to form a comparison near the strain level of the composites with conventional fibers. As represented in this figure, each of the resulting stress-strain relationships has similar characteristics, including:

- Energy is dissipated by the composite prior to the rupture of the conventional fibers due to the hysteretic behavior of the SMA reinforcement.
- Ductility in the composites is observed due to the stress induced phase transformation of the SMA reinforcement.
- Stiffness degradation beyond the point of SMAs phase transformation is observed in all studied cases. This change in stiffness forms a yield point in the composite's stress-strain behavior, which is more pronounced in some composites and depends on the type of fiber reinforcement and the amount of SMA reinforcement.

Even though the resulting stress-strain relationships shown in Figure 4.1 have some common characteristics, they still vary greatly depending on the composite type. To quantify the differences in the response of the composites, four response parameters are subsequently quantified and compared: 1) energy dissipated elastically (i.e. prior to the rupture of the conventional fibers), 2) composite's transformation stress (i.e. yield stress), 3) strain hardening after the transformation, and 4) residual stress after the rupture of the conventional fiber reinforcement. Parameter 1 provides important information on the damping characteristics of the SMA-FRP composite. Parameters 2 and 3 provide insight on the ductility of the composite, while Parameter 4 is a measure of the composite's performance under the most extreme demands. The results of each of the four response parameters are presented in the following subsections.

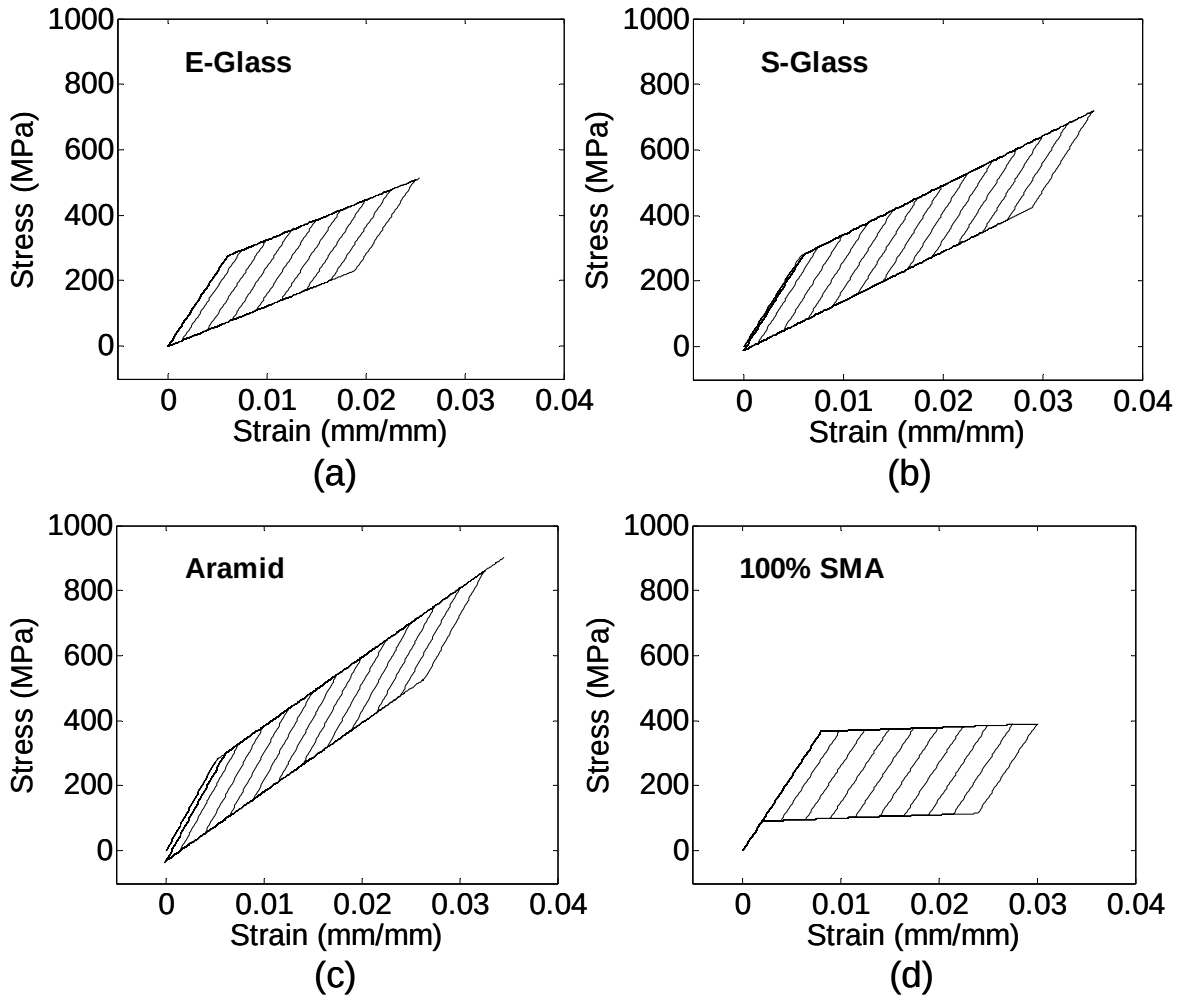

Figure 4.1: Selected stress-strain results from the parametric study of SMA-FRP composites((a),(b),(c)) 75% SMA prestrained to 0.75% (d) 100% SMA reinforced

4.2.1 Energy Dissipation

One of the main benefits of SMA-FRP composites is their ability to dissipate energy without permanent damage. Therefore, the potential for energy dissipation before the rupture of conventional fibers was quantified by calculating the area contained within the stress-strain hysteresis in the cycles before the rupture. Figure 4.2 shows a comparison of the ability of the studied composites to elastically dissipate energy. The figure illustrates that the amount of energy dissipated increases as both the amount of

SMA reinforcement and the prestrain of the SMA increases. Since SMA fibers were the only type of reinforcement used in the composite with 100% SMA, there was no need to prestrain the fibers. Also, for this composite type the energy dissipation was calculated up until the specimen reached the rupture strain of the conventional fiber reinforcement of the group it was being compared with. The results presented in the figure show that the energy dissipated by the composite with S-Glass reinforcement and no prestrain increased by 200% when the SMA reinforcement increases from 25% to 75% and the energy dissipated by 25% S-Glass/75% SMA composite increased by 70% when the prestraining was increased from 0% to 0.75%. Even though prestraining of composites containing 25% SMA increased the energy dissipation by 18% to 40%, depending on the conventional fiber and the amount of prestrain, the total amount of energy dissipated was still very low; therefore, the use of prestraining to increase energy dissipation should be reserved for composites with moderate to high SMA content. When comparing between conventional fiber reinforcements, S-Glass and aramid have comparable energy dissipation performance, with an on average difference of less than 2.5% given the same SMA and prestrain percentage. On the other hand, the composites reinforced with either S-Glass or aramid fibers dissipated on average about 180% more energy than composites reinforced with E-Glass containing the same amount of SMA with the same level of prestrain. This result is primarily due to the higher rupture strain of both S-Glass and aramid fibers compared to E-Glass fibers. Hence, a slight increase in the rupture strain of the conventional fibers will result in a significant improvement in the damping capability of the composite. It can also be seen that the energy dissipation capacity of composites

reinforced with 75% SMA and highly prestrained 50% SMA reinforcement were similar to the capacity of the 100% SMA reinforced model.

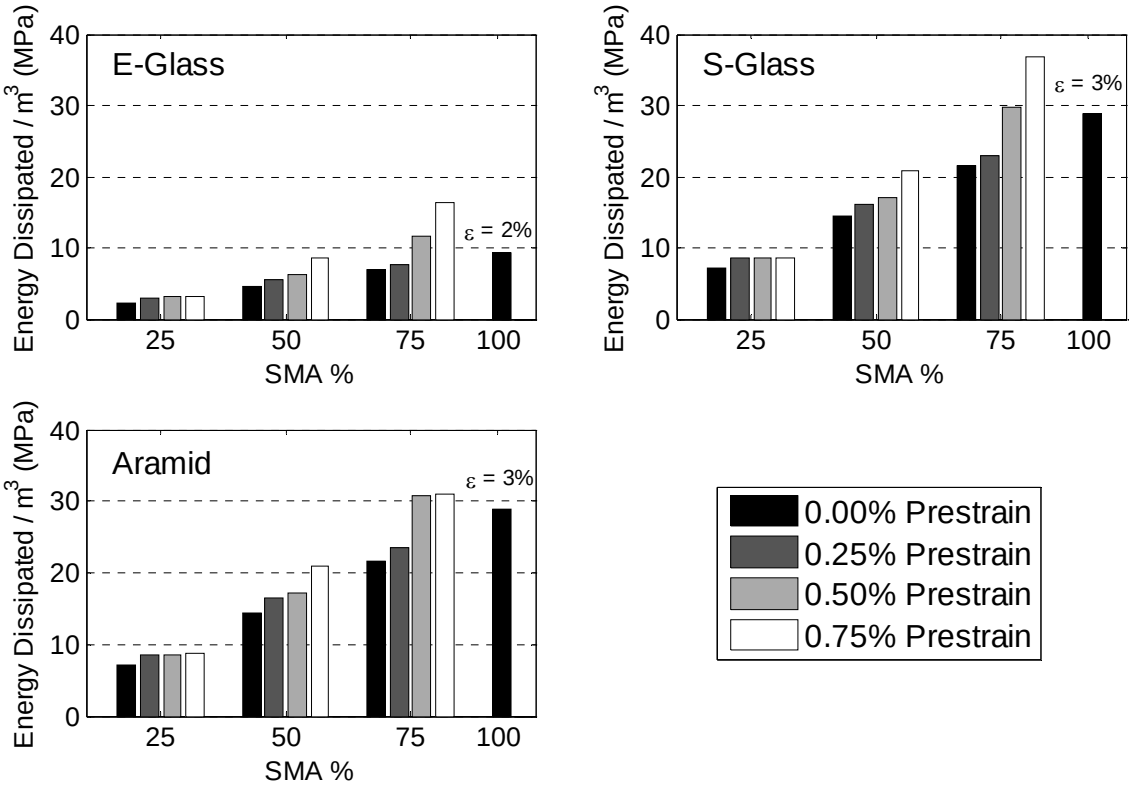

Figure 4.2: Parametric Study Results – Elastic Energy Dissipation.

4.2.2 Transformation "Yield" Stress

The transformation stress, which represents the yielding point of the composite, is considered important since it is preferable for the composite to remain linear elastic when subjected to service loads, but also yield early enough before failure. A good measure for acceptable transformation strengths is that of steel rebar, which is commonly available with yield stresses between 280 and 520 MPa. Figure 4.3 compares the yield strength of the composites in this parametric study, which vary between 109 and 582 MPa. From

this figure one can see that increasing the prestraining decreases the yield strength. Additionally, at high prestrain levels, increasing the SMA reinforcement percentage increases the yield stress and, conversely, at low prestrain levels, increasing the SMA reinforcement percentage lowers the yield stress.

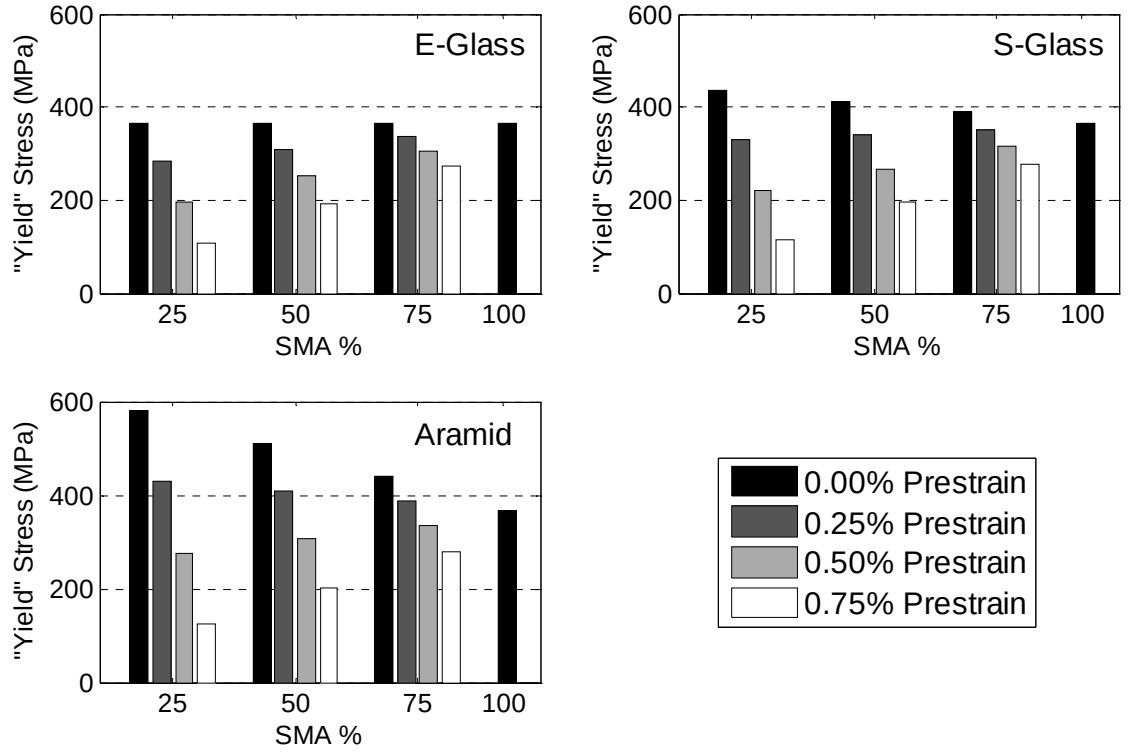

Figure 4.3: Parametric Study Results – Yield Stress.

By comparing Figure 4.2 and Figure 4.3 it can be concluded that some of the composites which had the best performance in terms of energy dissipation, had transformation stresses low enough for them to be unsuitable for the intended application. An example of this is the composite with 50% S-Glass and 50% SMA prestrained to 0.75% reinforcement. This composite has one of the highest elastic energy dissipation

potentials of all the 50% SMA reinforced composites, but has a transformation stress of 195 MPa, too low for many applications. On the other hand, some composites demonstrated good performance in both energy dissipation and yield stress. For example the composite reinforced with 25% S-Glass and 75% SMA prestrained to 0.75% dissipated the second most amount of energy while maintaining an acceptable yield stress of 315 MPa. These results indicate that optimization is essential to determine the composite that best matches the needs of a particular application

4.2.3 Strain Hardening Ratio

In the case of steel rebars, after steel yields it has a low stiffness, near plastic response, which allows it to endure further strain demand without developing excessive additional stress. This response is what is referred to as a ductile response. So far, the phase transformation of the SMAs has been compared to the yield point of steel, but the response of a SMA-FRP after this transformation point is not the same; there is a reduction in stiffness after this point, but in most cases the composite is still stiff enough that the response cannot be described as plastic. The strain hardening, which is defined as the ratio of post transformation stiffness to initial stiffness can be used, in part, to determine if the response of the composite is ductile. Figure 4.4 shows this ratio for the analyses in the parametric study. As one can see from this figure, the ratio observed in the composites varies from 2.31% to 84.6% and is unaffected by the amount of SMA prestrain. As one may expect, the ratio is lowered when the SMA percentage is increased. Additionally, for the same level of SMA reinforcement, the modulus ratio increases when stiffer conventional fiber reinforcement is used. For example, with 75%

SMA reinforcement the ratio is 26.7%, 31.0%, and 38.7% with E-Glass, S-Glass, and aramid reinforcement, respectively.

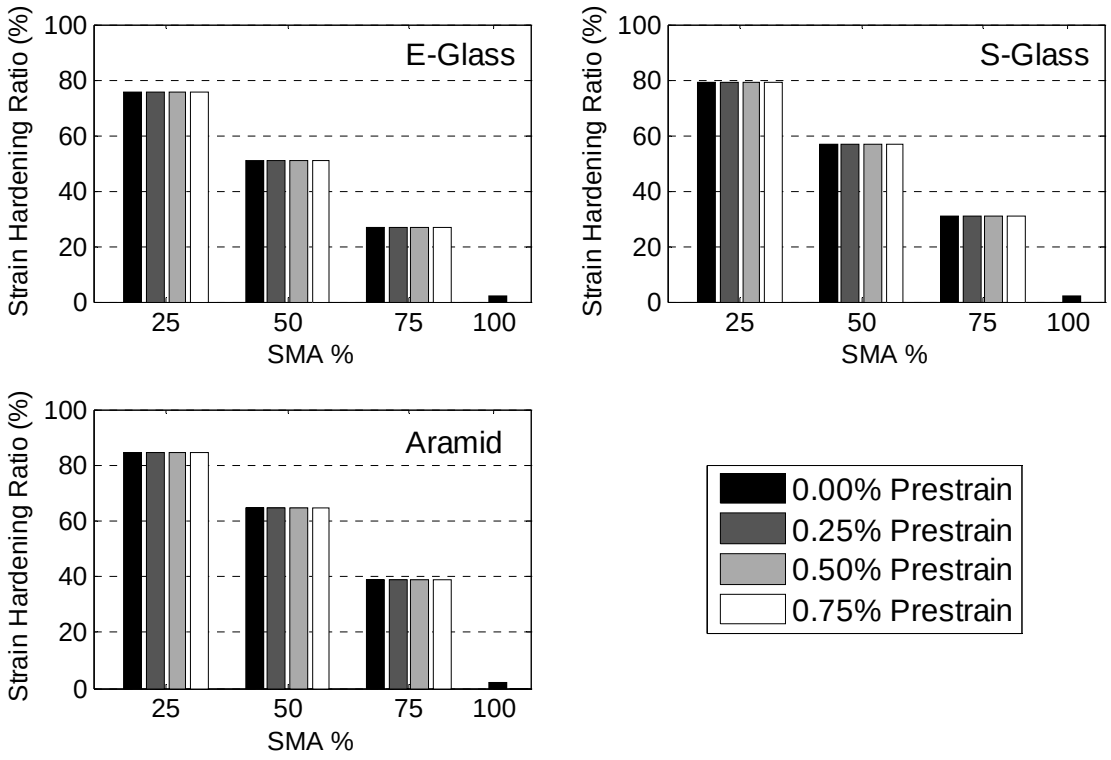

Figure 4.4: Parametric Study Results – Strain Hardening Ratio.

4.2.4 Residual Stress

Another important characteristic of SMA-FRP composites is their ability to maintain a reasonable percentage of their load-carrying capacity after the conventional fibers are completely ruptured. This characteristic is crucial, especially under extreme loading conditions where such residual stress could play a significant role in protecting the structure from collapsing. Figure 4.5 shows a comparison of the residual stress (as a percentage of the rupture stress) of the studied composites. Because no conventional

fibers are present in the 100% SMA reinforced composite, it is excluded from this comparison. A wide range of residual stress values (4.6% to 52.3%) was observed in the study. The residual stress increases with higher SMA percentage. When comparing between the residual stresses corresponding to different fiber reinforcement types, one can see that the E-Glass has the best performance with residual stresses between 11.5% and 52.3% of the rupture stress. This is due to the relatively low rupture strain and modulus of elasticity of E-Glass, which serves to limit the rupture stress. When comparing composites with S-Glass and aramid fiber, which are modeled with the same rupture strain, it is noticed that the S-Glass composite outperforms the aramid composite in residual stress. This highlights one potential disadvantages of using high modulus fiber reinforcement in SMA-FRP composites.

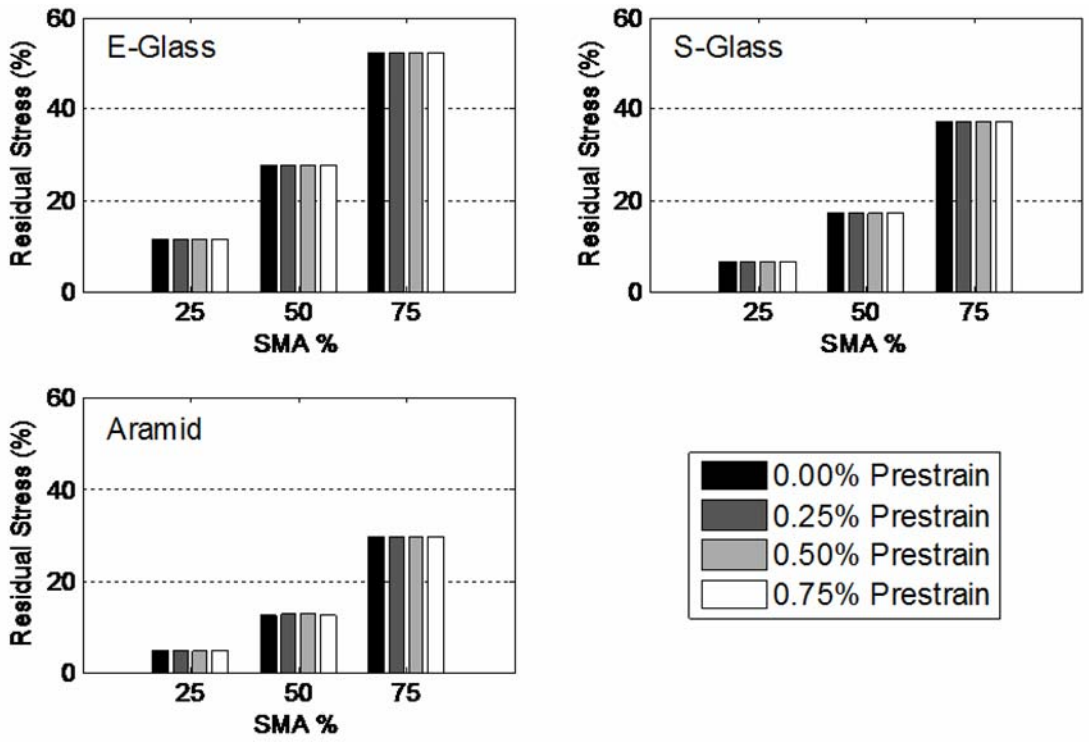

Figure 4.5: Parametric Study Results – Residual Stress.

CHAPTER 5:

MOMENT CURVATURE ANALYSIS

In this chapter the performance of SMA-FRP bars in concrete structures is evaluated at the section level with moment curvature analyses. These moment curvature analyses allow comparisons to be made between concrete sections reinforced with conventional FRPs and SMA-FRPs with various reinforcement ratios and confinement levels. In preparation for these analyses the analytical model used in the study is presented along with the material models used.

5.1 ANALYTICAL MODEL

To adequately compare the structural behavior of FRP and SMA-FPR reinforced concrete structures, a basis of comparison was formed through the use of moment-curvature relationships. To create these moment-curvature relationships, a fiber section analysis was performed using the finite element software OpenSees [Mazzoni et al. 2009], which was specifically designed for structural and geotechnical simulation under earthquake excitations. The concrete section used for this moment-curvature study is depicted in Figure 5.1. The analytical model representing this section has 240 fibers in the axis of bending. The reinforcement in this section is assumed to be in a single row at the top and bottom of the section, regardless of reinforcement ratio. Equal top and bottom reinforcement was chosen to equip the section for load reversal in seismic loading. The material models for the reinforcement and concrete fibers used in this analysis are subsequently discussed.

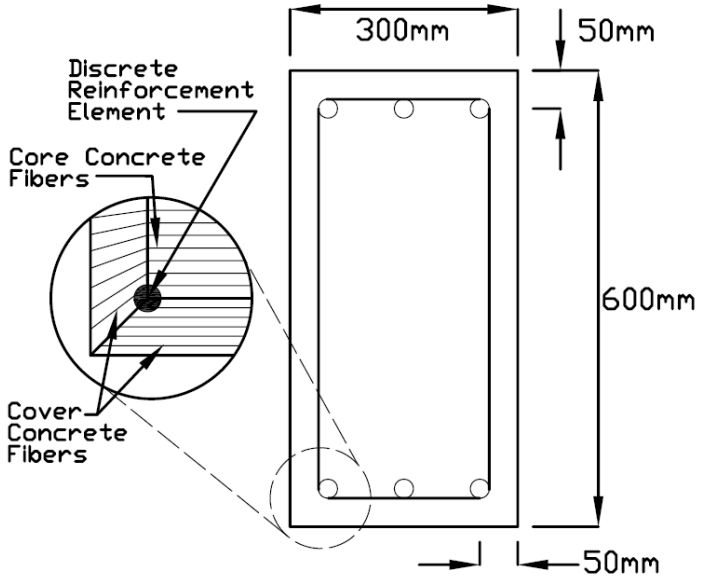

Figure 5.1: Reinforced concrete section used in the analysis

5.2 MATERIAL MODELS

This section presents the material models developed to describe the stress-strain constitutive behaviors of the SMA-FRP reinforcement, the FRP reinforcement and the concrete that were used in the study. These models were used throughout the entire of the thesis except when otherwise noted.

5.2.1 SMA-FRP Reinforcement

In Chapter 3 experimental tests on SMA-FPR composite coupons were discussed. From these experimental results, a phenomenological model for the behavior of SMA-FRP composites was developed in MATLAB. However, the analytical tool used for this moment curvature analysis, and the case studies presented in subsequent chapters, is OpenSees; therefore a new model was needed. This model was created in OpenSees by

combining, in parallel, material models for the resin (epoxy), conventional fiber reinforcement, and SMA wires. The material models used for both epoxy and conventional fibers were linear elastic. For the SMA wires, the OpenSees' built–in SMA model was utilized with the experimentally acquired SMA properties considering training of the SMA fibers. A comparison of the model and the experimental data presented in Chapter 3 is shown in Figure 5.2. This comparison is shown up to the rupture of the conventional fibers in the composite, which is defined to be the failure point due to the substation reduction in capacity after this point. As one can see from this figure, the analytical model was able to predict closely the experimentally behavior.

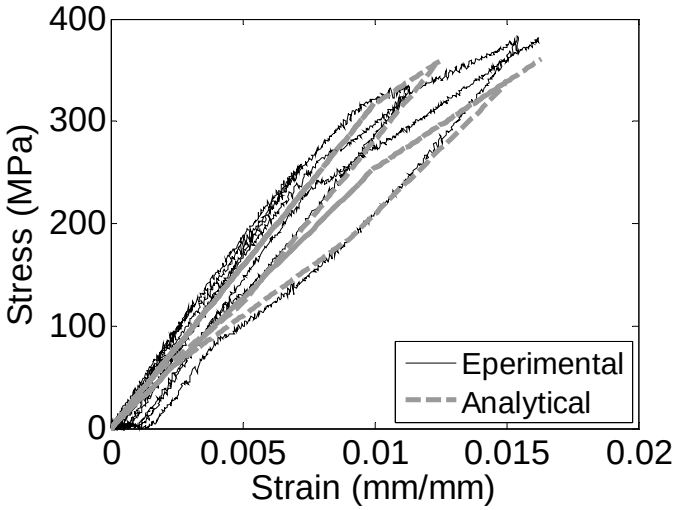

Figure 5.2: Experiment and analytical comparison of SMA-FRP stress-strain behavior

The developed analytical model was utilized to describe the behavior of two types of SMA-FRP composites, which were used during the rest of the study. The first SMA-FRP composite (SMA-FRP1) is reinforced, by volume, with 25% S-Glass and 75% SMA, while the second SMA-FRP composite (SMA-FRP2) is reinforced with 100% SMA. The volumetric ratio of reinforcement to resin for both composites was 65/35.

The SMA model used to develop these SMA-FRP composites is shown in Figure 5.4. The initial modulus was taken as 68.9 GPa, the transformation starts at strain and stress equal to 0.8% and 551 MPa, respectively. These values are typical for the superelastic NiTi [DesRoches et al. 2004]. The S-Glass fibers have a modulus of elasticity of 86.2 GPa, within the normal range for commercially available S-glass, and a rupture strain of 3%, while the epoxy matrix has a modulus of elasticity of 3.0 GPa. S-Glass was chosen as the conventional fiber reinforcement in SMA-FRP1, because of its high rupture strain. The stress-strain behaviors of the SMA-FRP1 and SMA-FRP2 are shown in Figure 5.3. In this figure the behavior SMA-FRP1 is only shown before rupture of the conventional fibers. This figure shows that, as one might expect, SMA-FRP2 has superior performance in terms of both ductility and energy dissipation through hysteretic area.

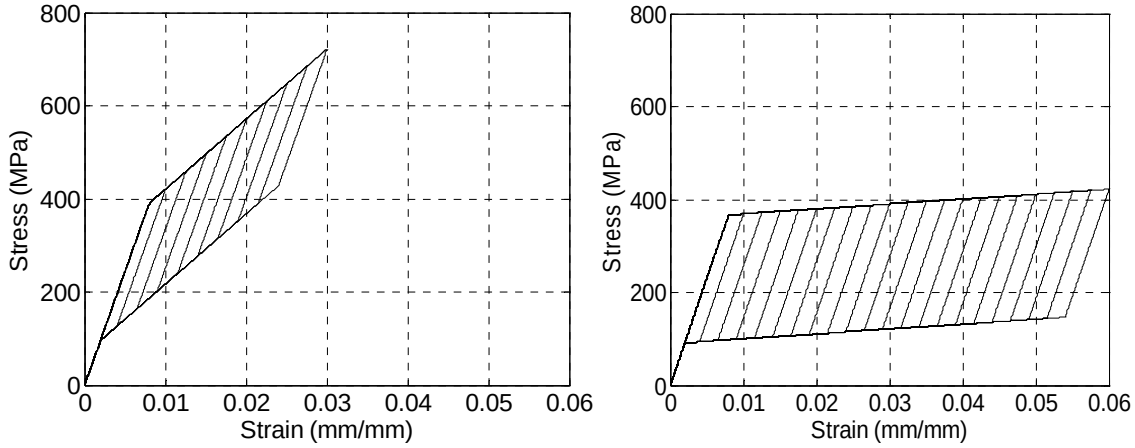

(a) SMA-FRP1 (b) SMA-FRP2

Figure 5.3: Stress-strain behaviors of the SMA-FRP composites investigated in this study

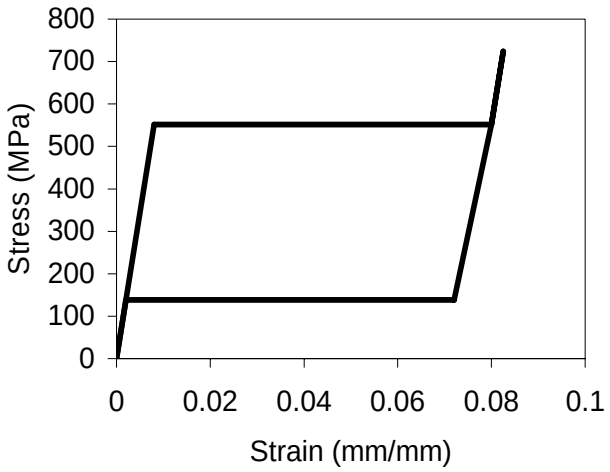

Figure 5.4: SMA stress-strain model used in analyses

5.2.2 FRP Reinforcement

The FRP reinforcing bars used in the analysis are a composite of an epoxy matrix reinforced with E-Glass fibers. The composite's volumetric reinforcement ratio is 65/35. The composite bars were modeled as linear elastic until rupture with a modulus of elasticity of 45.9 GPa and an ultimate strain of 2%. These mechanical properties were chosen as they are similar to the properties of currently manufactured GFRP bars [Bank (2006)].

5.2.3. Concrete

The concrete sections used in this analysis are composed of two different regions of concrete; cover concrete and core concrete. The cover concrete was unconfined and thus was defined to be ineffective due to spalling once a relatively low compressive strain (in this study 0.003) has been reached. As this analysis was focused on improving the ductility and energy dissipation in FRP reinforced concrete structures, the core concrete

was modeled as being confined with FRP stirrups. Due to the limited work done on the analytical characterization of concrete confined with FRP stirrups, confinement models designed for FRP wrapped rectangular concrete sections were sought in this study. The model by Youssef et al. (2007) was adopted due to its experimental verification with a group of specimens that were confined by a large range of FRP wraps; the volumetric ratio of the FPR wraps varied from 1.2% to 6.1% and both E-glass and carbon fiber wrapped specimens were tested.

The Youssef et al. model uses four parameters to define two key points, the transition point, which is the point at which the FRP becomes fully activated due to the dilation of the concrete, and the ultimate point, i.e. the point at which the confined section fails due to rupture of the FRP. These points can be seen on the schematic presented in Figure 5.5a for the confined concrete stress-strain curve. The four parameters used to define these points are the confined concrete ultimate stress, $f_{cu}^{'}$; the confined ultimate strain, ε_{cu}; the stress at the transition point, f_t; and the strain at the transition point, ε_t. To calculate these parameters the Equations 5.1 – 5.4 are used.

$$f_{cu}^{'} = \left(0.5 + 1.225 \left(\frac{f_{lu}^{'}}{f_c^{'}} \right)^{\frac{3}{5}} \right) f_c^{'} \tag{5.1}$$

$$\varepsilon_{cu} = 0.004325 + 0.2625 \left(\frac{f_{lu}^{'}}{f_c^{'}} \right) \left(\frac{f_u}{E} \right)^{\frac{1}{2}} \tag{5.2}$$

$$f_t = \left(1.0 + 1.1350 \left(\frac{\varepsilon_{jt} \rho E}{f_c^{'}} \right)^{\frac{5}{4}} \right) f_c^{'} \tag{5.3}$$

$$\varepsilon_t = 0.002 + 0.0775\left(\frac{\varepsilon_{jt}\rho E}{f_c^{'}}\right)^{\frac{6}{7}}\left(\frac{f_u}{E}\right)^{\frac{1}{2}} \tag{5.4}$$

In these equations $f_c^{'}$ is the unconfined concrete compressive strength, E is the FRP modulus of elasticity, f_u is the FRP ultimate stress, ρ is the reinforcement ratio for the FRP, and $f_{lu}^{'}$ is the effective confinement pressure. Additionally, ε_{jt} is the strain in the lateral reinforcement at the transition point, which was taken to be 0.002, as recommended by Youssef et al. and Toutanji (1999). $f_{lu}^{'}$ is calculated with equations 5.5 – 5.7.

$$f_{lu} = \frac{1}{2}\rho f_u \tag{5.5}$$

$$f_{lu}^{'} = k_e f_{lu} \tag{5.6}$$

$$k_e = \frac{1 - \left[\frac{(b-r_c)^2 + (h-r_c)^2}{3hb}\right] - \rho_l}{1-\rho_l} \approx 1 - \left[\frac{(b-r_c)^2 + (h-r_c)^2}{3hb}\right] \tag{5.7}$$

Where k_e is the shape modification factor, b is the confined section width, h is the confined section height, r_c is the rounded corner radius, and ρ_l is the longitudinal reinforcement ratio. In this situation, where the core is being confined with stirrups not a jacket, r_c can be estimated by using the minimum bend radius for FRP bars outlined in ACI 440 [ACI (2006)]. In the proceeding analysis, the longitudinal reinforcement ratio will vary; therefore, it is convenient to neglect ρ_l in Equation 5.7, so that a constant k_e can be approximated with only the confined core dimensions. One important difference between confinement with FRP wraps and stirrups is the fact that in the longitudinal

direction, wraps are continuous while stirrups are discrete. The adopted model does not consider the effect of vertical spacing between the stirrups, which will reduce the effective confinement by introducing areas of ineffectively confined concrete in between stirrups [Pantelides et al. (2004)]. To address this deficiency the confining stress is altered by a vertical confinement effectiveness coefficient, k_l. Several researchers, [Paultre and Legeron (2008) and Mander et al. (1988)] used the following expression when considering the vertical spacing of confinement in concrete rectangular columns

$$k_l = \left(1 - \frac{s}{2h}\right)\left(1 - \frac{s}{2b}\right) \tag{5.8}$$

In this expression, *s* is the spacing between the stirrups. Considering now the effect of the spacing of the FRP stirrups, $f_{lu}^{'}$ can now be calculated as:

$$f_{lu}^{'} = k_e k_l f_{lu} \tag{5.9}$$

Using this model, confined concrete models were developed for three levels of confinement, low, medium, and high, which were designed to correspond to ultimate concrete strains of 0.005, 0.0075, and 0.01, respectively. The stress strain curves for these confined concrete models and cover concrete can be found in Figure 5.5b. The reinforcement ratios and stirrup spacing for these models are found in Table 5.1. The range of confinement provided by these models will enable conclusions from the analysis to be made on the correlation between performance of SMA-FRP reinforcement and the concrete confinement. The confined concrete models were incorporated into the analysis through the OpenSees material model, Concrete02.

Table 5.1: Reinforcement ratios and stirrup spacing used for confinement models

Confinement	Stirrup Spacing (mm)	Reinforcement Ratio*
High	80	0.039
Medium	120	0.026
Low	250	0.012

* Based on concrete core dimensions

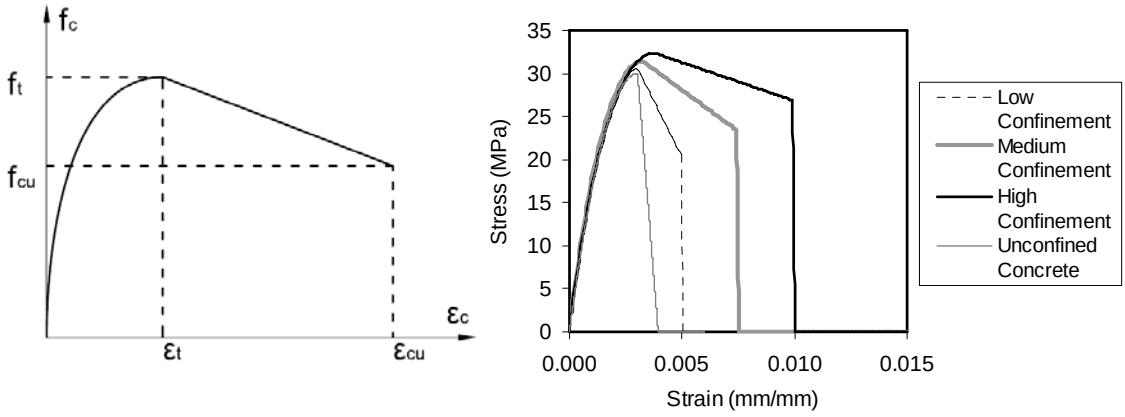

(a) (b)

Figure 5.5: (a) Generalized confined stress-strain curve
(b) Stress-strain curves for three levels of confinement calculated using confinement model modified from Youssef et al. 2007

5.3. MOMENT CURVATUVE COMPARISON

Using the developed analytical models, moment curvature analyses were performed at reinforcement ratios ranging from 0.5% to 3.0% (using reinforcement on one side of the section). By post-processing the data generated by these analyses one can find the effect of the reinforcement ratio and confinement on the moment capacity of the section (see Figure 5.1). In this thesis, the moment capacity is defined as the maximum moment achieved before either failure or significant decrease in moment capacity is observed. For the FRP and SMA-FRP1 reinforced sections the limit states that defined

failure were the rupture of the conventional fibers in the reinforcing bars (under-reinforced section), or the crushing of the core concrete (over-reinforced section); for the SMA-FRP2 composite reinforced sections the only structural limit state that defined failure was the crushing of the core concrete due to the high strain capacity of SMAs.

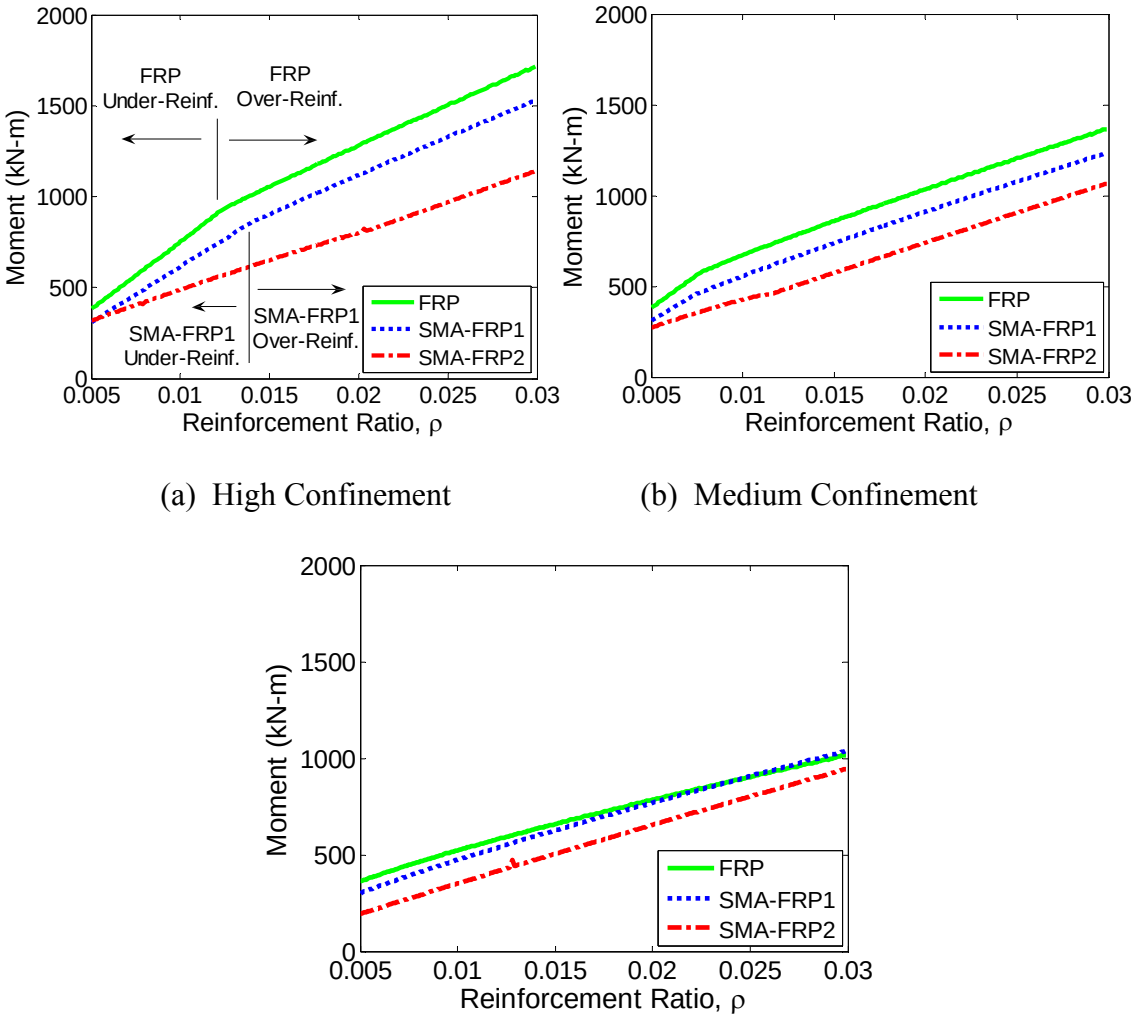

(a) High Confinement

(b) Medium Confinement

(c) Low Confinement

Figure 5.6: Moment Capacity vs. reinforcement ratio for FRP and SMA-FRP reinforced sections

Given these limit states, one can see from Figure 5.6 that the moment capacity of the section is increased when the confinement level or the reinforcement ratio is

increased regardless of the reinforcement type. It is also seen that the moment capacity of the sections with different reinforcement types becomes similar as the confinement is lowered. This can be attributed to the fact that low confinement results in crushing of concrete before the reinforcement can fully engage. Additionally in this figure one can see kinks, i.e. points where a change in the slope occurs. These kinks are observed in the FRP and SMA-FRP1 cases at points where the failure mode of the section changes from under-reinforced to over-reinforced. An example of this is seen for the highly confined FRP reinforced section at a reinforcement ratio of 1.24%.

The effect of the reinforcement ratio and confinement on the curvature ductility of the section is also presented in Figure 5.7. The curvature ductility is defined as the maximum curvature achieved before the failure of the section divided by the curvature that corresponds to the onset of phase transformation of the SMA in the composite (yielding). For the FRP reinforced sections no transformation occurs in the reinforcement, so, by definition, the curvature ductility of the FRP reinforced sections is always unity. Depending on the confinement level and reinforcement ratio, the curvature ductility of SMA-FRP reinforced sections was observed as high as 4.2 and 11.5 for SMA-FRP1 and SMA-FRP2, respectively. In contrast, FRP reinforced section always exhibit a non-ductile response. For the SMA-FRP reinforced sections, increasing the reinforcement ratio, or decreasing the confinement level has the effect of lowering the curvature ductility of the section. One kink that was not seen in the maximum moment comparison can be seen in the SMA-FRP2 case with medium confinement at a reinforcement ratio of 0.01. This kink is due to the transition from crushing of the core concrete before and after SMA strain hardening, which occurs at 8% strain in the SMA.

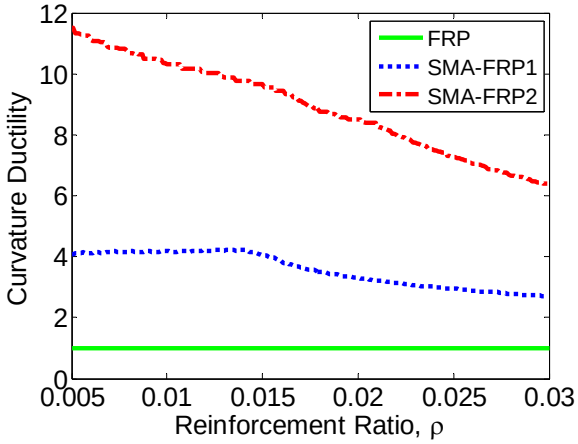

(a) High Confinement

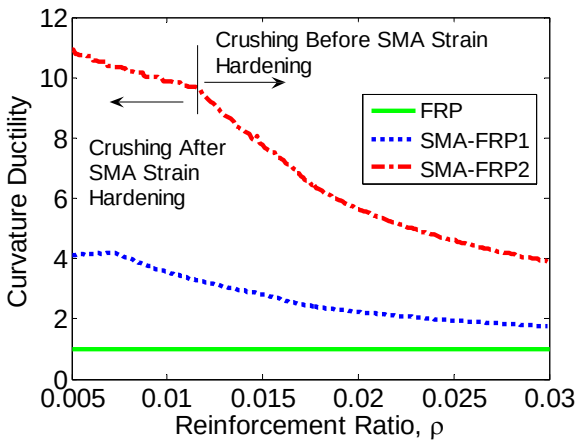

(b) Medium Confinement

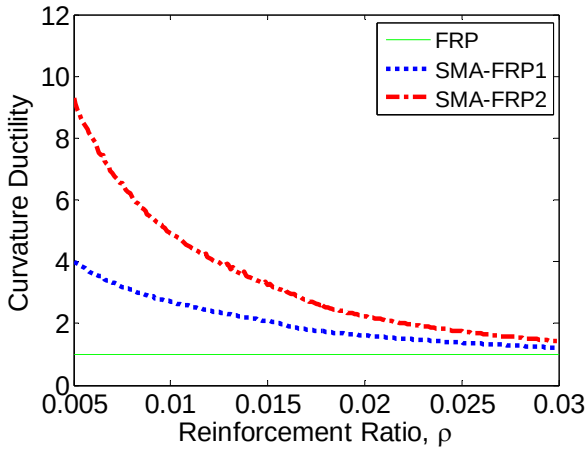

(c) Low Confinement

Figure 5.7: Curvature ductility vs. reinforcement ratio for FRP and SMA-FRP reinforced sections

Using the maximum moment versus reinforcement ratio comparison (see Figure 5.6) one can determine the necessary reinforcement ratios to generate equivalent sections based on a maximum moment capacity basis of comparison. An example with this basis of comparison is shown in Figure 5.8 for a moment capacity of 600 kN-m where the ultimate point, as defined above, is shown by a black dot. In this figure the moment-curvature relationship that results in the desired moment capacity is shown for each

reinforcement type considered at all three levels of confinement. As discussed before, these moment curvature relationships show that reinforcement with SMA-FRP is capable of adding significant curvature ductility to the section. Additionally, this figure shows that by decreasing the confinement of the section any potential curvature ductility gained from the usage of SMA-FRP reinforcement is greatly diminished.

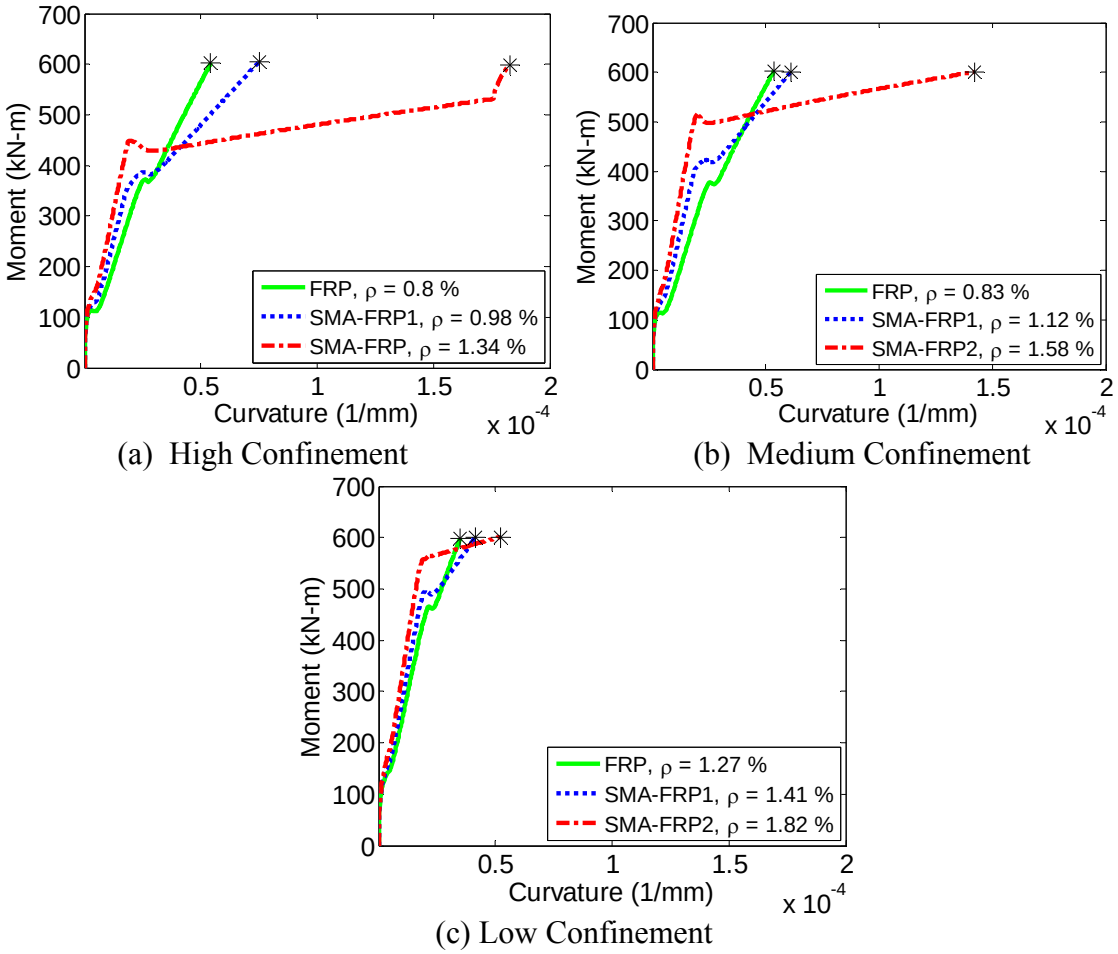

Figure 5.8: Moment-curvature comparison based on a moment capacity of 600 kN-m.

CHAPTER 6:

NUMERICAL CASE STUDIES

The performance of SMA-FRP composite reinforcement was further investigated on the structural element level with two numerical case studies using OpenSees. The first case study was on a concrete cantilever beam. This study was limited in scope and compared the performance of beams using FRP or SMA-FRP reinforcement in the plastic hinge region of a beam designed for a particular moment capacity. The second case study involved a 2-dimensional (2-D) concrete beam-column joint reinforced in beam plastic hinge zone with FRP or SMA-FRP reinforcement. This case study was more extensive and was used to compare the performance of the SMA-FRP reinforcement at various levels of concrete confinement and moment capacity of the members. Both these case studies are used to show how SMA-FRP bars can be used to add ductility and enhance the energy dissipation capacity of concrete structures primarily reinforced with conventional non-ductile linear elastic FRP bars.

6.1 CASE STUDY ONE: CANTILEVER BEAM

This case study investigated the cyclic behavior of an overall FRP reinforced concrete cantilever beam with two types of reinforcement in the plastic hinge zone at the end of the beam, conventional GFRP bars and SMA-FRP bars. The geometry of the beam and section as well as the cantilever tip displacement pattern is shown in Figure 5.1. Two different SMA-FPR composites were investigated in this study:

- SMA-FRP1: SMA-FRP composite reinforced with 25% S-Glass and 75% unprestrained SMA wires
- SMA-FRP2: SMA-FRP composite reinforced with 100% SMA

The stress-strain behavior of these composites, as well as the material properties of the FRP bars used in this analysis, can be found in Chapter 5 (see Figure 5.3). Additionally, using the model described in Chapter 5, a confined concrete model for this analysis was developed based on an ultimate concrete strain of 0.009. The stress strain curves for the confined concrete and cover concrete models can be found in Figure 6.2.

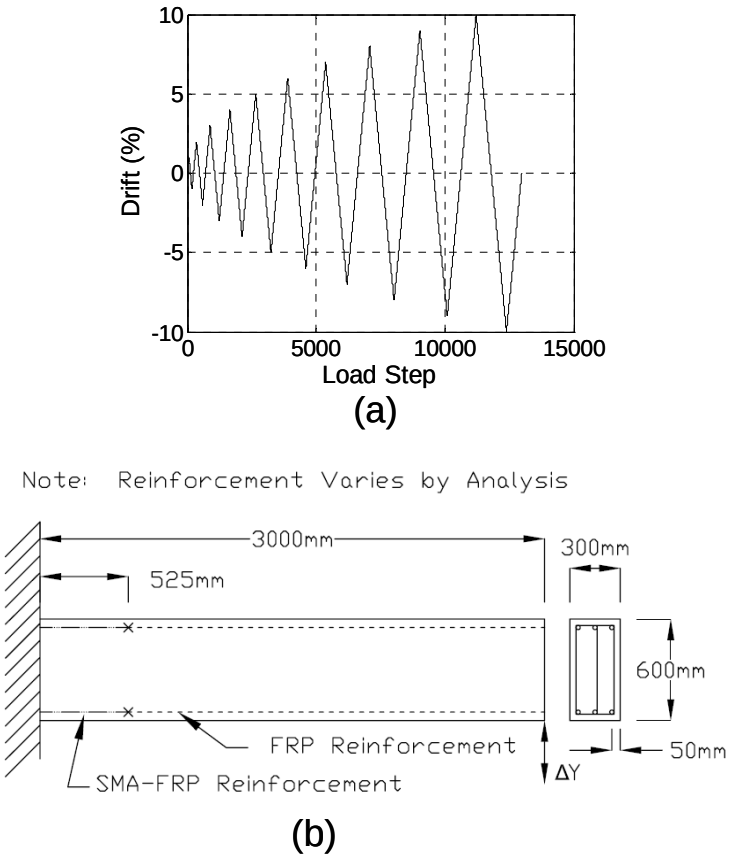

Figure 6.1: (a) Geometry of the cantilever beam (b) tip displacement pattern used in the case study.

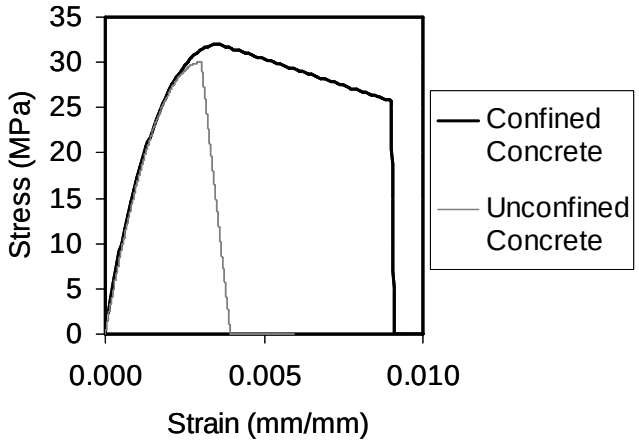

Figure 6.2: Stress-strain curves for concrete models

To provide an accurate basis of comparison, a moment curvature analysis was completed to determine the reinforcement ratios necessary for equal moment capacity of the section when reinforced with either SMA-FRP or FRP. Based on an FRP reinforcement ratio of 1%, the resulting reinforcement ratios for SMA-FRP1 and SMA-FRP 2 were 1.23% and 1.91%, respectively. This moment curvature comparison is shown in Figure 6.3. In these moment curvature relationships the FRP reinforced section fails due to tensile rupture of the composite, the SMA-FRP1 reinforced section reaches its maximum moment right before it fails due to the rupture of the epoxy and fiberglass, and SMA-FRP2 fails from crushing of the core concrete.

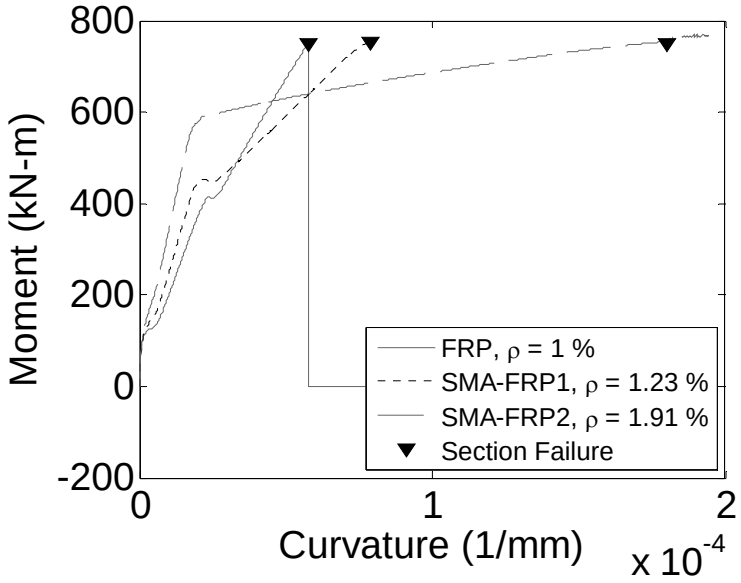

Figure 6.3: Moment-curvature relationships of SMA-FRP and FRP reinforced sections with the same moment capacity.

Figure 6.4 shows the load vs. drift at the tip of the cantilever beam for each reinforcement type until the failure of the cantilever is reached. This corresponds to the rupture of the reinforcing fibers in the FRP (Figure 6.4a) and SMA-FRP1 reinforced sections (Figure 6.4b) and the crushing of the core concrete for the SMA-FRP2 reinforced section (Figure 6.4c). From Figure 6.4 one can see that the sections reinforced with SMA-FRP1 and SMA-FRP2 dissipate significantly more energy than the FRP reinforced section and exhibit ductile behavior. These figures also show that there is not significant visible degradation in the hysteresis due to the concrete deterioration. To explain this phenomenon the behavior of the materials is examined. Figure 6.5 shows the stress-strain relationship for the core concrete and SMA-FRP reinforcement at the top of the SMA-FRP2 reinforced specimen and the first integration point of the member. In this figure points are noted on the curves when specific drift levels in the member are reached. As one can see from this figure the confined core concrete does degrade at

relatively high levels of compressive stain; however, as the concrete degrades more stresses move to the reinforcement in compression, this stress balance is responsible for the lack of major degradation in the load-deformation hysteresis seen in Figure 6.4.

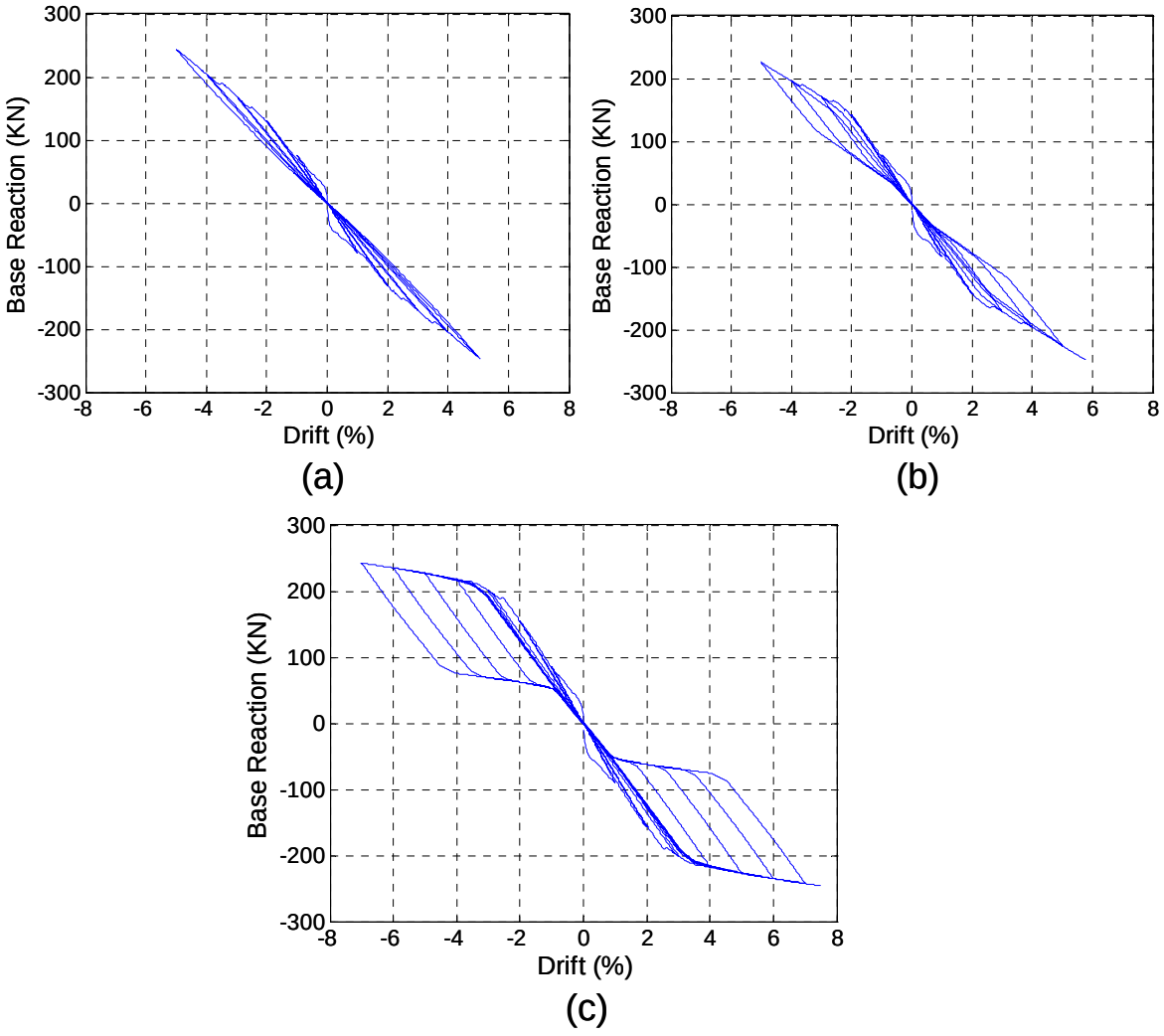

Figure 6.4: Reaction vs. drift at the tip of the concrete cantilever beam when reinforced with (a) FRP (b) SMA-FRP1 (c) SMA-FRP2

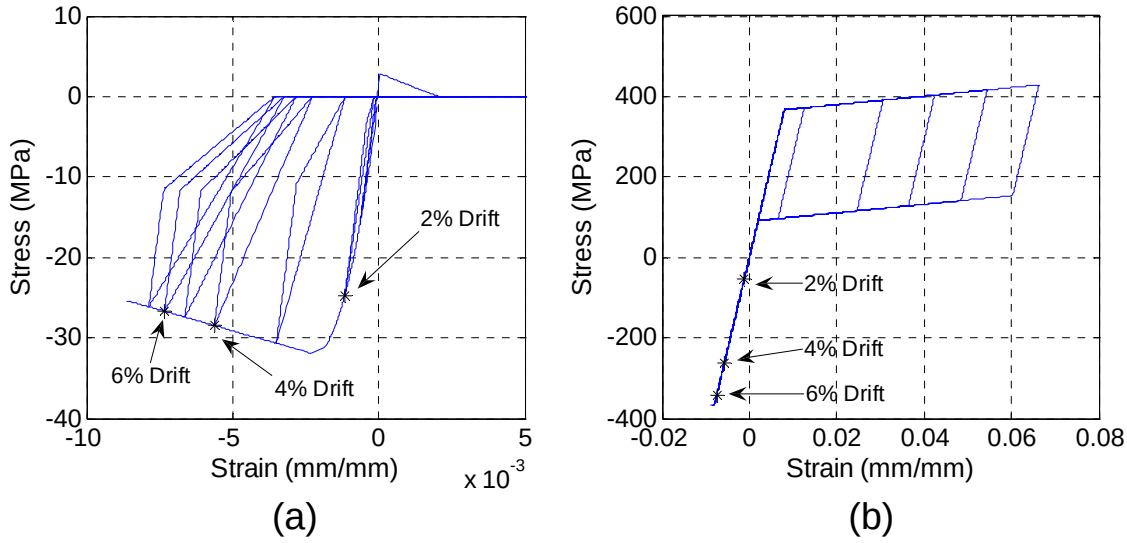

Figure 6.5: Stress vs. strain in the (a) Core concrete (b) SMA-FRP reinforcement at the top of the SMA-FRP 2 reinforced section

To evaluate the performance of the SMA-FRP reinforcement, two quantities are calculated and compared: ductility and damping. The displacement ductility of the SMA-FRP reinforced members can be calculated by dividing the displacement corresponding to the transformation of the SMA in the reinforcement to the ultimate displacement. The displacement ductility of the beam reinforced with SMA-FRP1 and SMA-FRP2 was 2.83 and 2.65, respectively, while for the conventional FRP reinforced beam the behavior was almost linear, i.e. non-ductile.

The damping provided by a structure is an important parameter because it is linked to the energy dissipated by the structure. With the data from the last completed cycle of each specimen before failure, the viscous damping of an equivalent linear system, ζ_{eq}, was calculated for each model using equation 6.1 (Chopra 1995).

$$\zeta_{eq} = \frac{1}{4\pi}\left(\frac{E_{Dis}}{E_{Elastic}}\right) \tag{6.1}$$

In this equation E_{Dis} is the hysteretic energy dissipated in the last complete cycle and $E_{Elastic}$ is the equivalent linear elastic energy stored in the system at the cycle's maximum drift. The damping ratio due to the hysteretric area was calculated to be 0.006, 0.018, and 0.048 for the FRP, SMA-FRP1, and SMA-FRP2 reinforced sections, respectively.

6.2 CASE STUDY TWO: BEAM-COLUMN JOINT

In this case study a 2-dimensional (2-D) concrete beam-column joint reinforced in the plastic hinge zone in the beam with SMA-FRP and FRP reinforcements is investigated under cyclic loading. While this case study focuses on using SMA-FRP composite reinforcement in frame structures, it is important to note that the reinforcing of beam-column joint was selected as an example among other potential applications of SMA-FRP reinforcement in concrete structures with high level of ductility demand.

The physical and finite element representations of the analyzed structure are depicted in Figure 6.6. Both beams and columns were dimensioned equally and reinforced to provide equal moment capacity. This dimensioning and reinforcement scheme adheres with the strong column-weak beam philosophy which encourages the formation of plastic hinges in the beams during extreme loading events. Each member in the analyzed beam-column joint was modeled to the point of contraflexure under lateral load, i.e. the mid-span point. Consequently, only half of each member (the beam and the columns above and below the joint) was modeled. The boundary condition at the bottom end of the column was pinned, i.e. displacement is fixed and rotation is free, while the top end of the column is fixed in the X-direction with Y-direction movement and rotation

free. The end of the beam was left free in all degrees of freedom. A constant compressive axial load equivalent to 10% of the column's compressive strength was applied at the top of the column to simulate gravity loads.

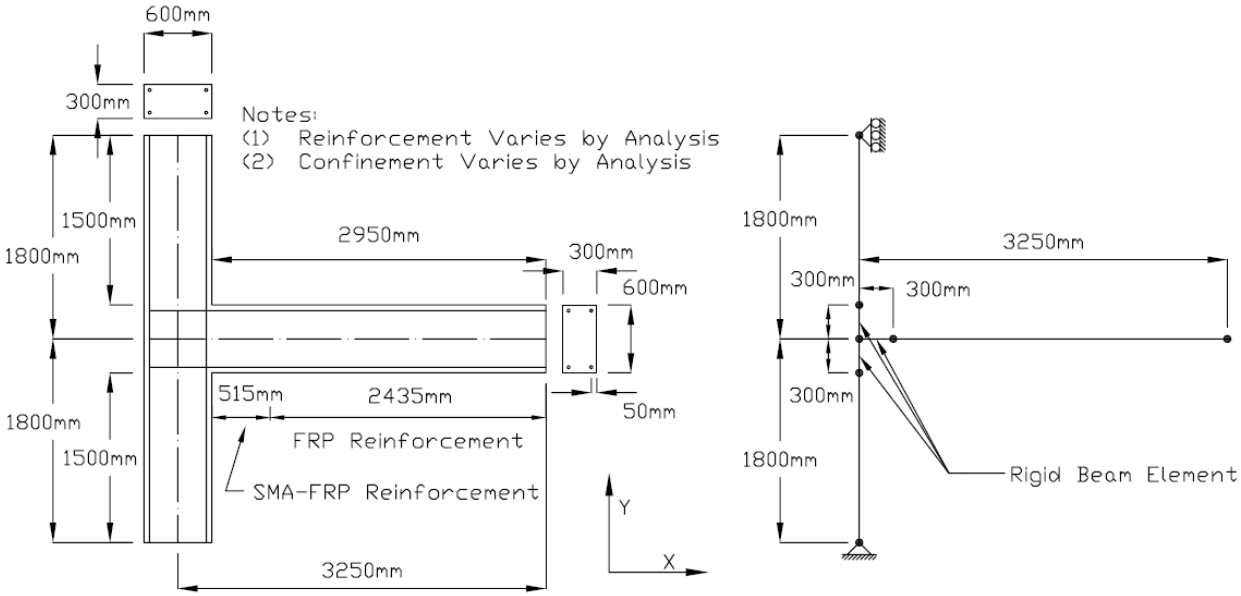

(a) (b)

Figure 6.6: Beam-column joint
a) Physical representation b) Finite element representation

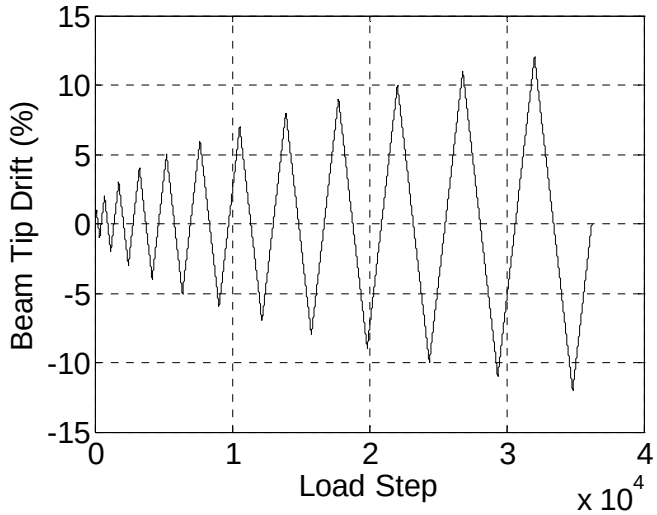

Figure 6.7: Displacement load pattern for analysis of beam-column joint

The material models used in this analysis for the FRP and SMA-FRP reinforcement, as well as the concrete, can be found in Chapter 5. Both beams and

columns were modeled using 7 integration point nonlinear force-based beam-column elements. Since it is not cost effective to use SMA-FRP composite reinforcement throughout the entirety of a structure or member, the beam's plastic hinge region was selectively reinforced with SMA-FRP composite reinforcement in only the beam integration points closest to the joint. This corresponds to SMA–FRP reinforcement being used for a distance of 515 mm from the face of the column. Outside this plastic hinge region, FRP reinforcement was exclusively used. Because inelasticity was designed to be concentrated in the plastic hinge region of the beam, the deformation and inelasticity in the joint itself was neglected; consequently, the joint was modeled with rigid beam members and dimensioned so that only the clear span length of the beams and columns was considered. The model was statically loaded in the Y direction of the free beam end with the cyclic displacement pattern shown in Figure 6.7. In this figure, drift is defined as the vertical displacement of the beam tip divided by the length of the beam element.

In addition to the type of reinforcement present in the plastic hinge region, the effect of the confinement of the core concrete and the moment capacity of the members were investigated. The effect of the confinement was included by performing analyses at the three levels of confinement that were previously discussed in Figure 5.5. The moment capacity of the members was investigated by performing analyses at moment capacities ranging from 500 kN-m to 900 kN-m in 50 kN-m increments. The reinforcement ratio necessary for a particular moment capacity for each confinement level and reinforcement type was determined using the results from the moment-curvature analysis presented in the preceding section. An example of the results from

this analysis are seen in Figure 6.8, which shows the beam tip load versus beam tip drift in the vertical direction for the end of the beam for highly confined specimens with a moment capacity of 600 kN-m analyzed in this study. As typically observed in this analysis, these results show that the specimens with SMA-FRP in the plastic hinge zone exhibit a ductile response and dissipate more hysteretic energy when compared to the exclusively FRP reinforced specimen.

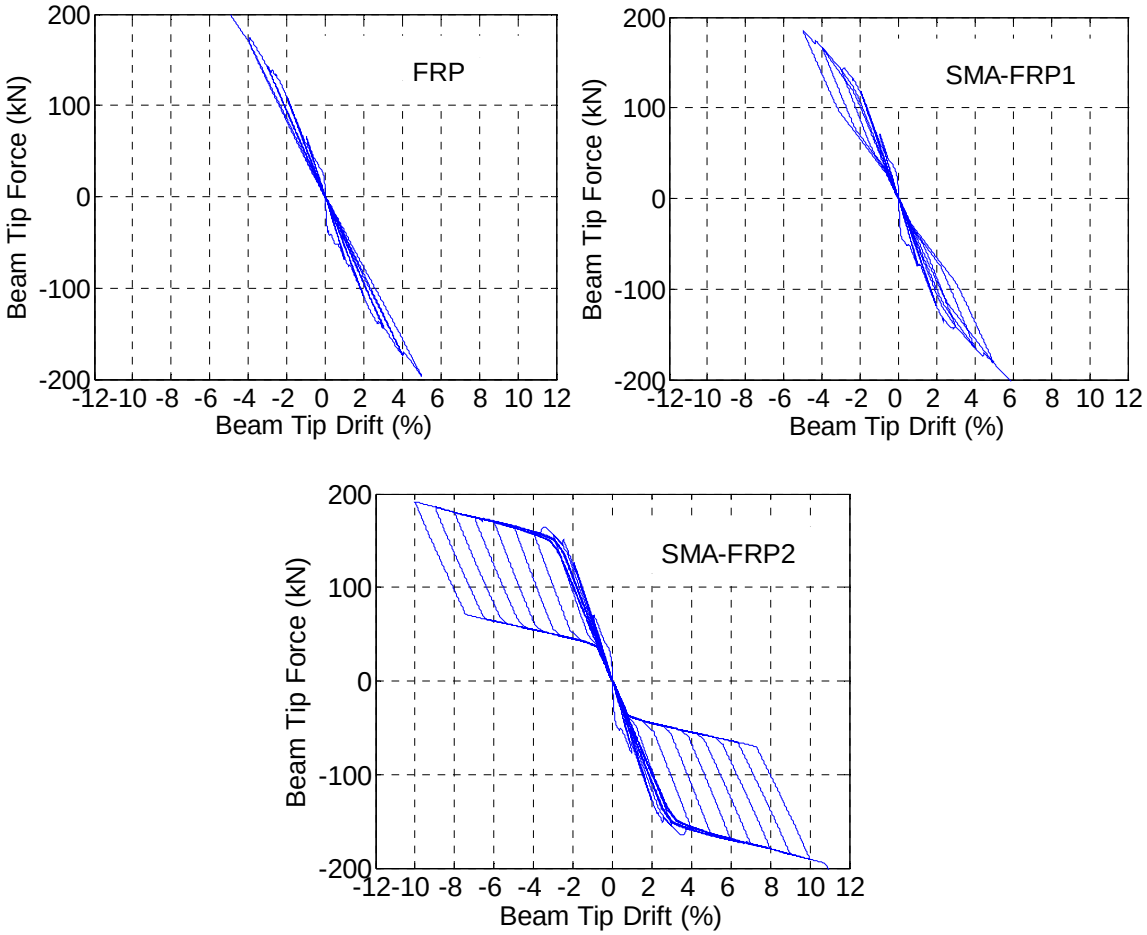

Figure 6.8: Beam tip force vs. vertical beam tip displacement from highly confined specimens with a moment capacity of 600 kN-m in the beam-column joint study

These figures also show that there is not significant visible degradation in the hysteresis; however, with increased strain and cycling one might expect to see

degradation due to the concrete deterioration. Once again, to explain this phenomenon the behavior of the materials is examined. Figure 6.9 shows the stress-strain relationship for the core concrete and SMA-FRP reinforcement at the top of the SMA-FRP2 reinforced specimen and at the first integration point of the member. In this figure points are noted on the curves when specific drift levels in the member are reached. As one can see from this figure the confined core concrete does degrade at relatively high levels of compressive stain; however, as the concrete degrades more stresses move to the reinforcement in compression. Because the sections have equal top and bottom reinforcement, the tensile stress can be kept in equilibrium with the compressive reinforcement. As was the case in the first case study, this stress balance is responsible for the lack of major degradation in the load-deformation hysteresis seen in Figure 6.8.

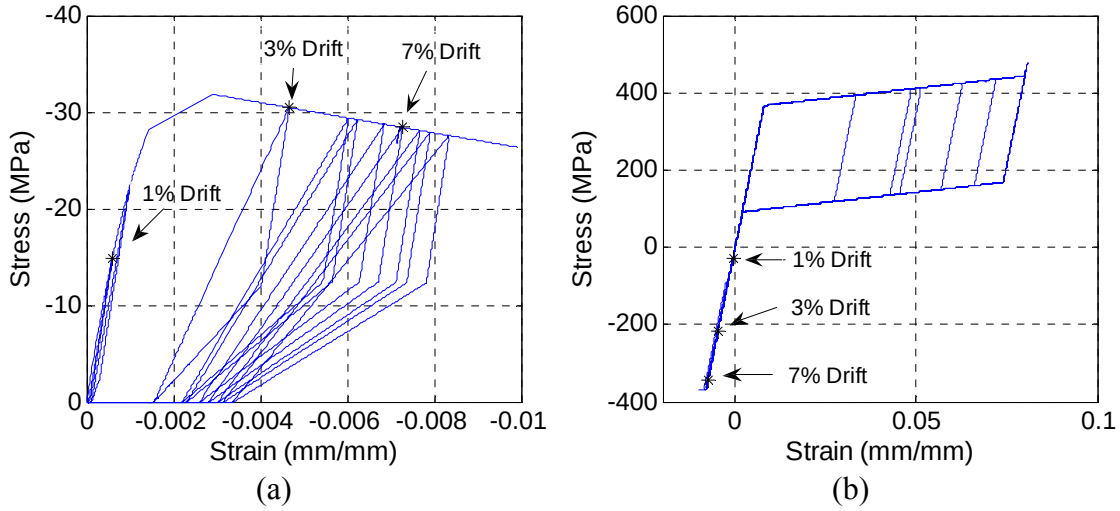

Figure 6.9: Stress vs. strain in the (a) Core concrete (b) SMA-FRP reinforcement at the top of the SMA-FRP2 reinforced section with 600 kN-m capacity and high confinement

To evaluate the results from this study, several response parameters were quantified and compared: 1) drift capacity 2) damping ratio and 3) displacement ductility.

Each of these parameters represents key characteristic of the performance of the substructure. Parameters 1 and 3 provide insight on the deformation performance of the substructure while parameter 2 provides information on its energy dissipation capability.

Drift Capacity

The drift capacity of the substructure is important when assessing a structures performance to given deformation demands. The drift capacity results from the specimens in this analysis are shown in Figure 6.10. From these results it was found that the drift capacity is lowered when the confinement level is reduced regardless of the reinforcement type. Furthermore, SMA-FRP reinforcement at high and medium confinement levels show an improvement in drift capacity compared to FRP reinforced model, with up to 20% and 125% increase in drift capacity, for SMA-FRP1 and SMA-FRP2, respectively, given the same moment capacity and confinement level. However, at low confinement the drift capacities of the SMA-FRP reinforced beam-column joint are not significantly different than that of the FRP reinforced joint. After the SMA-FRP2 reinforced specimen's failure limit state changes from crushing after strain hardening to crushing before SMA strain hardening, which occurs at around 650 kN-m for the high confinement specimen, increasing the moment capacity lowers drift capacity of the SMA-FRP2 reinforced model. Increasing the moment capacity has a smaller effect on both the FRP and SMA-FRP1 reinforced model, with both minor increases and decreases observed.

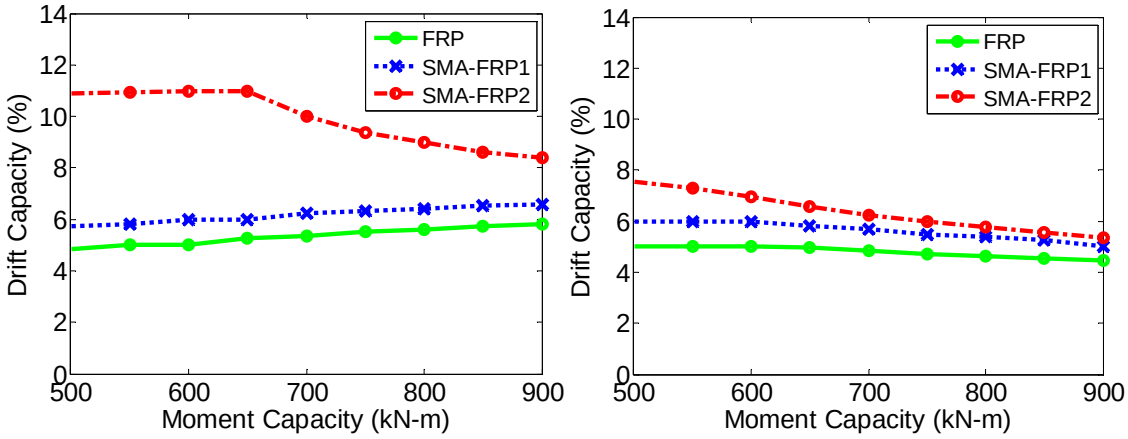

(a) High Confinement (b) Medium Confinement

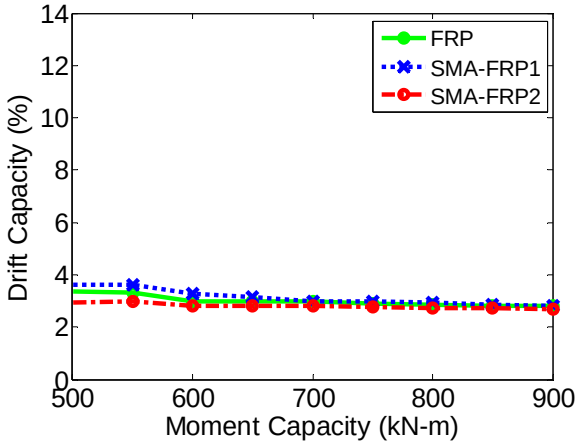

(c) Low Confinement

Figure 6.10: Drift Capacity vs. Moment Capacity

Energy Dissipation

The damping provided by a structure is an important parameter because it is linked to the energy dissipated by the structure. With the data from the last completed cycle of each specimen before failure, the viscous damping of an equivalent linear system, ζ_{eq}, was calculated for each model using equation 6.1. Figure 6.11 shows the ζ_{eq} versus the moment capacity results from this analysis. From this one can see that the maximum damping ratio for the SMA-FRP1 and SMA-FRP2 reinforced joints were 101% and

475% higher than the maximum ratio for the FRP reinforced model, respectively. It is also clear from this figure that energy dissipation decreased dramatically as the confinement level was lowered and the moment capacity was increased, with almost no difference in energy dissipation for all three models at low confinement and high moment capacity. This decrease is attributed to the fact that lowering the confinement and increasing the moment capacity lowers the frame's ultimate drift capacity and thus, lowers the amount of hysteretic area that can be utilized to accumulate energy dissipation and provide damping to the structure.

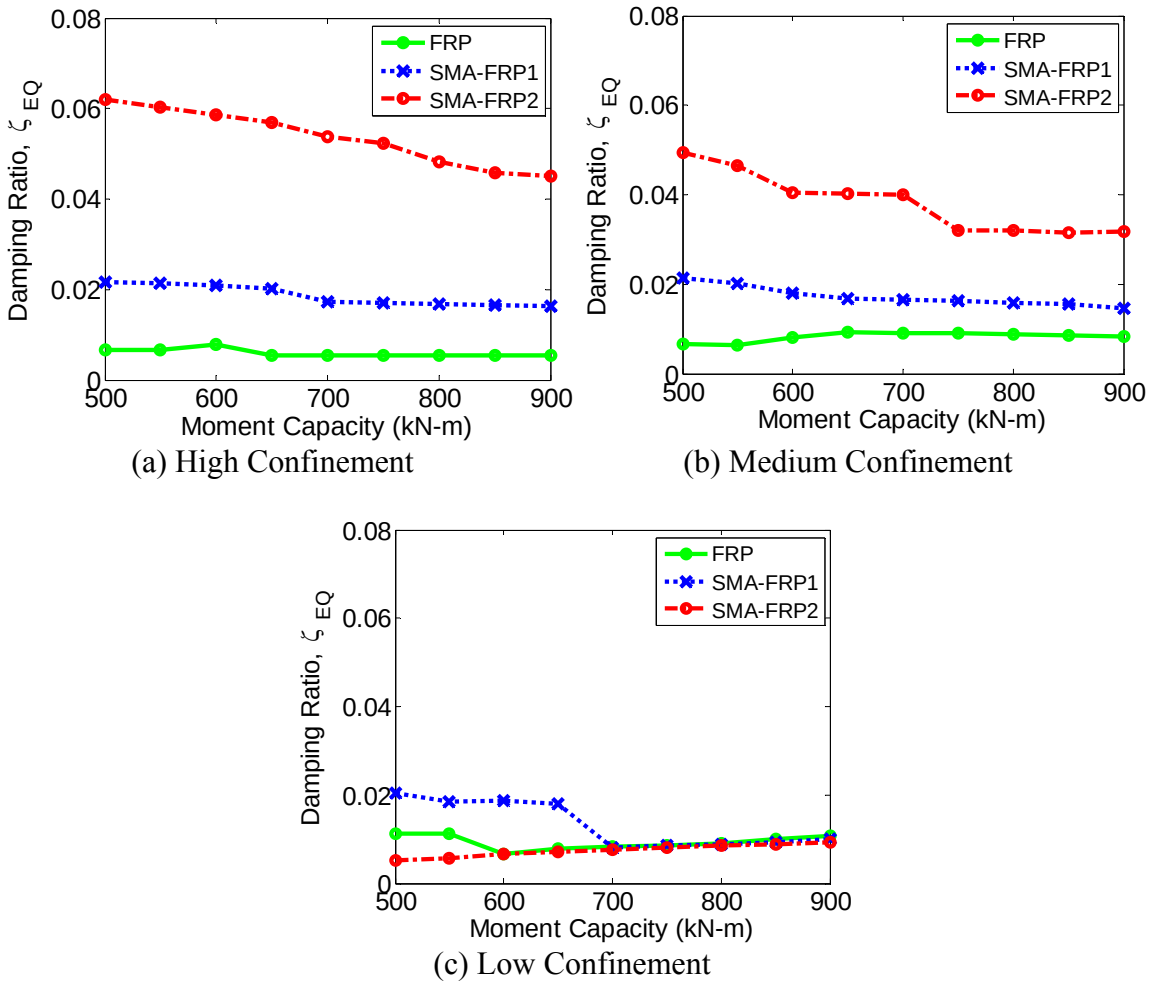

(a) High Confinement

(b) Medium Confinement

(c) Low Confinement

Figure 6.11: Damping Ratio vs. Moment Capacity

Ductility

One of the important advantages sought from replacing FRP bars with SMA-FRP reinforcement is the improvement in ductility capacity. In the previous moment-curvature analysis, the ductility of the section was measured with the curvature ductility; on the larger scale of the beam-column-joint, ductility can be measured with displacement ductility. In this analysis, displacement ductility is calculated by dividing the maximum displacement reached before failure by the displacement at which the SMA fibers experience phase transformation (yields). Since FRP does not yield, the ductility of the FRP reinforced specimens is, by definition, unity. The resulting relationship between ductility and moment capacity is found in Figure 6.12. From this figure it was found that the ductility of the SMA-FRP reinforced specimens generally decreases as the confinement level is lowered. The SMA-FRP2 reinforced specimens proved to be more sensitive to this decrease as the maximum decrease in displacement ductility was 74% when comparing high and low confinement specimens at the same moment capacity, however, for the SMA-FRP1 case the maximum decrease was 57%. This higher sensitivity to confinement level can be attributed to the fact that the SMA-FRP2 reinforced members accumulate most their displacement ductility at high curvature levels, which require both high reinforcement strain and high concrete strain. At low and medium confinement it is also seen that the ductility of SMA-FRP1 reinforced models are sometimes higher than SMA-FRP2 reinforced models. This peculiar result occurs because a higher amount of SMA-FRP2 is required to achieve a given moment capacity, which delays yielding and at lower confinement levels can lead to a reduction in ductility. From Figure 6.12 was also found that increasing the moment capacity generally

decreases the ductility of SMA-FRP2 reinforced specimens, but has much less effect on the ductility of SMA-FRP1 reinforced specimens. Again, this is due to the sensitivity of SMA-FRP2 reinforced members to the ultimate curvature of the section, which is lowered substantially with increased reinforcement ratio.

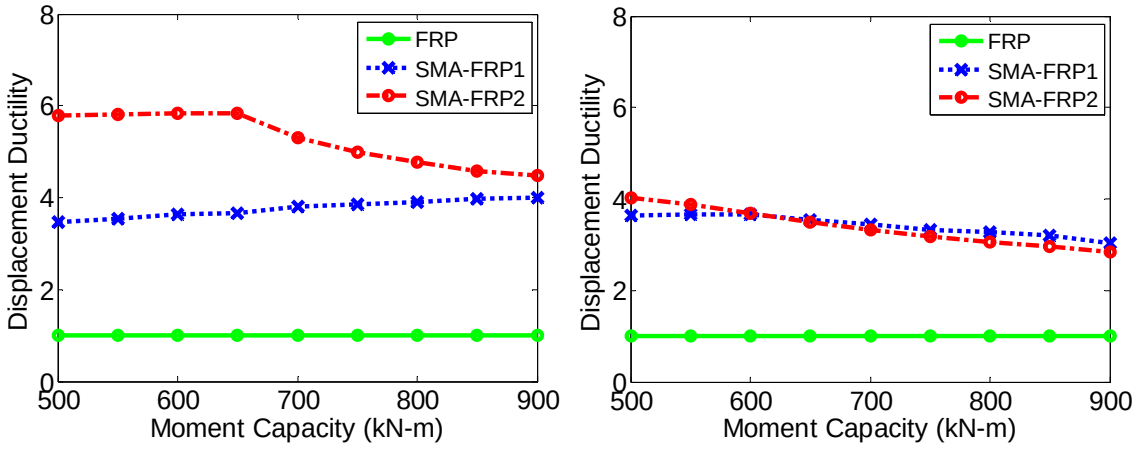

(a) High Confinement (b) Medium Confinement

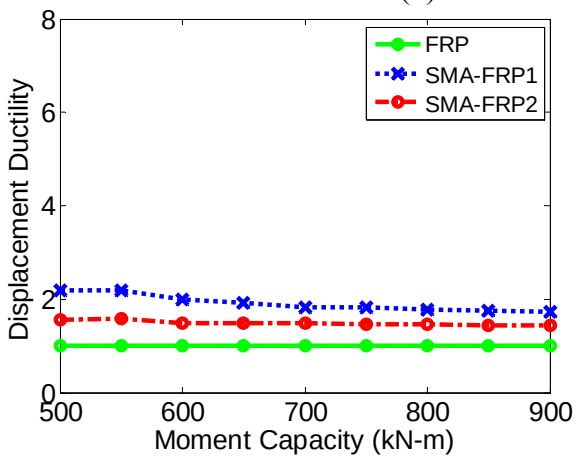

(a) Low Confinement

Figure 6.12: Displacement Ductility vs. Moment Capacity

CHAPTER 7:

FRAME ANALYSIS

Thus far, SMA-FRP reinforcement has been explored at the material, section, and subassemblage level, now as a final step, SMA-FRP reinforcement in a structural system will be explored. Accordingly, this chapter presents an analytical study of a concrete frame structure with SMA-FRP reinforcement that is subjected to seismic loading.

7.1 ANALYTICAL MODEL

The model structure for this analysis is a 1 Bay – 3 Story reinforced concrete frame (see Figure 7.1). The section dimensions of the beams and columns in the structure are equal and set at 600 mm x 300 mm. The structure was primarily reinforced with FRP, but to evaluate the performance of SMA-FRP reinforcement, the model was analyzed with all beam plastic hinge zones reinforced with the two types of SMA-FRP considered in this study (see Figure 5.3), as well as GFRP. Once again in this model, force-based beam-column elements were utilized for both beam and columns, while the deformation and inelasticity in joint itself was neglected by using rigid links to represent the beam-column joint. Mass was lumped at the nodal points; thus, the beams were discretized into two separate elements so that mass can be lumped at a node along the beam span. The base of each column was fixed in all DOFs. As demonstrated by both the moment-curvature analysis and the substructure study on the beam-column joint, the effectiveness of SMA-FRP composite reinforcement is rapidly diminished as the confinement of the section is reduced. Because of this, and the fact that most codes require that concrete structures in

high seismic zones be detailed to ensure adequate confinement, only the high level of confinement (see Figure 5.5b) was considered in this section. Beams were reinforced to deliver a moment capacity of 600 kN-m, while column reinforcement levels were designed such that the frame follows the weak-beam, strong-column principle.

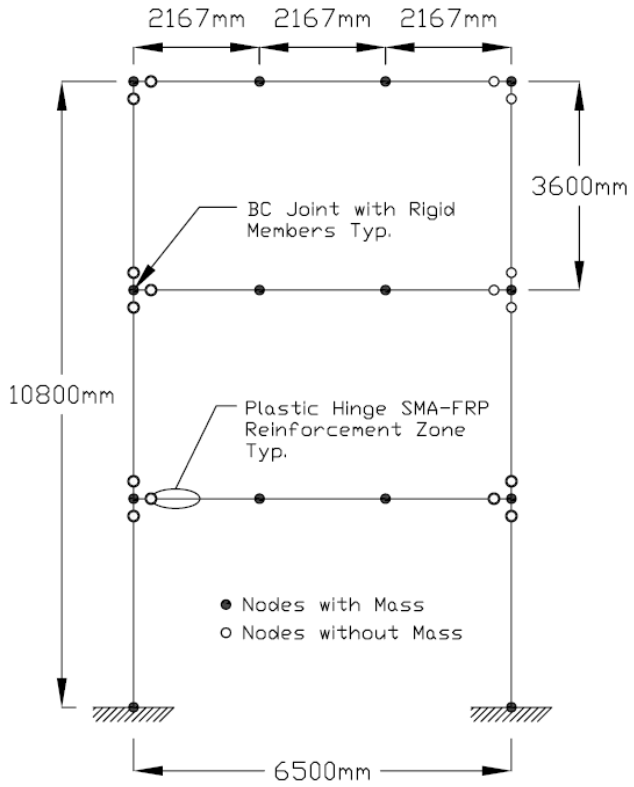

Figure 7.1: Model of the frame structure used in the analysis

Modal analysis was performed before the loading was applied on frames with each plastic hinge reinforcement type. Table 7.1 shows the resulting first three natural periods of the frames. From this table one can see that the natural periods of the frame were similar, regardless of plastic hinge reinforcement type. This is to be expected since much of the stiffness of the frame is derived from the concrete, which is the same in each case. Furthermore, similar periods are expected because the initial stiffness of each hinge

reinforcement type was similar, and the reinforcement in areas outside the beam plastic hinge zone was identical in all three structures. Additionally, this modal analysis showed that each frame type had very similar mode shapes. Figure 7.2 shows the first three resulting mode shapes of the frame with SMA-FRP2 hinge reinforcement. Due to the similarity in modes shapes, the mode shapes for the frames reinforced with FRP or SMA-FRP1 in the hinge are not shown. The mode shapes shown in Figure 7.2, in particular, the first mode shape, are typical for a concrete frame structure of this height. Using this modal information, the first two modes of each frame were damped by 5% through the use of Raleigh damping.

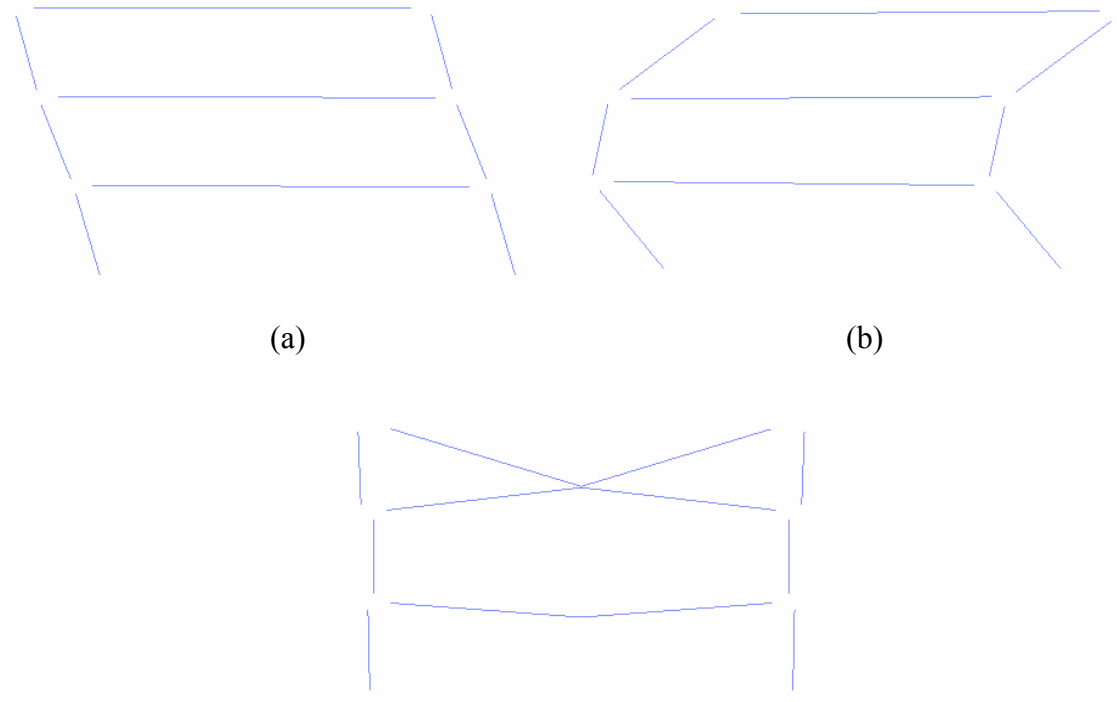

Figure 7.2: Mode Shapes of frame reinforced with SMA-FRP2
(a) Mode 1 – T =0.404 sec (b) Mode 2 – T = 0.115 sec (c) Mode 3 – T = 0.073 sec

Table 7.1: Natural periods of frames given reinforcement type (sec)

Mode	Hinge Reinforcement Type		
	GFRP	SMA-FRP1	SMA-FRP2
1st	0.408	0.406	0.404
2nd	0.116	0.115	0.115
3rd	0.073	0.073	0.073

7.2 EARTHQUAKE PROPERTIES

The seismic performance of this frame was evaluated by performing a dynamic analysis with three earthquake ground motion records:

- Beverly Hills - Mulhol Station record of the 1994 Northridge earthquake
- Shin-Osaka Station record of the 1995 Kobe earthquake
- Capitola Station record of the 1989 Loma Prieta earthquake

Table 7.2 summarizes some of the key parameters of these earthquake records. Additionally, Figure 7.3 shows the unscaled ground acceleration time history for each of these earthquake records.

Table 7.2 Ground Motion Records Properties

Earthquake	Northridge - 1994	Kobe - 1995	Loma Prieta - 1989
Station	Beverly Hills - Mulhol	Shin-Osaka	Capitola
PGA (g)	0.52	0.24	0.53
PGV (cm/s)	63	38	35
Mechanism	Thrust	Strike-Slip	Strike-Slip
Epicentral Distance (km)	13.3	46	9.8
Record Duration (sec)	29.95	40.95	39.95
Magnitude, M_L	6.7	6.9	6.9

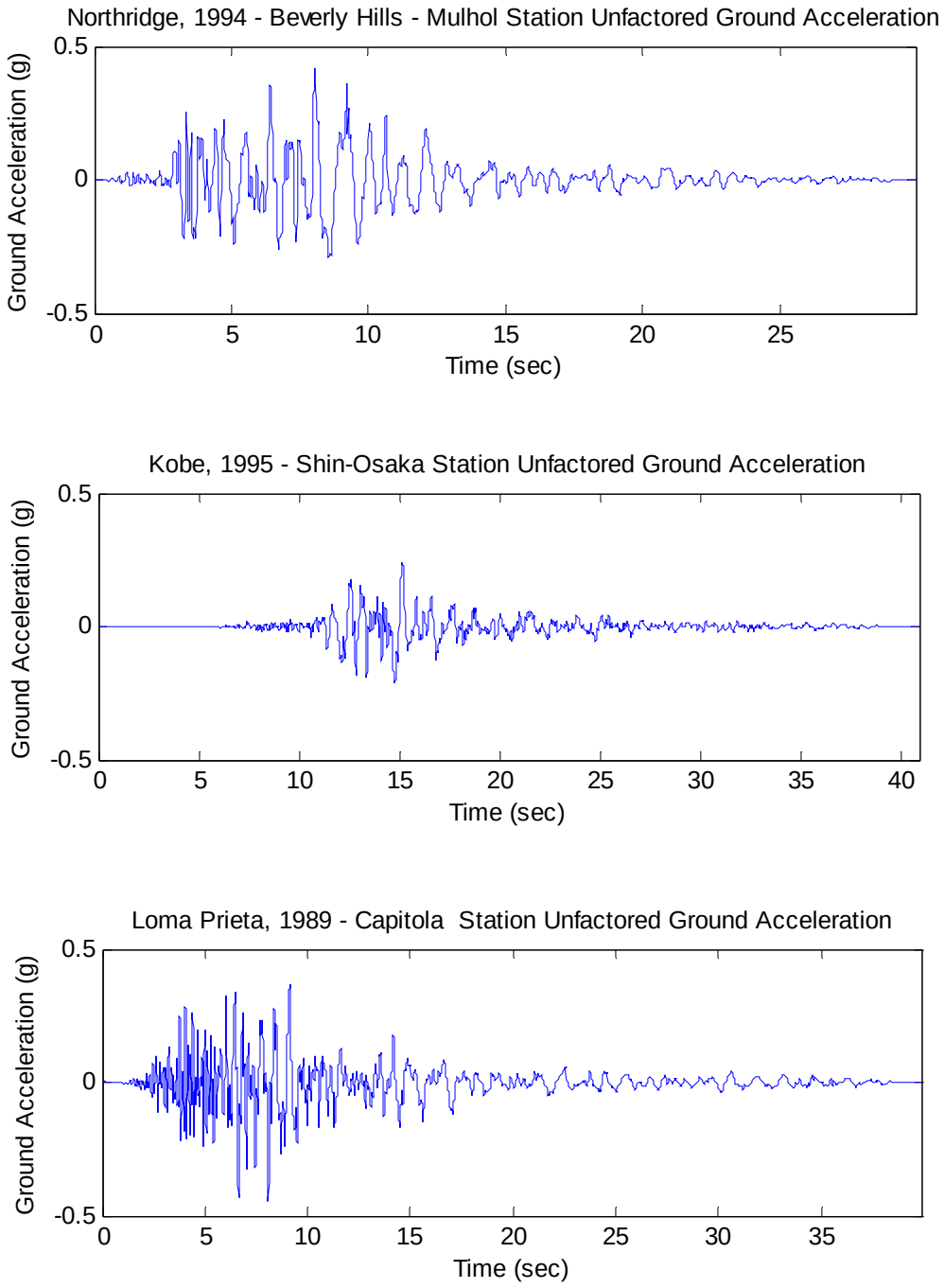

Figure 7.3: Unscaled ground acceleration time histories

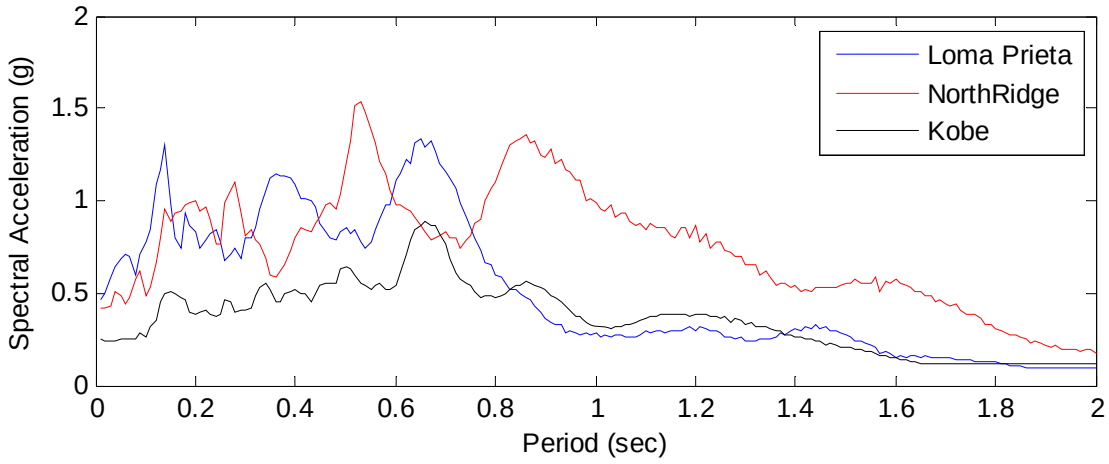

Figure 7.4: Pseudo acceleration spectra for selected ground acceleration time histories

For each of these earthquakes records, the pseudo acceleration spectrum assuming 5% damping was calculated from the ground acceleration time history data. The results of this calculation are shown in Figure 7.4. Through inspection of this figure one can see that in each case, the first natural period of the building is located in or near an area of relatively high spectral demand. Additionally, one can see that with increasing period, the spectral acceleration for the Loma Prieta earthquake record reduce faster than the Northridge or Kobe record. This may prove important depending on how much the period of the building increases as damage starts to accumulate. Finally, it is seen that the maximum spectral acceleration for the Northridge and Loma Preita earthquake records are similar, but the maximum spectral acceleration for the Kobe earthquake is significantly smaller. This difference is primarily due to the lower PGA of the unscaled Kobe time history; this will not be a problem as the scaling of the record will address this issue.

7.3 INCREMENTAL DYNAMIC ANALYSIS

The analysis method chosen to evaluate the performance of the previously introduced frame model was the incremental dynamic analysis (IDA). The IDA method was used in structural analysis as early as 1977, but has become more popular in recent years, in part, due to advancements in computer technologies [Bertero 1977, Vamvatsikos and Cornell 2001]. The popularity and widespread acceptance of IDA was demonstrated by its inclusion in design guidelines published by FEMA [FEMA 2000]. As part of an IDA a model is analyzed with a ground acceleration time history at various levels of intensity. The desired level of intensity is achieved by scaling the time history record. This scaling can be based on many different quantities, such as PGV, spectral acceleration, etc. In this analysis, scaling via PGA was chosen since it is a commonly used technique and has the advantage of simplicity. Once these multiple analyses are completed, the data can then be post-processed to extract important parameters of the response, often referred to as structural state variables. These response parameters can then be plotted together to form curves that show the progression of the structure and its response parameters as the intensity of the demand increases. The resulting IDA curves are often dependent on the input time history, so this type of analysis is often performed using multiple records. In the analysis presented below, the maximum PGA increment between analyses was 0.3g. The PGA increment was decreased as the frame approached its maximum survivable PGA, and as needed throughout the analysis to provide definition to the IDA curves.

7.4 RESULTS AND DISCUSSION

An example of the results from the analysis described above is shown in Figure 7.5, which shows the base shear vs. average roof drift ratio plots for frames subjected to the Northridge earthquake. In this plot, for each reinforcement type, the earthquake record was scaled to the maximum survivable PGA. This corresponded to the maximum PGA earthquake in which all the members of the frame did not reach a failure limit state. The failure limit states for this model differed depending on the reinforcing material in the section of interest. For FRP and SMA-FRP1 reinforced sections, failure was defined as either crushing of the core concrete or rupture of the conventional fibers in the reinforcement. For the SMA-FRP2 reinforced section, failure was defined only as crushing of the core concrete. From Figure 7.5 one can see the hysteretic nature of the base shear vs. roof drift ratio response for each reinforcement type. From this figure it is clear that the SMA-FRP1 reinforced frame shows similar performance when compared to the FRP reinforced structure; however, SMA-FRP2 reinforced frame clearly shows superior performance in terms of drift ratio and energy dissipation. Additionally, this figure shows that, when compared to the GFRP reinforced frame, both SMA-FRP reinforced frames reached higher maximum roof drift levels. Compared to the GFRP frame, this increase was 15.4% and 64.9% for the SMA-FRP1 and SMA-FRP2 reinforced frames, respectively. Likewise, the SMA-FRP reinforced frames, when compared to the GFRP reinforced frame, show more hysteretic area contained within the curve. 5% and 286% more energy was dissipated, when compared to the FRP reinforced frame, by the SMA-FRP1 and SMA-FRP2 reinforced frames, respectively. To provide a quantitative evaluation of the performance of the SMA-FRP composite reinforcement in the frame,

IDA curves showing the maximum base shear vs. the maximum drift ratio were calculated for each acceleration time history record (see Figure 7.3).

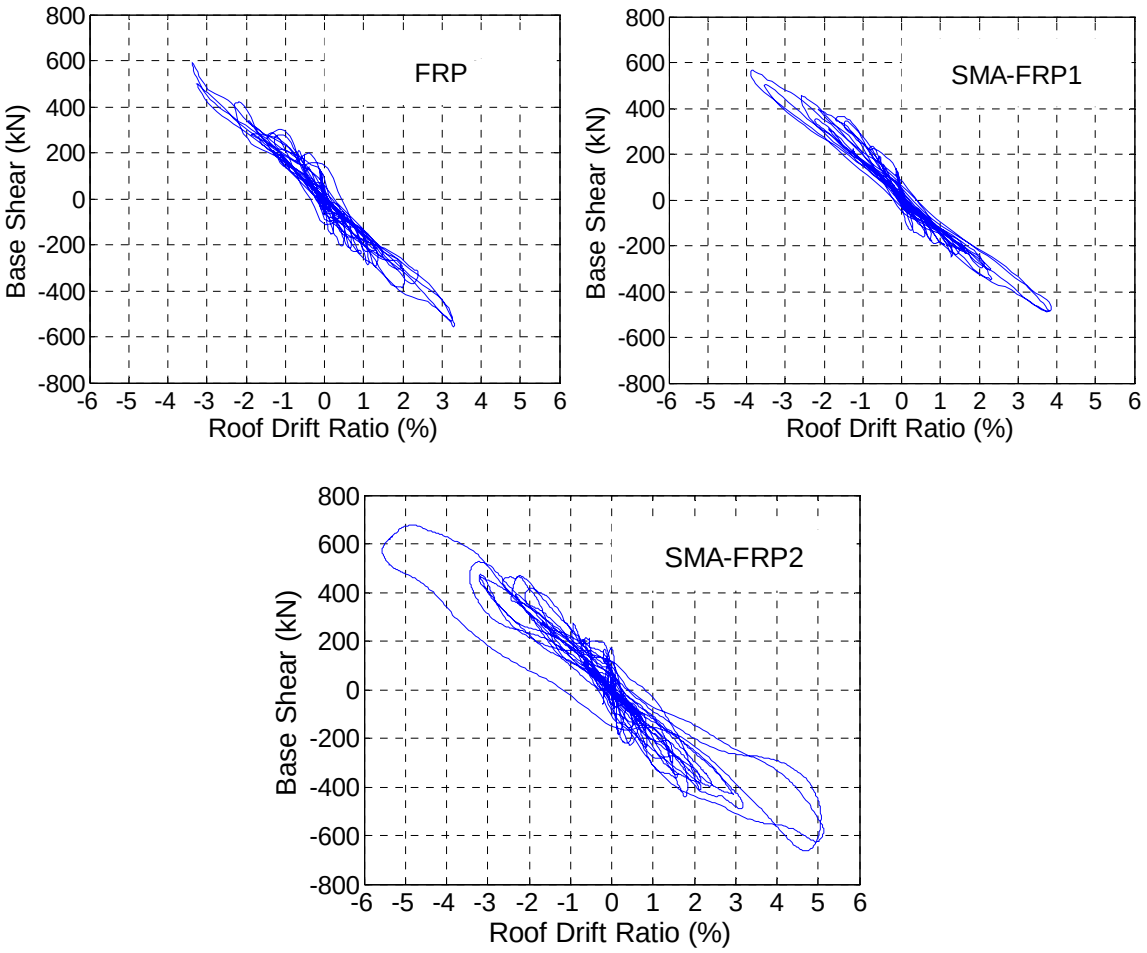

Figure 7.5: Base shear vs. roof drift ratio (a) Northridge, Beverly Hills – Mulhol Station (b) Kobe, Shin – Osaka Station (c) Loma Prieta, Capitola Station ground acceleration time histories scaled to maximum PGA

Figure 7.6 shows IDA curves of the maximum base shear vs. the maximum story drift ratio for each frame type and earthquake record. Additionally, in this figure plots are shown of the PGA of the analysis vs. the story drift ratio; this plot can be used to relate both the maximum base shear and story drift to the time history record intensity. From this figure one can see that the IDA curves for the different reinforcement types

follow very similar and partially overlapping paths. However, the frames reinforced with SMA-FRP persist longer in the IDA and reach higher levels of PGA, drift ratio, and, in most cases, base shear. This initial overlap is due to the fact that the overall stiffness properties of the frames are very similar; this was demonstrated previously by a modal analysis, which showed very similar periods and mode shapes. This is expected because the frames are almost identical, where the only difference being the reinforcement in the plastic hinge zones of the beams.

As indicated by the results of the IDA, the drift ratio capacity was higher for each earthquake for both the SMA-FRP1 and SMA-FRP2 reinforced frames, up to 16% and 66%, respectively, when compared to the GFRP reinforced frame. This was expected due to the better curvature ductility and drift performance of SMA-FRP reinforcement in the section and substructure analyses (see Figure 5.7 and Figure 6.10 for examples). Additionally, these same analyses showed superior performance for SMA-FRP2 reinforcement, when compared to SMA-FRP1, so it is not surprising that the SMA-FRP2 reinforced frame has a higher drift ratio capacity. Despite the higher drift capacity of the SMA-FRP reinforced frames, these frames show only a modest, if any, increase of base shear capacity. This is expected because the frames are designed and reinforced to have the same moment capacity, regardless of reinforcement type. Additionally, this is a positive result because it shows the ductility of SMA-FRP reinforced frames, which is one of the main reasons SMA-FPR reinforcement is being studied.

From Figure 7.6 it is also seen that, given a reinforcement type, there is not a dramatic variation in the base shear capacity or drift ratio capacity for the different earthquake results. For example, maximum drift ratio of the SMA-FRP2 reinforced

frames varied between 5.3% and 6.3%, and the maximum base shear for the SMA-FRP1 reinforced frame varies from 544 to 568 kN. This similarity in base shear and drift ratio capacity suggests that these properties are more insensitive to the particular ground motion than other parameters, such as energy dissipation. A possible reason for this is that the moment and curvature capacities of each section were defined independently of the loading type.

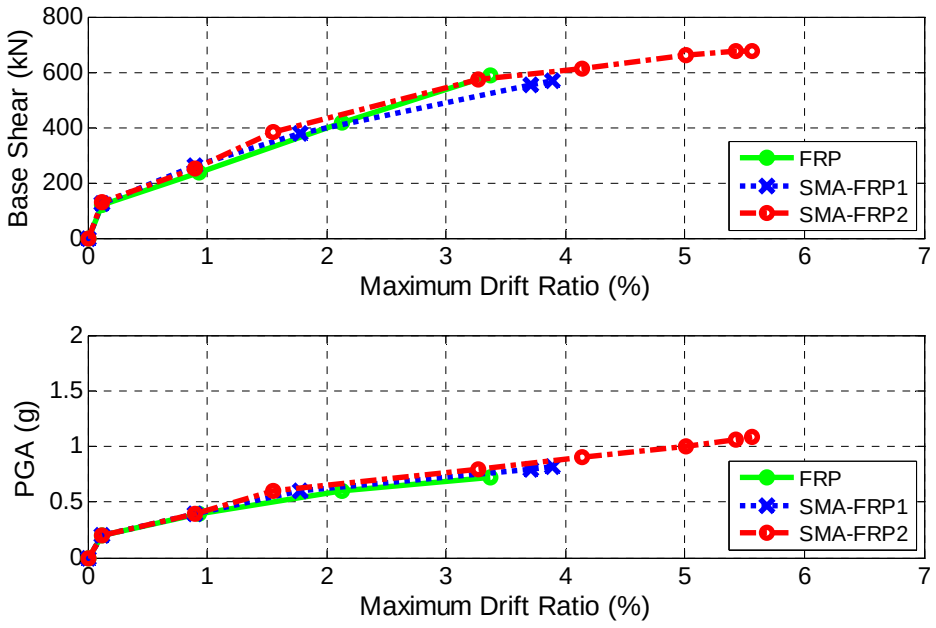

(a)

Figure 7.6: IDA Results (a) Northridge, Beverly Hills – Mulhol Station (b) Kobe, Shin – Osaka Station (c) Loma Prieta, Capitola Station

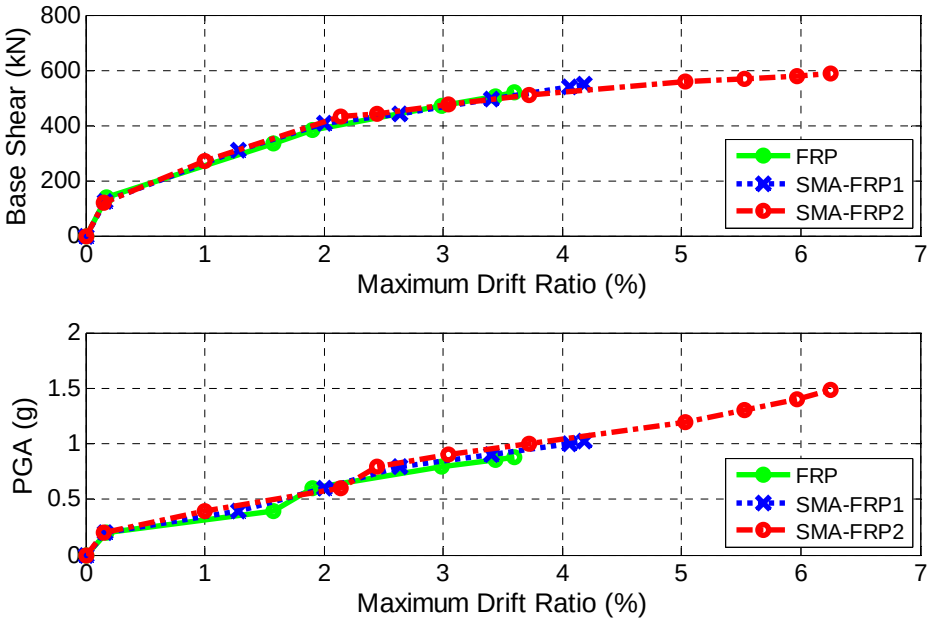

(b)

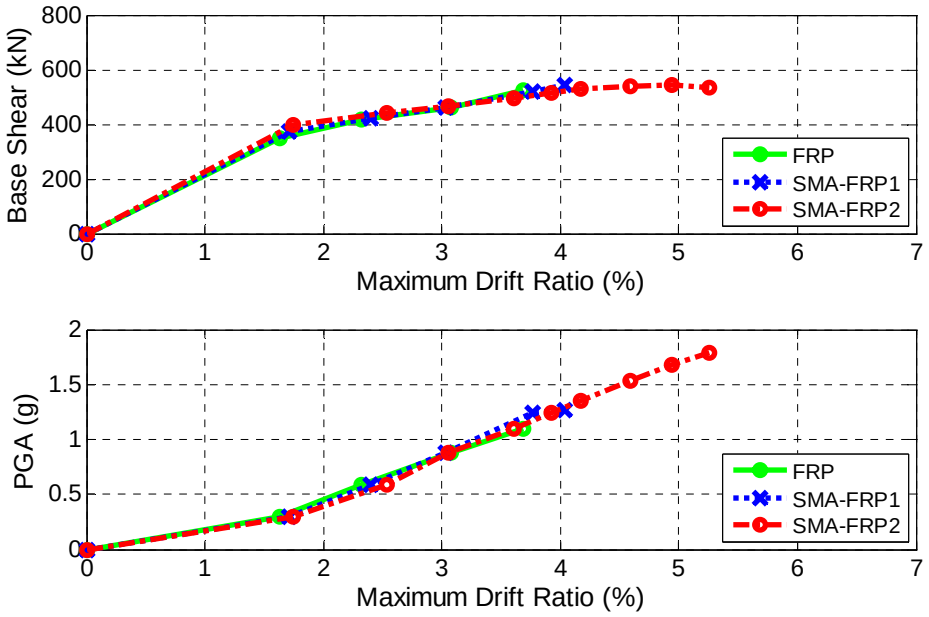

(c)

Figure 7.6 (cont.)

Figure 7.7 shows that, as mentioned previously, the SMA-FRP reinforced frames have higher maximum PGA for all the earthquake records analyzed. This figure shows

the normalized maximum PGA each model could withstand before failure for each earthquake. In this figure normalization is done by dividing the maximum PGA withstood by the frame for each reinforcement type by the maximum PGA obtained by the GFRP reinforced frame, for each earthquake. From this figure one can see that the SMA-FRP reinforced frames reach higher normalized PGA in all the analysis sets. The average maximum PGA increased 15% and 61% for the SMA-FRP1 and SMA-FRP2 reinforced models, respectively, when compared to the FRP reinforced model. The increase in maximum survivable earthquake seen in this analysis is most likely due to the higher ductility of the SMA-FRP reinforced beam plastic hinge sections.

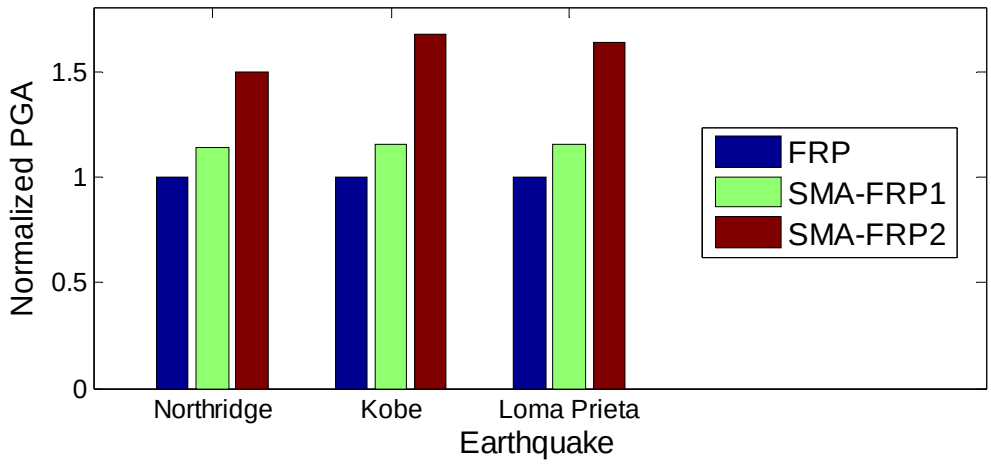

Figure 7.7: Relative maximum PGA

The energy dissipated by the frame in each analysis is plotted in Figure 7.8. For this figure, the energy dissipated was calculated by determining the area contained within a plot of the total lateral base reaction and the average roof displacement. From this figure it is seen that in all cases, the SMA-FRP reinforced models dissipate more energy

than the FRP reinforced models. The increase in energy dissipation varies from 5% to 67% for SMA-FRP1 reinforced models and 254% to 299% for SMA-FRP2 reinforced models, when compared to the FRP reinforced models. This is consistent with the results of the substructure analyses, which showed that SMA-FRP2 has a greater potential for energy dissipation. This greater potential comes from the fact that the stress-strain curve of SMA-FRP2 contains more hysteric area than the curve for SMA-FRP1, see Figure 5.3.

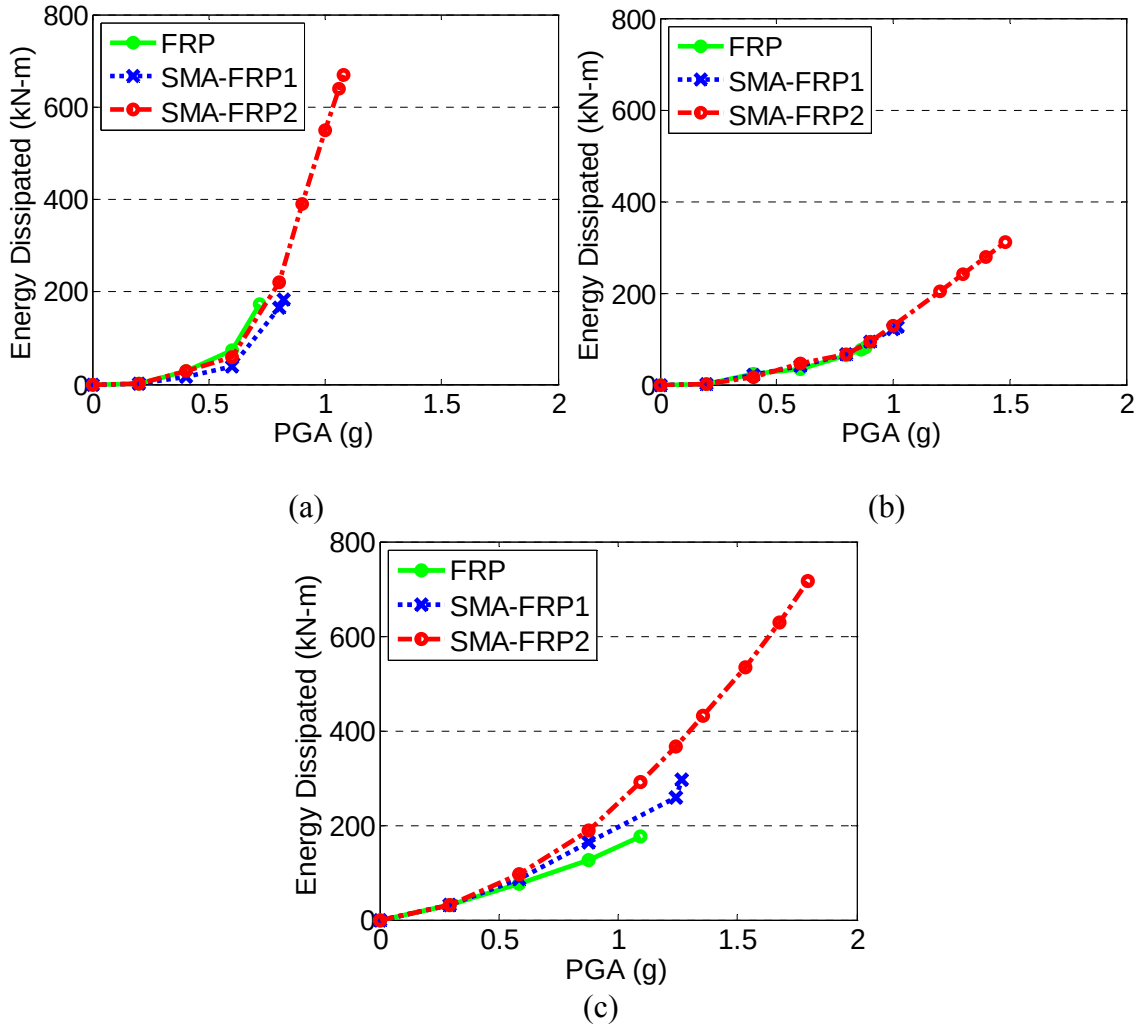

Figure 7.8: Dynamic Analysis Results – Energy Dissipation (a) Northridge (b) Kobe (c) Loma Prieta

One can also see from Figure 7.8 that the maximum energy dissipated was not the same for every earthquake. This can be explained using Figure 7.9, which shows the SMA-FRP2 stress-strain history from the maximum PGA earthquake for the Northridge and Kobe records. In both cases this stress-strain curve is from the top reinforcement in the beam integration point closest to the 1st story beam-column joint on the left side of the frame. This figure shows that this reinforcement was subjected to many more high strain cycles in the Northridge earthquake; thus the frame was able to dissipate more energy in the Northridge earthquake, when compared to the Kobe earthquake. This behavior is not surprising when considering the ground acceleration time histories of the two earthquake records, (see Figure 7.3); the Kobe record is dominated by one large spike in acceleration, while the Northridge record shows multiple spikes of acceleration achieving near maximum values.

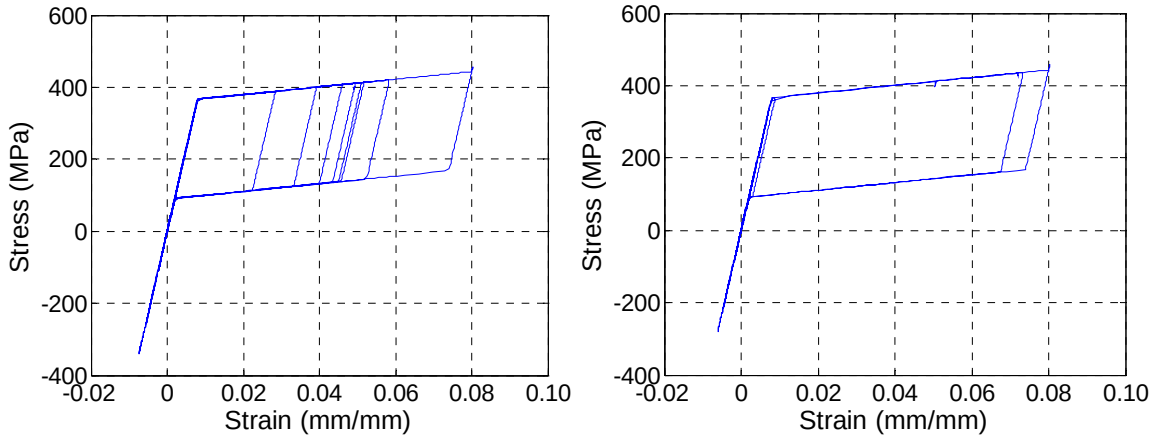

Figure 7.9: SMA-FRP2 stress-strain results from the 1st floor beam at maximum PGA (a) Northridge (b) Kobe

CHAPTER 8:

CONCLUSIONS

This thesis explored analytically the behavior of SMA-FRP composites and the use of SMA-FRP reinforcement in concrete structures and particularly the ability of SMA-FRP reinforcement to improve the ductility and energy dissipation of FRP reinforced structures. A simplified analytical model describing the stress-strain behavior of SMA-FPR composites was developed in MATLAB based on experimental results. The model was used in a parametric study that measured the effect of three key parameters including conventional fiber reinforcement type, SMA volumetric percentage, and level of SMA prestraining on the composite's ductility and energy dissipation capabilities.

Experimental results showed that replacing 25% (by volume) of the fiberglass in a GFRP composite with superelastic SMA wires would increase the amount of ductility and elastic energy dissipated by 64% and 2.6 times, respectively. Even after the rupture of the fiberglass, the SMA-FRP specimen was able to sustain 28% of its strength until 3.8% strain, while the GFRP specimen failed at 1.63% strain. The parametric study revealed that the effectiveness of the SMA-FRP in increasing the ductility of concrete structures is highly dependent on the phase transformation strain of the SMA and the rupture strain of conventional fibers. Increasing the spacing of these two strain measures will result in a more ductile SMA-FRP. Two approaches were investigated to increase the difference between these two strain values. The first approach was through prestraining the superelastic SMA wires prior to using them in the composite, while the second

approach was through using conventional fiber reinforcement with relatively high rupture strain. The study showed that in a particular case and under the same load demands, prestraining the SMA wires increased the ductility ratio and elastic energy absorbed by 245% and 392%, respectively. However, in some cases prestraining was associated with a significant decrease in the composite's yield stress to a level where it would be unsuitable for structural applications. The study also showed that SMA-FRP composites reinforced with the high rupture strain conventional fibers such as S-Glass and aramid, dissipated, on average, 180% more energy than the composites reinforced with the moderate rupture strain E-Glass fibers. The opposite was observed with the modulus of elasticity of the conventional fibers where high modulus fibers decreased the ductility of the composite. Therefore, to increase the SMA-FRP composite's ductility and ability to dissipate energy, high strain, moderate modulus of elasticity conventional fiber reinforcement is recommended. Another key difference between the behavior of SMA-FRP and conventional FRP composites was the capacity for residual stress in SMA-FRP composites after the rupture of the conventional fibers. This characteristic is vital under extreme loading conditions where the residual stress could play a significant role in protecting the structure from collapsing. The residual stress observed in the parametric study varied from 4.6% to 52.3%.

For the study on the use of SMA-FRP reinforcement in concrete structures, two experimentally based models of SMA-FRP reinforcement were created in OpenSees. The two SMA-FRP composite types used in the analysis were SMA-FRP1 which comprised 25% S-Glass and 75% SMA, by volume, and SMA-FRP2 which was reinforced with 100% SMA. These models were then used to investigate the efficacy of

SMA-FRP composites as reinforcements for concrete structures and compare it with conventional GFRP bars. Additionally, to evaluate the effect of concrete confinement on the performance of SMA-FRP reinforcement, three confinement levels were incorporated in the analysis. Sectional analysis using moment-curvature relationships illustrated the capability of SMA-FRP reinforcements to increase the curvature ductility by up to 4.2 and 11.5 times for SMA-FRP1 and SMA-FRP2, respectively compared to GFRP reinforcement. It was also found that increasing the reinforcement ratio decreased the curvature ductility of the section for all reinforcement types, while increased its moment capacity. Furthermore, it was found that decreasing the confinement level decreased maximum moment and curvature ductility of the section, regardless of the reinforcement type.

At the substructure level SMA-FRPs were used in two case studies. The first case study was performed on a reinforced concrete cantilever beam and demonstrated the superiority of SMA-FRP to GFRP in enhancing the ductility and energy dissipation of the concrete beam, when SMA-FRP reinforcement is only provided in the plastic hinge zone near the end of the beam. Under the same load history, the damping ratio due to hysteretic area in the beam reinforced with two different types of SMA-FRP was 3 times and 8 times higher than the FRP reinforced beam. The displacement ductility of the beam reinforced with SMA-FRP composites was 2.83 and 2.65, respectively, while for the conventional FRP reinforced beam the behavior was almost linear, i.e. non-ductile.

In the second case study SMA-FRP reinforcement was investigated in the plastic hinge zone of a beam-column joint subassemblage, which was subjected to cyclical loading. The response of the beam-column joint was evaluated using three parameters;

the maximum displacement, equivalent damping factor, and the displacement ductility. Results indicated that, SMA-FRP reinforced joints have superior damping ratio compared to the FRP reinforced joint. The maximum damping ratios for the SMA-FRP1 and SMA-FRP2 cases were 101% and 475% higher, respectively, than the maximum damping ratio for the GFRP reinforced joint. It was also shown that the SMA-FRP reinforced models have better performance in terms of drift capacity (20% and 125% increase for SMA-FRP1 and SMA-FRP2, respectively) and ductility (4 and 5.8 for SMA-FRP1 and SMA-FRP2, respectively) when compared to the GFRP reinforced models. The only exception to this was seen for low confinement specimens, where ductility and drift capacity gains were low to negligible.

At the structure level an incremental dynamic analysis of a 1 bay – 3 story Frame with SMA-FRP reinforcement in the plastic hinge zones of all beams was completed with three earthquake records. While the benefits of SMA-FRP reinforcement depended on the earthquake record, the results showed that in all cases the SMA-FRP reinforced structures were able withstand higher seismic demands, measured by the maximum survivable PGA of each earthquake. The drift capacity of the SMA-FRP frames was also shown to increase by up to 16% and 66% for SMA-FRP1 and SMA-FRP2 reinforced models, respectively, when compared to the GFRP reinforced models. Additionally, the energy dissipation of SMA-FRP reinforced frames increased by up to from 67% and 299% for the SMA-FRP1 and SMA-FRP2 reinforced models, respectively, when compared to the GFRP reinforced models. These results illustrate that SMA-FRP bars have the potential of effectively reinforcing critical sections in earthquake-resistant concrete structures.

In this thesis the behavior of SMA-FRP reinforcing bars has been systematically investigated. This started with experimental tests of the properties of SMA-FRP coupons, but continued with an analytical study of SMA-FRP bars at the material level and analysis of SMA-FRP reinforced concrete structures at the section, substructure, and structural levels. At each point in this investigation, it was shown that SMA-FRP bars can provide ductility and damping that is lacked when traditional FRP reinforcement bars are considered. Logical continuations of this work include more in-depth analytical studies using less idealized SMA-FRP material models and verification thru experimental tests of SMA-FRP reinforced concrete specimens

REFERENCES

Andrawes, B. and DesRoches, R.. (2007). Effect of ambient temperature on the hinge opening in bridges with shape. Engineering Structures. 29 (1), 2294–2301.

ACI 440 (2006). "440.1R-06: Guide for the Design and Construction of Structural Concrete Reinforced with FRP Bars" American Concrete Institute, Farmington Hills, Michigan

ASTM D3039 2008 Standard test method for tensile properties of polymer matrix composites

Bakis, C. E.; Bank; L. C.; Brown, V. L.; Cosenza, E.; Davalos, J. F.; Lesko, J. J.; Machida, A.; Rizkalla, S. H.; and Triantafillou, T. C. (2001). "Fiber-Reinforced Polymer Composites for Construction—State-of-the-Art Review" Journal of Composites for Construction, 6 (2), 73-87.

Bank L.C., Oliva M. G., Russel J. S., Dieter J. S., Berg A. C., Ehmke F. G., Carter J. Hill R., Henke R., and Gallagher B. (2005). "Bridge B-20-133 on US-151 With Fiber Reinforced Polymer Reinforced Concrete Deck" Submitted to: Wisconsin Department of Transportation, University of Wisconsin-Madison, Madison, Wisconsin

Bank, L. C. (2006). Composites for Construction: Structural Design with FRP Materials. Hoboken, New Jersey: John Wiley & Sons, Inc.

Baz, A.; Imam, K., and McCoy, J. (1990) Active vibration control of flexible beams using shape memory actuators, Journal of Sound and Vibration, 140 (3), 437-456

Benmokrane, B.; Chaallal; and Masmoudi, R. (1995). "Flexural Response of Concrete Beams Reinforced with FRP Reinforcing Bars" ACI Materials Journal, 91 (2), 46-55.

Benmokrane, Brahim; El-Salakawy, Ehab; Cherrak, Zoubir; and Wiseman, Allan (2004). "Fibre reinforced polymer composite bars for the structural concrete slabs of a Public Works and Government Services Canada parking garage" Canadian Journal of Civil Engineeering 31, 732-748.

Benmokrane B, El-Salakawy E., El-Ragaby A., and Lackey T. (2006). " Designing and Testing of Concrete Bridge Decks Reinforced with Glass FRP Bars" ASCE Journal of Bridge Engineering, 11:2, 217-229

Bertero VV. Strength and deformation capacities of buildings under extreme environments. Structural Engineering and Structural Mechanics, Pister KS (ed) ; Prentice Hall: New Jersey, 1977; 211-215.

Brinson L. C. (1993). One-Dimensional Constitutive Behavior of Shape Memory Alloys:

Thermomechanical Derivation with Non-Constant Material Functions and Redefined Martensite Internal Variable. Journal of Intelligent Material Systems and Structures. 4, (229 – 242)

Bradberry, T. E. (2001). "Concrete bridge decks reinforced with fiber reinforced polymer bars." Transportation Research Record 1770, Transportation Research Board, Washington, D.C., 94–104.

Buehler, W. J. and Wiley, R.C. (1965) Nickel-base alloys, U.S. Patent 3,1 74,851

Burton, D.S. and Gao, X.. (2006). Finite element simulation of a self-healing shape memory alloy composite. *Mechanics of Materials*. 38 (1), 525-537.

Cho, Maenghyo and Kim, Sanghaun . (2005). Structural morphing using two-way shape memory effect of SMA. *International Journal of Solids and Structures*. 42 (1), 1759 1776.

Chopra A. K. (1995). Dynamics of structures, Prentice-Hall, New Jersey.

Delemont, M. A. (2001). "Seismic retrofit of bridges using shape memory alloys," Master's thesis, Georgia Institute Of Technology

DesRoches, R. and Smith, B. (2004). "Shape Memory Alloys in Seismic resistant design and retrofit: a critical review of their potential and limitations" Journal of Earthquake Engineering, 8 (3), 415-429.

DesRoches, R.; McCormick, J.; and Delemont, M. (2004). "Cyclic Properties of Superelastic Shape Memory Alloy Wires and Bars" Journal of Structural Engineering, 130 (1), 38-46.

Dolce, M. and Cardone, D. (2006). Theoretical and Experimental Studies for the Application of Shape Memory Alloys in Civil Engineering. *Journal of Engineering Materials and Technology*. 128 (1), 302-311.

FEMA. (2000). Recommended seismic design criteria for new steel moment-frame buildings. Report No. FEMA-350, SAC Joint Venture, Federal Emergency Management Agency, Washington DC, 2000.

Hamada K.; Kawano, F.; Asaoka, K. (2003), Shape Recovery of No-Ti Alloy Fiber-Reinforced Denture Base Resin by Smart Repair Process, Materials Science Forum ,426-432, 2327-2332

Harris, H.G.; Somboonsong, W.; and Ko, F.K. (1998). "New Ductile Hybrid FRP Reinforcing Bar for Concrete Structures" Journal of Composites for Construction, 2, (1), 28 37

Hebda D. A. and White S. R. (1995) Effect of training conditions and extended thermal cycling on nitinol two-way shape memory behavior" Smart Materials and Structures, 4, 298-304

Hebda, D.; Whitlock, M.; Ditman, J.; and White, S. (1995) Manufacturing of Adaptive GraphiteEpoxy Structures with Embedded Nitinol Wires, Journal of intelligent Material Systems and Structures, 6, 220-228

Hoffmann, K. H. and S. M. Zheng. "Uniqueness for Nonlinear Coupled Equations Arising from Alloy Mechanism", Preprint No. 118, Inst. fur Mathe, Uni. Augsburg (1986).

Huang, W. and Toh W. (2000). Training two-way shape memory alloy by reheat treatment, Journal of Material Science Letters, 19, 1549 – 1550

Janke L., Czaderski C., Motavalli M., and Ruth, J. (2005). Applications of shape memory alloys in civil engineering structures - Overview, limits and new ideas. *Materials and Structures*. 38 (1), 578-592.

Jonnalagadda K.; Kline, G., and Sottos, N. (1997) Local Displacements and Load Transfer in Shape Memory Alloy Composites, Experimental Mechanics, 37 (1), 78-86

Jonnalagadda K., Sottos N., Qidwai M., Lagoudas D. (1998). "Transformation of Embedded Shape". J. of Intell. Mat. Sys. and Struc., 9

Katz, A. (1999) "Bond mechanism of FRP rebars to concrete." Materials and Structures, 32, 761-768

Kuribayashi, K.; Tsuchiya, K.; You, Z.; Tomus, D.; Umemoto, M.; Ito, T.; and Sasaki, M. (2006). Self-deployable origami stent grafts as a biomedical application of Ni-rich TiNi shape memory alloy foil Materials Science and Engineering A, 419, 131–137

Lagoudas, D. C. (2008). Shape Memory Alloys: Modeling and Engineering Applications, New York, NY: Springer Science and Business Media, LLC

Lau, K. (2002) Vibration characteristics of SMA composite beams with different boundary conditions, Material and Design, 23, 741-749

Liang, C. and C. A. Rogers. 1990. "One-Dimensional Thermomechanical Constitutive Relations for Shape Memory Materials", J. Intell. Mater. Syst. Struct., 1:207-234

Liu, Y.; Lui, Y.; and Van Humbeek, J. (1999) Two-way shape memory effect developed by martensite deformation in NiTi, Acta mater. 47 (1), 199-209

Li, Hui and Liu, Zhi-qiang. (2006). Behavior of a simple concrete beam driven by shape memory alloy wires. *Smart Materials and Structures.*. 15 (1), 1039-1046.

Maji, A. K.; and Negret, I.(1998). "Smart Prestressing with Shape-Memory Alloy" Journal of Engineering Mechanics, 124 (10), 1121 – 1128

Mander, J. B.; Priestley, M. J. N.; and Park, R., "Theoretical Stress-Strain Model for Confined Concrete," ASCE Structural Journal, V. 114, No. 8, 1988, pp. 1804-1 826.

Mazzoni, S.; McKenna, F.; Scott, M. H.; Fenves, G. L. ; et al. (2009). "Open System for Earthquake Engineering Simulation User Command-Language Manual." Pacific Earthquake Engineering Research Center, University of California, Berkeley

McCormick, J., Barbero, L., and DesRoches, R. 2005. "Effect of mechanical training on the properties of superelastic shape memory alloys for seismic applications." Proc., Int. Society Optical Engineering (SPIE), 5764, 430–439.

Michaud, Véronique and Schrooten, Jan. (2002). Shape Memory Alloy Wires turn Composites into Smart Structures. Part II: Manufacturing anti Properties. *Smart Structures and Materials 2002: Industrial and Commercial Applications of Smart Structures Technologies Proceedings of SPIE*. 4698 (1), 406-415.

Miller D. A. and Lagoudas D. C. 2000. "Thermomechanical characterization of NiTiCu and NiTi SMA actuators influence of plastic strains" Smart Materials and Structures, 9, 640-652

Muller (1979). "A model for a body with shape-memory" Archive for Rational Mechanics and Analysis, 70(1), 61-77

Niezgodka, M. and J. Sprekels. (1986). "On the Dynamics of Structural Phase Transformation in Shape Memory Alloys", Preprint No. 114, Inst. fur Mathematik, Universitat Augsburg

Naito, H.; Sato, J.; Funami, K.; Matsuzaki, Y.; and Ikeda T. (2001). "Analytical Study on Training Effect of Pseudoelastic Transformation of Shape Memory Alloys in Cyclic Loading" Journal of Intelligent Material Systems and Structures, Vol. 12, pp 295-300

Paine J., and Rogers, C. (1994). The Response of SMA Hybrid Composite Materials to Low Velocity Impact, Journal of Intelligent Material Systems and Structures, 5, 530-535

Paine, Jeffrey S. N. and Rogers, Craig A.. (1995). Shape memory alloys for damage resistant composite structures. *Active Materials and Smart Structures*. 2427 (1), 358-371.

Pantelides, C. P.; Yan, Z.; and Reaveley, L. D. (2004). "Shape Modification of Rectangular Columns Confined with FRP Composites" Submitted to Utah Department of Transportation Research and Development Division

Pappada S.; Rametta, R.; Toia, L.; Coda, A.; Fumagalli, L.; and Maffezzoli, A. (2008) Embedding of Superelastic SMA Wires into Composite Structures Evaluation of Impact Properties, Journal of Materials Engineering and Performance, 18, 522-530

Pastore, Christopher M. and Ko, Frank K. (1999). "Braided Hybrid Composites for Bridge Repair." National Textile Center Annual Report: November 1999, F98-P01, USA,1999

Paultre, P. and Legeron, F., (2008). "Confinement Reinforcement Design for Reinforced Concrete Columns," Journal of Structural Engineering, 134, (5), 738-749

Perkins J. (1974) "Residual stresses and the origin of reversible (two-way) shape memory effects," Scripta Metallurgica, 8, 1469-1476

Rogers C. (1990) Active vibration and structural acoustic control of shape memory alloy hybrid composites Experimental results, J. Acoust. Soc. Am., 88 (6), 2803-2811

Rogers C.; Liang, C.; and Jia, J. (1991) Structural modification of simply-supported laminated plates using embedded shape memory alloy fibers, Computers and Structures, 38, 569-580

Said, A. M. and Nehdi, M. L. (2004). "Use of FRP for RC Frames in Seismic Zones: Part II. Performance of Steel-Free GFRP-Reinforced Beam-Column Joints" Applied Composite Materials 11, 227–245

Sittner P. and Stalmans R. (2000) "Developing hybrid polymer composites with embedded shape-memory alloy wires" Journal of the Minerals, Metals and Materials Society, 52(10), 15-20

Smith N., Antoun G., Ellis A., and Crone W. (2004). "Improved adhesion between nickel–titanium shape memory alloy and a polymer matrix via silane coupling agents". Composites: Part A, 35, 1307-1312

Somboonsong; Ko, Frank K.; and Harris, Harry G. (1998). "Ductile Hybrid Fiber Reinforced Plastic Reinforcing Bar for Concrete Structures: Design Methodology" ACI Materials Journal, 95 (6), 655-666

Sterzla, Tobias and Winzek, Bernhard. (2003). Bistable shape memory thin film actuators. *Smart Structures and Materials 2003: Active Materials: Behavior and Mechanics, Proceedings of SPIE*. 5053 (1), 101-109.

Strongwell Corporation. (2009). Pultrusion Process. Available: http://www.strongwell.com/pultrusion/. Last accessed 24 November 2009.

Tanaka, K. and S. Nagaki. "A Thermomechanical Description of Materials with Internal Variables in the Process of Phase Transformation", Ingenieur-Archiv, 51:287-299 (1982).

Toutanji H A (1999). “Stress-Strain Characteristics of Concrete Columns” ACI Materials Journal, 96 (3), 397-404

Todoroki, A.; Kumagai, K.; and Matsuaki, R. (2009) Self-deployable Space Structure using Partially Flexible CFRP with SMA Wires. Journal of Intelligent Material Systems and Structures, 00, 1-10

Tsoi, K.; Stalmans, R.; Schrooten, J.; Wevers, M.; and Mai, Y. (2003) Impact damage behaviour of shape memory alloy composites Materials Science and Engineering, A342, 207-215

Vamvatsikos D. and Cornell C.A. (2001.) "Incremental Dynamic Analysis" Earthquake Engng. Struct. Dyn.

Vokoun, David and Stalmans, Rudy. (1999). Recovery stresses generated by NiTi shape memory wires. *Smart Structures and Materials 1999: Mathematics and Control in Smart Structures*. 3667 (1), 825-835.

Wang X. (2002), Shape memory alloy volume fraction of pre-stretched shape memory alloy wire-reinforced composites for structural damage repair, Smart Materials and Structures, 11, 590-595

Weber, André; Schweinfurth, Jörg; and Jütte, Ben (2006). “Newly developed GFRP rebar in diaphragm walls of large tunnelling projects” Tunnelling and Underground Space Technology 21(3-4), 437.

Wei Z. G.; Sandstrom, R.; and Miyazaki, S. (1998). “Shape memory materials and hybrid composites for smart systems Part II Shape-memory hybrid composites Part II Shape-memory hybrid composites” Journal of Material Science 33, 3763-3783

Winzek B, Schmitz, S., Rumpf H., Sterzl T, Hassdorf R., Thienhaus S., Feydt J., Moske M., and Quandt E. (2004) Recent developments in shape memory thin film technology", Material Science and Engineering A, 378, 40-46

Xu Y., Toyama N., Yoshida H., and Kishi T. (2002). "A novel technique for fabricating SMACFRP adaptive composites using ultrathin TiNi wires". Smart Materials and Structures, 12, 196-202

Youssef, M. N.; Feng, M. Q.; and Mosallam, A. S. (2007) “Stress–Strain Model for Concrete Confined by FRP Composites,” Composites: Part B, 38, 614–628

Zak A., Cartmell M., Ostachowicz W., and Wiercigroch (2003). "One-dimensional SMA models for use with reinforced composite structures" Smart Materials and Structures, 12, 338-346

Zhang, Run-xin and Ni, Qing-Qing. (2007). Mechanical properties of composites filled with SMA particles and short fibers. *Composite Structures*. 79 (1), 90-96.